Facultat de Física

Departament de Física Atòmica Molecular i Nuclear
Universitat de València

Measurement of the top-quark pair production cross-section involving a tau & muon studies with TileCal in ATLAS

Eva Valladolid Gallego

Dirigida por:
Mª Victoria Castillo Giménez

DOCTORADO EN FÍSICA

July 2014

A mis padres

La Dra. Mᵃ Victoria Castillo Giménez, Catedrática del Departamento de Física Atómica Molecular y Nuclear de la Universidad de Valencia,

CERTIFICA:

Que la presente memoria, *Measurement of the top quark pair production cross-section involving a Tau & Muon Studies with TileCal in ATLAS*, ha sido realizada bajo mi dirección en el Departamento de Física Atómica Molecular y Nuclear de la Universidad de Valencia por Eva Valladolid Gallego y constituye su Tesis Doctoral para optar al grado de Doctora en Física.

Y para que así conste, en cumplemento de la legislación vigente, firmo el presente certificado.

Firmado: Mᵃ Victoria Castillo Giménez

Declaration

This dissertation is the results of my own work, except where explicit reference is made to the work of others, and has not been submitted to any other university.

Eva Valladolid Gallego

Abstract

The Large Hadron Collider (LHC) at the CERN laboratory started with its first proton-proton collisions in November 2009. The high energy physics program in the following has been dominated by the LHC and its experiments, looking for discoveries such as the Higgs boson, supersymmetric particles or new properties in known particles. This thesis is framed within the ATLAS experiment, one of the four large detectors located at the LHC and it is focused in Top Physics and Tile Calorimeter sub-detector studies.

The work presented contains an introductory part with the detector description and its expected physics performance. The first part, shows the result of studies developed within the ATLAS detector. Firstly it is described the process of data validation, showing some results that contributed to the commissioning of the hadronic ATLAS sub-detector *Tile Calorimeter* (TileCal). Also, studies performed with the muon identification algorithm, *TileMuId*, based on TileCal and used at Level-2 trigger for low-p_T muons detection during the previous period of data taking, are showed. The analysis was performed using cosmic rays data collected in autumn 2009. The second part of this thesis, represents a contribution to Top Physics studies, with an estimation of the top-quark pair ($t\bar{t}$) production cross section ($\sigma_{t\bar{t}}$), characterized by hadronically decaying τ and lepton in its final state ($t\bar{t} \rightarrow \tau\ell\nu_{\tau}\nu_{\ell}bb$, $\ell + \tau$ channel), using sample data collected in 2011 with an integrated luminosity of 4.73 fb^{-1}. The final measured cross section obtained is

$$\sigma_{t\bar{t}} = 184 \pm 10(\text{stat.}) \pm {}^{+20}_{-19}(\text{syst.}) \pm 3.3(\text{lumi.})\text{pb}$$

where 'stat.' represents the statistical, 'syst.' the systematic and 'lumi.' the luminosity uncertainties. The result is consistent with the theoretical prediction and other measurements performed so far. This study also includes the calculation of the Z scale factors used in the main analysis and an estimation of the mis-identification probability of τ leptons from hadronic jets using tag-and-probe method in the $\gamma + jets$ channel for background studies, validating the use of the BDT algorithm for tau identification with 2011 data.

Contents

List of Figures

List of Tables

Chapter 1

Introduction

The Large Hadron Collider (LHC) is a proton-proton collider located at CERN (*Conseil Européen pour la Reserche Nucléaire*) near Geneva, in Switzerland. It is currently the world's largest particle accelerator, where large quantities of protons in opposite directions at energies of 7 TeV are accelerated around a circular tunnel of 27 km circumference at close speed of light, which will reach a total energy collision of 14 TeV. The ring is located in Swiss and French lands and its experiment embedded in different points of the circular accelerator, represent a significant coordinate international effort to study the fundamental structure of the nature. It is expected that unknown physical phenomena will occur and could be observed. In this experiment there is a special research focus on dark matter, evidence of extra dimensions and the Higgs boson search, particle that give mass to elementary particles. CERN announced the discovery of the Higgs boson in July of 2012.

The Standard Model (SM) summarizes the understanding of the elementary particles, its constituents and how they interact. The model describes six types of quarks and leptons that interact by the gauge bosons. However physicist have developed theories that go beyond the SM in the search for new physics. For this search it is of particular interest the top-quark (t-quark), which is the heaviest elementary particle with 172.5 GeV, focusing specially in the t-quark pair production cross section ($\sigma_{t\bar{t}}$) characterized by lepton (μ or e) plus hadronically decaying τ ($t\bar{t} \rightarrow \tau\ell\nu_\tau\nu_\ell bb$, that is $\ell + \tau$ channel) for the search of new physics such as the charged Higgs boson.

ATLAS (A Toroidal LHC ApparatuS) is the largest experiment of the LHC. It is one of the two LHC general-purpose experiments, which attempts to make precise measurement of the SM to search for New Physics. The experiment gives the possibility to measure the t-quark pair production cross section ($\sigma_{t\bar{t}}$) with high

precision, due to its large centre of mass energy of $\sqrt{s} = 7$ TeV.

The present work is concerned with studies carried out in the ATLAS experiment, which is outlined as follows:

- Chapter 2 sums up a description of the underlying physics connected to the $t\bar{t}$ production, decay process and τ lepton. The QCD and electroweak theories are briefly explained.

- Chapter 3 summarizes the basic parts of the LHC accelerator and the ATLAS detector, with the description of their main parts and structure.

- Chapter 4 is devoted to the $TileCal$ detector and $TileMuID$ Level-2 Trigger algorithm studies, carried out during the commissioning phase of the ATLAS detector. Results from the contribution with studies in the Tile Calorimeter and Muon Level-2 Trigger systems in the ATLAS detector are presented. The chapter, divided in two parts, firstly describes the components of the electronic and calibration systems and shows results on data quality assessment performed in May 2009, intended for preparation of the TileCal before the start with data taking. Secondly, the chapter describes the Muon High Level-2 Trigger and TileMuID algorithm based on TileCal, and shows results from tests performed with cosmic rays taken in December 2009.

- Chapter 5 contains Top Physic studies with a scenario where the top pair production cross section with a lepton and a hadronically decaying τ lepton in the final state, is measured. To develop this study, sample data collected in 2011, with 4.73 fb^{-1} of $proton$-$proton$ collisions accumulated by the ATLAS experiment, were used. The work also includes results of the mis-identification probability of τ leptons from hadronic jets, using the tag-and-probe method in the $\gamma+$ jet channel, and the calculation of the Z scale factor used for the cross- section estimation.

Chapter 2

Physics Motivations

In this chapter the general physics motivations of the ATLAS experiment are introduced, followed by the description of the physics of the top quark pair production of interest relative to the results of this work, as well as physical properties of the τ lepton.

2.1 The Standard Model

The Standard Model of the particles (SM) is a unified quantum field theory, consistent with quantum mechanics and special relativity, which allows the understanding of the elementary particles structure and describes the fundamental interactions between them. It is the theory that better describes the experimental observations at the moment, and has been proved valid at very high energies in many accelerator experiments. The elementary particles can be classified as: leptons, quarks and bosons. Leptons and quarks, named fermions, are spin $1/2$ particles and are organized in three families. The bosons are integer spin particles. Figure 2.1 shows the list of the SM elementary particles, including properties as the mass, charge and spin, as well as the fundamental interactions between them.

There are four fundamental forces of nature through which the particles interact: the electromagnetic, the weak, the strong and the gravity. Each fundamental force has its own corresponding boson. Currently the SM only suits the first three forces but many extensions and new theories try to unify the four:

- The electromagnetic interaction takes place between particles which have electric charge. Its associated boson is the photon (γ), which is a neutral massless particle.

- The weak interaction is responsible of the radioactive decay of the nucleus trough the exchange of Z^0 and $W^{\pm}$ bosons. These particles have very large masses limiting the range of the interaction.

- The strong interaction is responsible for retaining the protons and neutrons together in the atomic nuclei. The associated bosons of this force are the gluons which are massless particles that carry color charge.

- The gravity acts between all types of particles. Its associated boson is the undiscovered graviton. This interaction can be considered insignificant between elementary particles.

In the frame of quantum mechanics formalism, the SM is written as a gauge field theory based on symmetry group. It unifies the electroweak (EW) interaction (which unifies electromagnetic and weak forces) and the quantum chromodynamics (QCD). The bosons are a manifestation of the symmetry group of the theory, which for the SM is $SU(3)_C \otimes SU(2)_L \otimes U(1)_Y$ where C denotes 'Color', L denotes 'Isospin' and Y denotes 'Hyper-Charge'. The $SU(2)_L \otimes U(1)_Y$ symmetry group, describes the so-called Electroweak Interaction (Quantum Electrodynamics o QED), which is spontaneously broken through the existence of a Higgs field with non-zero expectation value. This leads to the emergence of massive vector bosons, the $W^{\pm}$ ($M_W \sim 80$ GeV) and the Z ($M_Z \sim 91$ GeV), which mediate the weak interaction, while the photon (γ) of electromagnetism remains massless. The quarks are triplets of the SU(3) gauge group and so they carry an additional charge, referred to as 'color', which is responsible for their participation in the strong interaction (Quantum Chromodynamics o QCD). Eight vector gluons mediate this interaction; they carry color charges themselves, and are thus self-interacting. This implies that the QCD coupling is small for large momentum transfers but large for soft processes, and leads to the confinement of quarks inside color-neutral hadrons (like protons and neutrons). Attempting to free a quark produces a jet of hadrons through quark-antiquark pair production and gluon bremsstrahlung.

However, the SM fails to be a complete theory of fundamental interactions because it does not include gravity, the fourth fundamental interaction known. It carries also more theoretical problems and some experimental results not yet understood as:

- Unification of the forces: Nowadays it is sought the unification of the electroweak theory with the strong interactions. The Great Unified Theory (GUT) try to join both in only one interaction characterized by a simple coupling constant.

- Dark matter: there are experimental proves that dark matter exist, but its nature is not known.

- Matter-antimatter asymmetry: Currently it is known that there is a lack of balance between matter and antimatter not yet understood, but SM assumes that the particles and antiparticles have the same masses.

- Neutrino masses: The SM takes on zero the mass of the neutrinos, but experimental results show that they have small but finite masses.

- Hierarchy problem: it is related with the unnaturally Higgs mass. At Planck scale the theoretical calculation of the Higgs mass gives different masses that crashes with the current LHC results.

On July 4, 2012, CERN announced the observation of a new particle 'consistent with the Higgs boson'. On March 14, 2013, with two times more data, it was confirmed that the new particle is increasingly seen as the Higgs boson. Nevertheless, still remains the question of whether this particle is the Higgs SM or perhaps the lightest of several bosons predicted in some theories that go beyond the Standard Model. Given the current experimental results, the SM is not considered as the final theory. Current experiments have significantly increase the energy of the collisions, expecting to show enlightening results in the near future. The previous questions and experimental observations have addressed to the develop of many theories to cover the physic Beyond the Standard Model (BSM). One of them is the Supersymmetry, briefly explained in the next section.

2.1.1 Supersymmetry

The SM has worked really well to predict what experiments have shown so far about the basic constituent of matter, but it looks that it is incomplete. An extension of the SM is the Supersymmetry (SUSY) theory that aims to fill some of the remaining questions. It predicts a partner particle for each particle in the SM, which would solve a major problem with the theory. If the theory is correct, supersymmetric particles should appear in collisions at the LHC, but no hint of supersymmetry has been observed up to now.

SUSY predicts new particles that would interact through the same forces as SM particles, but they would have different masses. If supersymmetric particles were included in the SM, the interactions of its three forces (electromagnetism and the strong and weak nuclear forces) could have the same strength at very high energies. Supersymmetry would also link the two different classes of particles known as fermions and bosons. In the SM fermions all have spin 1/2, while the bosons have

Figure 2.1: Elementary particles of the SM.

0, 1 or 2 units of spin. SUSY predicts that each of the particles in the SM has a partner with a spin that differs by half of a unit. Then, bosons are accompanied by fermions and the other way round. In many theories it is predicted the lightest supersymmetric particle to be electrically neutral and stable. It interacts weakly with the particles of the SM. These are the characteristics required for dark matter. It is believed that comprises most of the matter in the universe and to hold galaxies together.

The SUSY is covered by the ATLAS experiment with the search of new vector bosons usually labeled as W' and Z' up to a mass scale of 5 TeV, excited quarks up to 6 TeV of mass, lepto-quarks up to 1.5 TeV, Technicolor resonances up to a mass limit of 1 TeV, signature of extra-dimensions and new particles predicted by the Little-Higgs models.

2.1.2   The Electroweak measurements

The model of Glashow-Weinberg-Salam (GWS) of electromagnetic and weak inter-actions is a gauge theory based on the broken symmetry group $SU(2)_L \otimes U(1)_Y$ (L denotes weak isospin space, and Y denotes hyper-charge). The Electroweak Theory (EW) represents the unification of the weak theory and the Quantum Electro

Dynamics (QED). The interactions of these theories have been established in two stages, the neutral currents in neutralino scattering and the discovery of the W and Z gauge boson in proton-antiproton collisions.

The ATLAS experiment studies the production of W and Z events, where precision measurements are performed due to the high center of mass energy reached in the experiment, which implies high cross-sections. For Z production of reconstructed final states, ATLAS allows precise measurements of the transverse momentum and the rapidity function. The measurement of the Z boson, allows the development of studies that can be useful to measure detector energy, resolution and momentum, being possible to check the width, mass and leptonic decay of the boson, as well as the lepton identification.

In ATLAS, electroweak measurements including the W and Z boson, allow to check the SM. The understanding of the hadronic behavior and environment is crucial to achieve physics goals. There are compulsory inputs of measures of the Z and W bosons from which via their final states, a number of fundamental electroweak parameters can be obtained. For example, lepton definition by comparing muon and electron cross-sections, or M_W via the W boson decay.

The di-boson production using photon and lepton final states, is also important. It gives information of the behavior of the electroweak interactions setting limits into high energy. This is useful in the triple gauge boson couplings, where precise measurements of the couplings will be interesting to unveil possible new physics in the LHC.

2.1.3   QCD and Strong Interaction

The gauge theory of the strong interactions in the quark model is named QCD, and is based on the symmetry group $SU(3)_C$ (C denotes Color states of the quarks). Only quarks carry colour and charge, and can be the unique matter particles that interact with the strong force in the SM. There are eight massless colored gluons, g_α that are the gauge mediators of the strong interaction.

When a quark is isolated from its original hadron, due to a collision with another particle, the isolated quark tends to group with other quarks to form a colorless particle, producing new hadrons and mesons. This phenomenon is called the hadronisation that produces jets.

2.1.4   Searches of the SM Higgs

One of the main goals of LHC has been the discover of the Higgs boson that allows the SM theory be complete. In the last two years the search has been performed in a wide variety of decay channels, having as important problem that the mass of the boson itself was not known, being the branching ratios of the decay channel

dependent of the Higgs' mass. One of the more visible signatures is the decay of the Higgs boson to two photons and two Z or W$^{\pm}$ pair, channels that has been searched in a mass window of 115-130 GeV/c^2.

In July 2012 the discover of a new particle was announced, based on data collected in 2011 and 2012, with 2012 data still under analysis. Results showed clear signs of the existence of a new particle at a significant level of five σ in the mass region around 126 GeV, which made suspect that this particle could be the Higgs boson. In March 2013 was confirmed that this new particle looked closer to be the Higgs boson, after having analyzed two and a half times more data than it were available for the discovery announcement in July 2012.

At this time still remains the question of whether it is the Higgs boson of the SM, the particle linked to the mechanism that gives mass to elementary particles, or maybe the lightest of several bosons predicted in some theories that go beyond the SM. Results show that the new particle has the spin-parity of the searched Higgs boson and new precise measurements must be performed to compare the results with the predictions.

2.2   The Top Quark physics

The top quark discovery took place in 1995 by CDF experiments at Tevatron in Fermilab. It is the heaviest elementary particle with 172.5 GeV and represents the third generation of the quark doublet. Due to its heavy mass, its decay exhibits a large phase space, for what it represents an important probe for the search of the new physics in the SM framework. The production of the top quark is one of the dominant process after QCD jets, W and Z bosons. Nowadays some of the properties of the top quark have already been studied in the LHC: cross-section, mass, spin, charge, charge asymmetry, rare decays or resonances, among other properties.

2.2.1   Process of production, decay and measurement of the Top Quark

In Hadron Colliders, there are two mechanisms of production of top quarks: $t\bar{t}$ pairs produced through Quantum Chromo-Dynamics interactions and single top that are produced through the weak interaction. The production of a pair in a proton-proton collision, occurs through gluon-gluon and quark-antiquark fusion, where the cross section depends on the center of mass energy (figure 2.2). At Tevatron the production was restricted to the quark-quark fusion, but in the LHC, with the largest energies ever produced, the gluon scattering processes represent
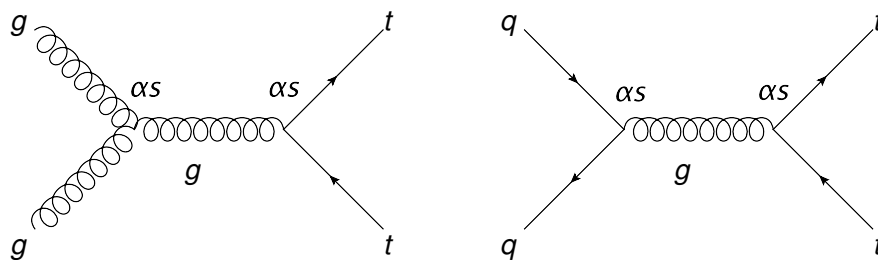
Figure 2.2: Feynmann diagrams for the top production processes, for gluon-gluon fusion (left) and quark-quark fusion (right).

the majority of the cases. The LHC is named to be a top quark factory, producing millions of $t\bar{t}$ pairs only in a sample of 10 fb^{-1}. Since the operation of the accelerator started, enormous quantities have been collected.

In the ATLAS experiment, one of the studies concerned to top-quark pair production is the measurements of its cross-section. These measurements are important for the study of intrinsic properties of the quark and its interactions and to the search for new production mechanisms non-SM related. The production of the $t\bar{t}$ cross-section can be measured by its decay into a single muon or electron with associated jets, or into two muons or electrons with jets. Figure 2.3 shows the latest $t\bar{t}$ cross-sections measured at LHC. The obtained value at 7 TeV is 177^{+11}_{-9} pb and 241 ± 32 pb at 8 TeV, in the $\ell + jets$ channel. The experimental results in the different top decay channels at 7 TeV and at 8 TeV are compared to an estimated Next-to-Next-to-Leading-Order (NNLO) QCD calculation.

The production of single top quarks in LHC represents the third of the total $t\bar{t}$ production. Only with a few fb^{-1} is possible to measure with high precision the single top cross-sections. It is required the use of sophisticated analysis techniques for the search of top pairs candidates events and the reduction of the different backgrounds.

The decay process is described by the electroweak theory once that the top quark is generated. The $t\bar{t}$ pair decay can be categorized by the decay product of two W bosons. The top quark decays predominantly into a W and a b-quark with a branching ratio near 100%. The W boson decays either into a quark and anti-quark pair with probability close to 2/3 or into a charged lepton-neutrino pair with probability of 1/3. Top pair final states are classified according to the W boson decays, where the all-jet mode accounts for about 44% of the decays, lepton plus jets for close to 45% and the di-lepton mode, for about 10% of the decays. Final states containing electrons or muons are of particular interest for early measurements as they provide clear triggers signals and rich event signatures. The signature of these events is that they usually contain jets (two are originated
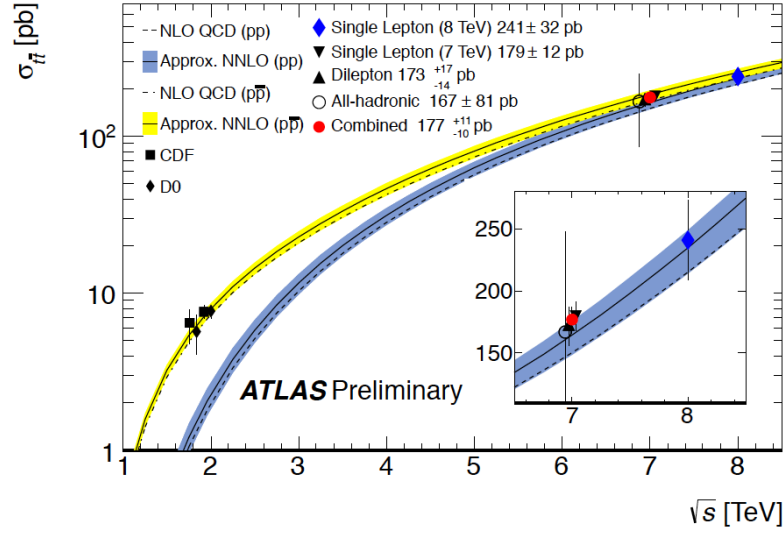
Figure 2.3: Top pair production cross section as a function of the LHC center of mass energy ($\sqrt{s}$).

from b-quarks decay). They also exhibit high p_T, isolated charged leptons and missing transverse energy (Et_{miss}) from the escaping neutrino. The branching fractions of the top quark pair decay by categories, are represented in figure 2.4 (left).

Associated to the production and the decay of the top quark there are processes, such as multiple parton interaction, pile up, initial state radiation (ISR) and final state radiation (FSR), that can be described by QCD. These are underlying events that do not change the overall cross-section, but affect the acceptance required for the cross-section measurement. Since the acceptance is estimated by monte carlo (MC), these events must be modeled and considered for the final measurement, fitting the experimental data. It is necessary to consider the pile-up events produced by additional collisions, so the measurements of the top quark will be restricted to regions in which the systematic uncertainties are accepted.

The work presented in this study is related to $t\bar{t}$ events, where each W boson decays into a lepton (e or μ) and a τ pair.

2.3   The τ lepton

The τ particle is a lepton that plays an important role in the physics program at the LHC. It is equivalent to the electron and the muon but with higher mass.
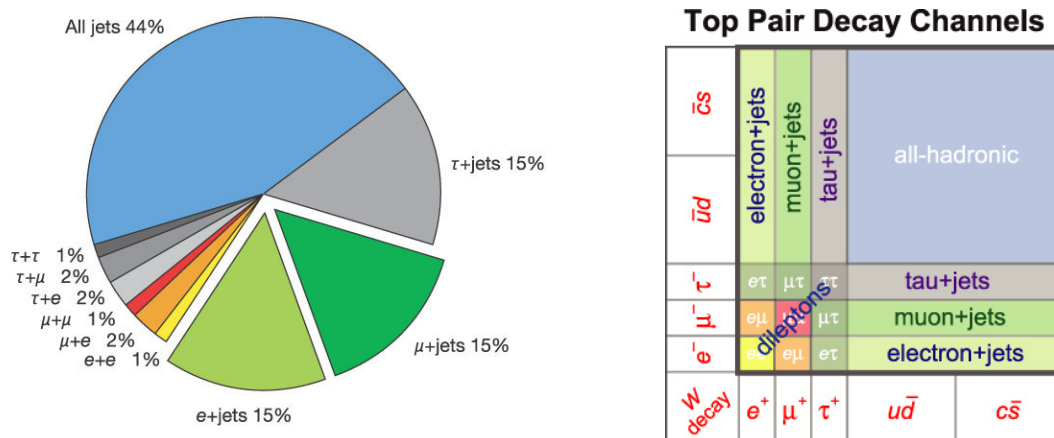
Figure 2.4: Branching ratios of the top quark pair decay by categories (left) and top quark pair decay channels (right).
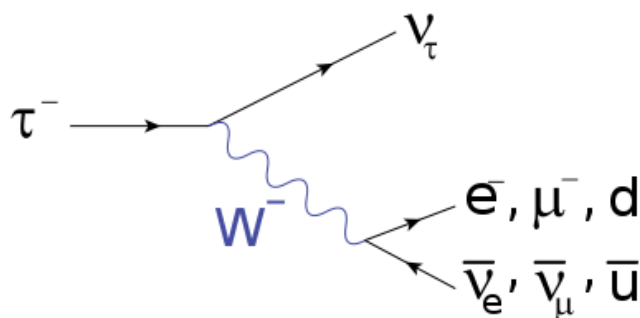
Figure 2.5: Feynman diagram of the τ decay through W boson production.

The τ, with mass m$_\tau$ =1777 MeV, is the only lepton which is able to decay into hadrons, and not only into leptons. The decay percentage that goes to a lepton is 35% ($\tau \to e\nu$ or $\tau \to \mu\nu$), and 65% decay into hadrons.

The τ jets have an odd number of charged tracks, topologically compacted in narrower jets compared to the QCD originated jet. This is an interesting feature that makes easy its study, sometimes used as a multivariate discriminate that allows better identification than the use of simple cuts. The τ lepton is a useful probe used for the search of new physics like the Higgs boson or even SUSY searches, and in electroweak measurements. Figure 2.5, shows the Feynman diagram of the common decays of the tau by emission of a W boson. Figure 2.6, shows the basic signatures of the hadronically decaying τ lepton.
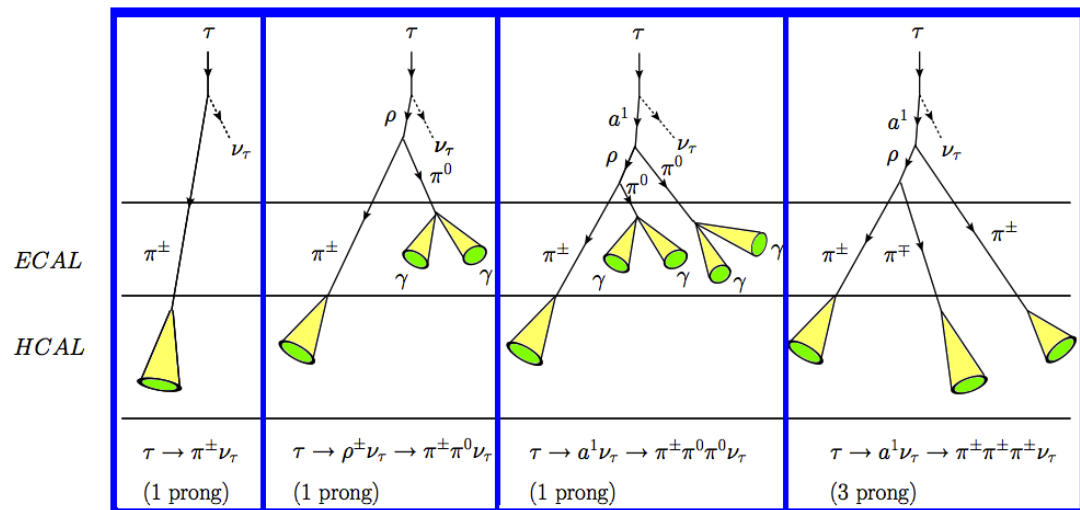
Figure 2.6: Basic signatures of the hadronically decaying τ lepton.

Chapter 3

The LHC and the ATLAS Experiment

3.1 The Large Hadron Collider

The Large Hadron Collider (LHC) [1], is currently the world's largest particle accelerator with the highest energy ever produced. It was built by the European Organization for Nuclear Research (CERN), from 1998 to 2008, with over 10,000 scientists and engineers from over 100 countries with the participation of universities and laboratories around the world, involved in high energy physic research.

The accelerator started its operation with proton-proton collisions in November 2009. During 2011 was operated with $\sqrt{s} = 7$ TeV. Due to its large center-of-mass energy, the $t\bar{t}$ production rate is 25 times larger than the previous highest-energy accelerator, the TEVATRON, for what LHC is considered a t-quark factory that provides the opportunity to evaluate $t\bar{t}$ cross section with precision.

The present chapter describes the LHC accelerator and the ATLAS detector, the largest of the LHC experiments, in which this work is performed.

3.2 The LHC accelerator

The LHC is installed in the 27 km long tunnel of the former Large Electron Positron collider (LEP). It is about 50-175 meters below the ground and located between Switzerland and France, next to the city of Geneva. Figure 3.1, shows an aerial view with the location of the accelerator. The accelerator design will allow to collide protons into protons at a center-of-mass energy of about 14 TeV, with a design luminosity of 10^{34} cm^{-2} s^{-1}, delivered by the Super Proton Synchrotron (SPS). The proton bunches circulate in the accelerator ring in opposite directions nearly at the speed of light. There are four collision points where detectors are

located in different locations of the accelerator. The experiments are ATLAS (Point 1) and CMS (Point 5), two of the LHC detectors that study fundamental physics; ALICE (Point 2), the experiment that works with quark plasma and gluons, and LHCb (Point 8), which aims to explain the asymmetry between matter and antimatter. Figure 3.2, shows the points where the different experiments inside the ring accelerator are located.

Figure 3.1: Aerial view of the LHC area and its main experiments located in the interaction points.

The performance requirements of the LHC imply important challenges in the design and construction of the accelerator. To bend the protons around the ring, 1.232 LHC dipoles (figure 3.3) with a magnetic field of 8.36 Tesla are used, producing a high field using niobium-titanium super-conducting magnets and super-fluid helium. The magnets cover around 20 km of the ring. To boost the luminosity the beams are focused at the collision points, using 392 quadrupole magnets in the straight sections of the ring. A cooling system maintains the operation temperature at 1.9 K.

The accelerator is made up of injectors, intermediate accelerator and the main part, which is named LHC. Before the main ring, there are a series of accelerators by which the beam energy is increased as where as the beam goes through the different rings. The starting point is a Linear Accelerator (LINAC) where protons
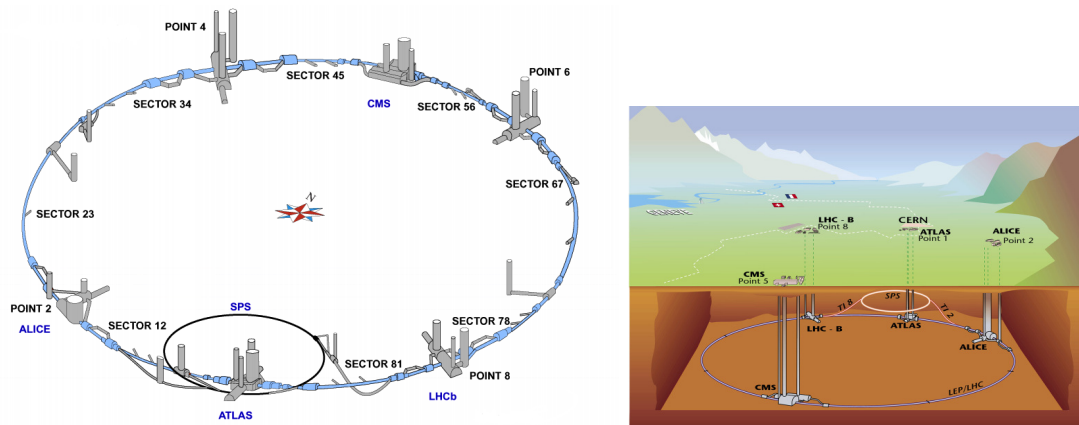
Figure 3.2: Sketches of the LHC experiments located in the interaction points of the accelerator, with sector divisions (left) and land location (right).
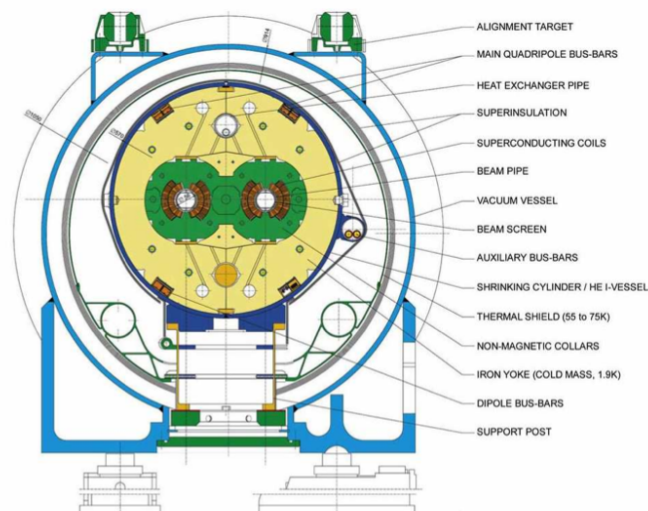
Figure 3.3: Cross section of the LHC beam pipe with dipole magnet.

are generated using hydrogen nuclei by ionizing the atoms and accelerated up to around 50 MeV. To increase the energy, the protons are sent to the Proton Synchrotron Booster (PSB, with 157 meters long), where they are accelerated up to 1.4 GeV and sent to the Proton Synchrotron (PS, with 628 meters), where protons are accelerated up to 25 GeV. The Super Proton Synchrotron (SPS, 7 kilometers) receives the protons and increases their energy up to 450 GeV. Finally,

the protons are injected into the main LHC tunnel, achieving 7 TeV beam energy, where they circulate in two separated proton beams in opposite directions, reaching speeds close to the speed of light (relativistic) and energies around 7 TeV. Then, both beams collide at each experiment site. For the ALICE experiment, lead (Pb) ions come from a vaporized lead source and sent through the linear accelerator LINAC3, to the Low Energy Ion Ring (LEIR). Then follow the same route as the protons, but only colliding at the ALICE experiment. In figure 3.4 is showed a scheme of the CERN accelerator complex.
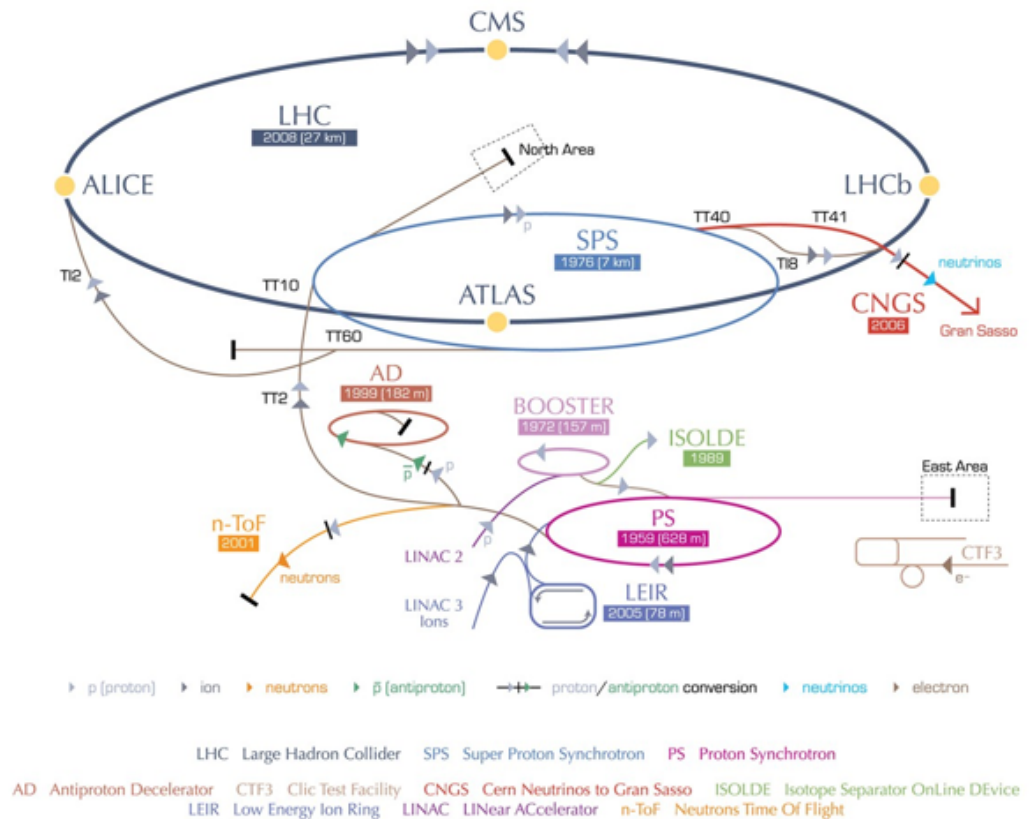
Figure 3.4: LHC Chain accelerators.

Protons are bundled into 2808 bunches for data-taking, where each bunch consists of 1.15×10^{11} protons. Those are controlled by 40 MHz Radio Frequency (RF) clock, which results in intervals of collision of 25 ns. The RF clock is also distributed to each detector to achieve synchronized data-taking. Table 3.1 summarizes the main parameters of the LHC at the nominal values and the ones achieved during 2011, the period where data were taken for the physic analysis

presented in this work. The number of protons per bunch already reached its design value.

Table 3.1: LHC main parameters with the nominal parameters value and the achieved values during 2011.

	unit	Designed	Parameter in 2011
Beam related parameter			
Proton beam energy	[TeV]	7	3.5
Relativistic γ	$-$	7461	3730
Magnetic field strength of the dipoles	[T]	8.3	4.2
Number of protons per bunch	$-$	1.15×10^{11}	1.15×10^{11}
Number of bunches	$-$	2808	1380
Circulated beam current	[kA]	11.85	5.93
Luminosity related parameter			
RMS bunch length (σ_z)	[cm]	7.55	6
RMS beam size (σ_x, σ_y)	[μm]	16.7	22
Instantaneous peak luminosity	[1/cm^{2}s]	1.0×10^{34}	3.5×10^{33}
Interval of the beam collision	[ns]	25	50

3.3   The ATLAS Detector

ATLAS, *A Toroidal LHC Apparatus*, is the largest experiment of the LHC. It is located at the interaction point 1 of the accelerator. More than 30 nations collaborated in its construction with the participation of about 4,000 scientist. The experiment was designed to exploit the full potential of physics in the LHC, exploring the fundamental properties of nature and the basic forces that shape the Universe. This implies a wide range of design requirements with a high field of specifications. The components must work reliably in a high radiation environment and provide precise measurements of various physical quantities, which are crucial to discover and study new physics processes and signatures. The collisions of protons in the centre of the detector, where the energy density in the high energy collisions is similar to the particle collision energy in the early Universe, less than a billionth of a second after the Big Bang, will reveal these fundamental particle processes.

3.3.1   Overview of the ATLAS detector

The ATLAS detector consists of different sub-detectors, from the inner to the outer part: inner tracker, solenoid magnet, liquid argon electromagnetic calorimeter, hadron calorimeter, toroid magnet, and the muon spectrometer (figure 3.5). The dimensions of the whole detector is 25 meters of diameter and 44 meters long, with a weight of 7000 tons. The ATLAS detector is a very complex instrument, described in detail in [2].
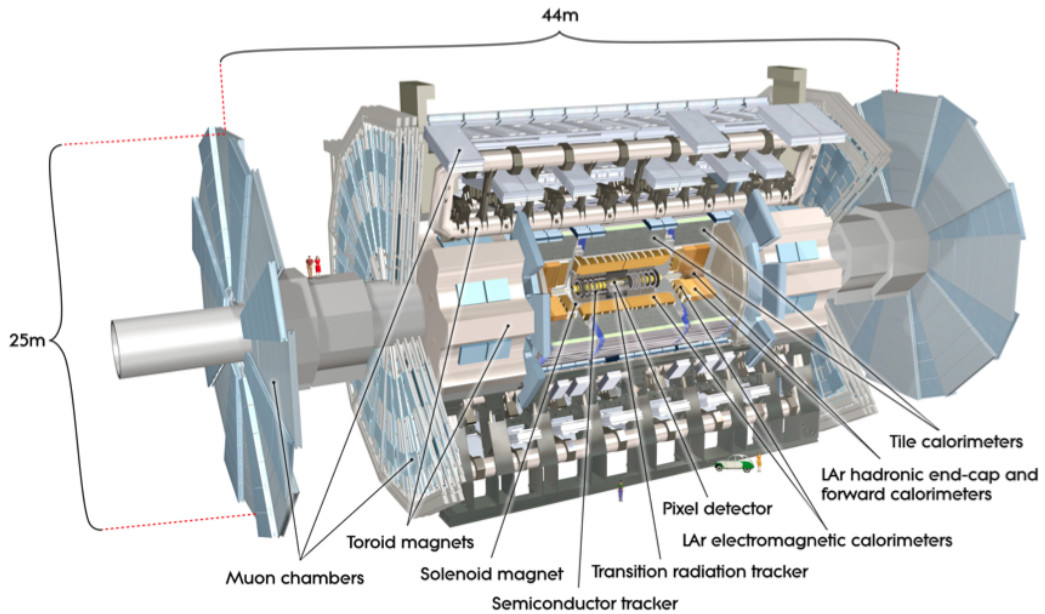
Figure 3.5: Overview of the ATLAS detector layout.

The detector requirements to achieve the demands of the physics program, where stable particles such as protons, neutrons, leptons and photons must be identified with precise measurements, are summarized as follows:

- High-precision of muon momentum measurements, with high accuracy at the highest luminosity, using the external muons spectrometer;

- High charged particle momentum resolution and track reconstruction efficiency;

- Good electromagnetic calorimetry for electron and photon identification and measurement;

- Full-coverage hadronic calorimetry for accurate jet and missing transverse energy measurements;

- Large acceptance in the polar and azimuthal angles;

- Fast and radiation hard electronics and sensor elements.

The ATLAS detector must have high accuracy and large acceptance in all components, to record the basic signatures with particle identification and measurements as the missing transverse energy, vertex tagging or hadronic jets. The identification of some of these signatures must be optimized for a high luminosity environment. The detector system is basically divided in the following components:

- Tracking detectors - for measurement of charged particles;

- Calorimetry - for energy measurements of electronic and hadronic particles;

- Muon chambers - for muon reconstruction and p_T measurements;

- Magnet system - for bending the trajectory of charged particles.

Particle identification is based on the particle charge and the penetration power in the material, that depends on how particles lose energy in the material. Basically, γ's and e's particles are captured in the electromagnetic calorimeter, while p's and n's are captured in the hadronic calorimeter. Muons are not stopped and go across the tail detector being registered also in the muon spectrometer. The presence of ν's, can not be directly detected, but it is possible to check its contribution by momentum imbalance in the transverse plane (figure 3.6).

Each sub-detector focusing in its performance and particle identification, is divided by:

- **Inner Tracker**: Reconstructs charged tracks and measures its transverse momentum (p_T). Additionally, reconstructs secondary vertices based on the resulting tracking.

- **Calorimeter**: Reconstructs jets. Electromagnetic calorimeter detects e/γ, while hadron calorimeter detects hadron jets.

- **Muon spectrometer**: Reconstructs muons and measures the p_T.

A brief summary of the detector performance and its coverage is shown in Table 3.2.
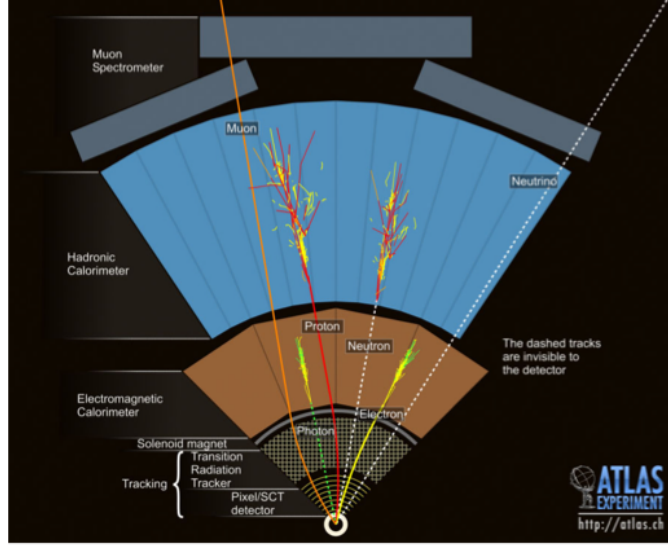
Figure 3.6: Basic principle of the particle identification scheme in the ATLAS detector.

Table 3.2: Summary of the detector performance and η coverage.

Detector	Designed performance	η coverage
Inner tracker	$\sigma_{p_T}/p_T = 0.05\% p_T \oplus 1\%$	$|\eta| < 2.5$
	vertex resolution 10 μm (xy), 50 μm (z)	
EM calorimeter	$\sigma_E/E = 10\%/\sqrt{E} \oplus 0.7\%$	$|\eta| < 3.2$
Hadron calorimeter	$\sigma_E/E = 50\%/\sqrt{E} \oplus 3\%$	$|\eta| < 3.2$
	$\sigma_E/E = 100\%/\sqrt{E} \oplus 10\%$	$3.2 < |\eta| < 4.9$
Muon spectrometer	$\sigma_{p_T}/p_T = 3\%$ $(p_T < 100$ GeV$)$	$|\eta| < 2.7$
	$\sigma_{p_T}/p_T < 10\%$ $(p_T < 1$ TeV$)$	

3.3.2   Nomenclature of the coordinate system

The coordinate system used in the ATLAS detector is described in this section. The origin of the three axes of the coordinate system is defined in its interaction point, as it is showed in figure 3.7. The positive x-axis is pointing towards the center of the LHC ring, and the positive y-axis points to the sky, being the x-y plane transverse to the beam direction. This defines the z-axis positive according to the right-handed system.

More of the variables used are defined as follows:

- ϕ: Azimuthal angle ϕ measured from positive x-axis.

- θ: Polar angle θ measured from positive z-axis. However, pseudo-rapidity variable is usually used instead of θ.

- η: Pseudo-rapidity is more useful to discuss about particle decay rate than θ, since it is the Lorentz invariant variable with respect to the Lorentz boosts in z direction. The phase space is proportional to η, and is defined as

$$\eta = -\ln\left[\tan\left(\frac{\theta}{2}\right)\right] \tag{3.1}$$

- p_T and E_T: In the LHC, since the momentum and energy conservation (equation 3.2) is kept in the plane xy, transverse momentum ($p_T = p\sin\theta$) and transverse energy ($E_T = E\sin\theta$) measurements, are used for identification.

$$\sum_{\text{particle}} p_T = 0 \tag{3.2}$$

- $\Delta \mathbf{R}$: The distance between two objects (equation 3.3), as it can be the distance between a jet and a muon, is defined in the η-ϕ plane. It is used as an index of the closeness between both of them ($0 < \Delta\text{R} < 4\pi$).

$$\Delta R = \sqrt{\Delta\phi^2 + \Delta\eta^2} \tag{3.3}$$

3.3.3 The Inner Detector

The Inner Detector (ID) [3] is the innermost sub-detector of ATLAS. It consists of different layers of high precision and granularity in the inner part and straw tubes in the outer part. The ID can reconstruct tracks of charged particles in a solenoidal magnetic field of 2T with a coverage up to $\eta = 2.5$. It makes use of magnetic deflection to measure the transverse momentum of the charged particles. The track traverses subsequently the beryllium beam-pipe, where there are three cylindrical silicon layers with individual pixel of 50×400 μm^2, four cylindrical double layers of a barrel silicon-microstrip sensors (SCT) of pitch 80 μm and 36 axial straws of 4 mm diameter contained in the barrel transition-radiation tracker (TRT) modules within their support structure.

So, there are two essential roles for the inner tracker. Firstly, to detect charged particles and measure the p_T, and secondly, to reconstruct the vertices with a resolution of 10 μm (xy) $\times$50 μm (z). 25 interactions per bunch are produced crossing at the designed luminosity, which result in more than 1000 charged tracks
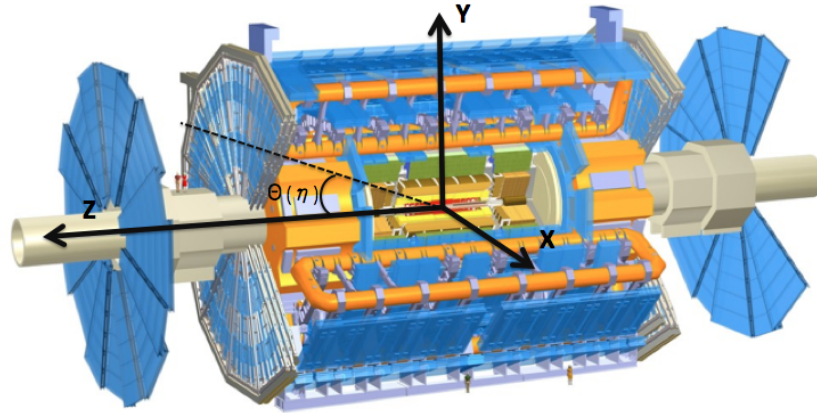
Figure 3.7: ATLAS schematic view with its coordinate system, which has the origin in the beam interaction point.

simultaneously. The selection of a set of tracks coming from the same vertex, is essential for the event reconstruction and other subjets as for instance, b-tag performance. Figure 3.8 shows the an schematics of the cross-section view of the ID. The main requirements for the ID are:

- Tracking efficiency of at least 95% over the full coverage for isolated tracks with $p_T > 5$ GeV.

- Momentum measurement in a large momentum range.

- To distinguish between electrons and photons that produce similar clusters in the Electromagnetic Calorimeter, and charge identification of particles with large transverse momentum.

- Momentum measurement of low energy muons which have large multiple scattering in the hadronic calorimeter, which is of interest for the present study.

- Tagging jets originating from high energy b-quarks and electron/jet separation in addition to the one already provided by the calorimeter.

- Identification of the primary vertex in the presence of many vertices from overlying minimum bias events.

- Identification of individual particles that perform a jet when the calorimeter cannot resolve individual particles.
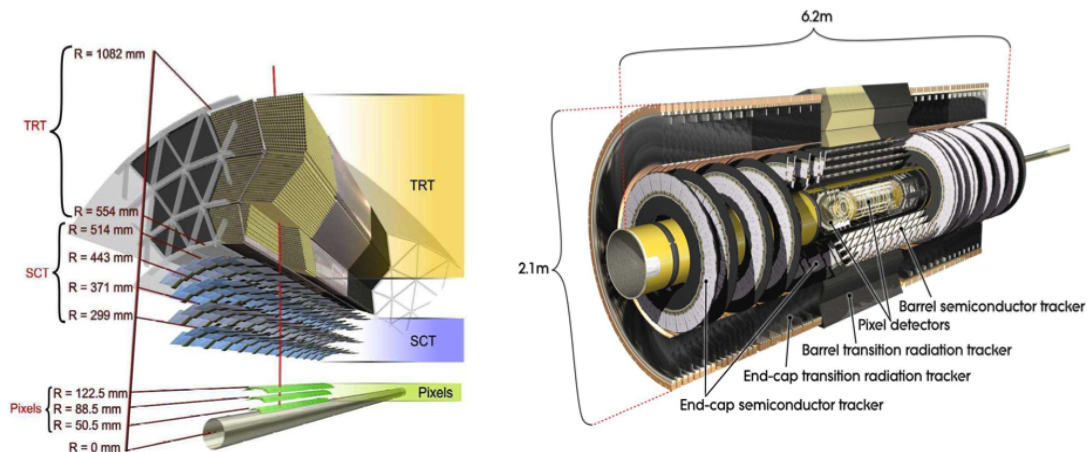
Figure 3.8: Cross-section view of the inner detector in the barrel (left) and schematic view (right) with the structural elements traversed by a charged track of 10 GeV p_T in the barrel inner detector. This sub-detector consists of two types of silicon devices, pixel and SCT, and one TRT.

The main parts of the ID, which has two silicon devices and one transition radiation tracker are summarized as follows. From inner to outer, Pixel Detector (Pixel), SemiConductor Tracker (SCT), and Transition Radiation Tracker (TRT), in a 2T magnetic field produced by a superconducting solenoid magnet.

Pixel Detector (Pixel)

The Pixel Detector is placed in the innermost part of ATLAS, and consists of three cylindrical layers placed from $r = 50.5$ mm to 122.5 mm in the barrel, being the radius of the beam pipe $r = 25$ mm. It is designed to provide a very high-granularity, and high-precision set of measurements as close as possible to the interaction point. Three disks formed by rectangular pixel modules are placed in the endcap, normally to the beam axis from $z = 495$ mm to $z = 650$ mm, which covers up to $|\eta| < 2.5$. The granularity consists of 2-dimensional semi-conducting silicon sensors with a pixel size of $50 \times 400 \ \mu\text{m}^2$. The channel sizes are optimized to achieve the required p_T resolution and vertex resolution for some benchmark physic processes, with a detection efficiency of the pixel detector higher than 99%, at a bias voltage of 150 V. The most important requirements for the pixel detectors is the determination of secondary vertexes for the identification of B decays, for

$b - tagging$ in top physics. It is important for pattern recognition since it has very low occupancy in spite of its close placement to the primary vertex, where it is placed the as close as possible to the beam pipe.

Semi conductor Tracker (SCT)

The SCT system, the second part of the ID, starting from $r = 299$ mm in the barrel and $z = 854$ mm in the endcap, is designed to provide eight precision measurements per track in the intermediate radial range, contributing to the precise measurement of momentum, impact parameter and vertex position. The SCT can also provide good pattern recognition due to the high granularity. The sub-detector consists of strip type semiconductor-sensors of 6.4 cm long with 4 double sided layers in the barrel, a mean strip pitch of 80 μm in ϕ at the barrel and 9 disk-shape layers in the endcap, with two sided readout. Charged particle can cross more than 8 layers in total.

The intrinsic position resolution in the barrel is 17 μm in $R\phi$ and 580 μm in the z direction, while it is 17 μm in ϕ, and 580 μm in the R direction in the case of the endcap. The SCT is operated with a biased voltage of 150 V, with efficiency of 99% and a total number of readout channels of 6.4 Million.

Transition Radiation Tracker (TRT)

The TRT is the outermost part of the inner tracker, based on straw detectors. The TRT consists of a sense wire and a cathode for electron identification, operated in a mixture of Xenon gas to detect transition-radiation photons created in a radiator between the straws. The filling with the gas allows the absorption of transition radiation which also enables a faster drift-time for electrons, providing high spatial resolution. In the center of the straw there is a 30 μm gold covered tungsten wire. This hard radiation technique allows a large number of measurements to be made from every track. The TRT provides additional discrimination between electrons and hadrons. The detection efficiency is about 80 %, and the total number of readout channels is 174 k.

Solenoid magnet

The ATLAS detector has a superconducting solenoid magnet between the ID and the calorimeter of 5.3 m long, which allows to obtain the p_T measurement of the charged tracks. The magnet produces 2T of uniform magnetic field along the Z axis, and it is operated with a current of 7.73 kA and at a temperature of 4.5 K. The magnet system is described in more detail in section 3.3.6.

3.3.4 Calorimetry

The calorimetry is divided in two main parts: the liquid Argon system and the tile hadron calorimeter. The first one, the liquid Argon electromagnetic calorimeter, denote as LAr calorimeter (ECAL), can detects e/γ and record the energy from 5 GeV up to 5 TeV. It uses liquid Argon as ionizing medium and needs a cryogenic system to keep the temperature low. The second part is the steel-scintillator hadronic calorimeter, denoted as Tile calorimeter (TiCal or TileCal), by which hadronic jets such as protons, neutrons or charged pions are stopped and identified. TileCal uses plastic scintillators. Both of them are sampling non-compensated calorimeters. The system absorbs the energy of the particles that cross the detector, allowing the accurate measurement of the energy and position of electrons and photons, energy and direction of jets and missing transverse momentum. The system also allows particle identification and event selection at the trigger level. Figure 3.9 shows a cutaway view of the system, composed by the barrel calorimeter with the TiCal and ECAL sub-detectors, and the endcap of LAr calorimeter for both electromagnetic and hadronic calorimeter. The regions covered by the different parts in terms of pseudo-rapidity are $|\eta| < 3.2$ for electromagnetic calorimeter; the hadronic barrel calorimeter covers $|\eta| < 1.7$, the hadronic end-cap calorimeters covers $1.5 < |\eta| < 3.2$, and the forward calorimeters $3.1 < |\eta| < 4.9$. An extensive overview of calorimeters in particle physics is given in [4].

The Liquid Argon Calorimeter

The electromagnetic calorimeter (EM) is placed outside the solenoid magnet. It consists on a lead-liquid Argon sampling calorimeter with accordion-shape lead absorber plates and electrodes. In the copper electrodes, a signal from the ionization electrons under the electric field is registered, where the accordion geometry covers a full range in ϕ, with a fast extraction of the signal and without azimuthal cracks. Figure 3.11 shows a cutaway view of the liquid Argon calorimeter, with detailed structure.

The outstanding feature of the LAr calorimeter is the fine granularity of $\Delta\eta \times \Delta\phi = 0.025 \times 0.025$. This granularity has been carefully chosen to achieve the desired mass resolution. In the region devoted to precision physics $0 < |\eta| < 2.5$, the EM calorimeter is divided into four sampling regions:

- Presampler, with a single thin layer of Argon but no lead absorber in front, to correct the energy lost in the solenoid and cryostat wall.

- 1st Sampling, with a readout in thin η strips that provides a good resolution in the η coordinate for photon and pion separation.
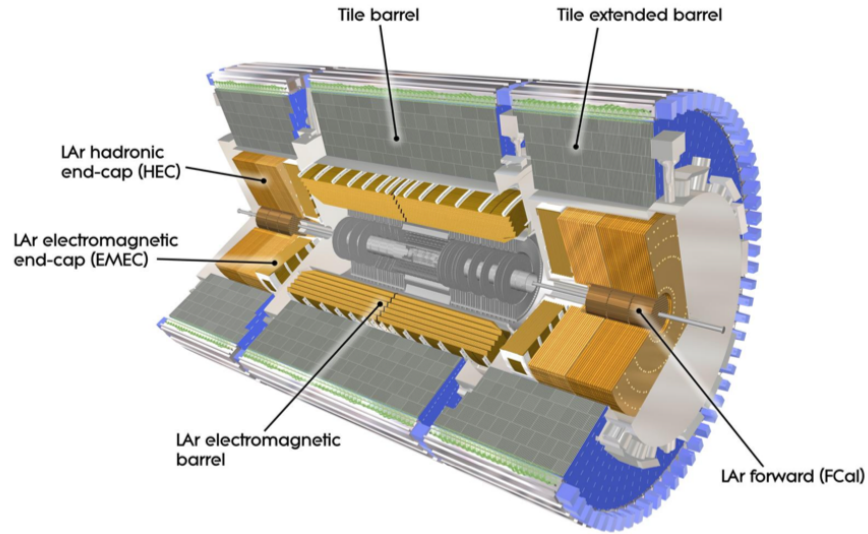
Figure 3.9: Cutaway view of the ATLAS calorimeter system. The TiCal and the ECAL compose the barrel calorimeter.
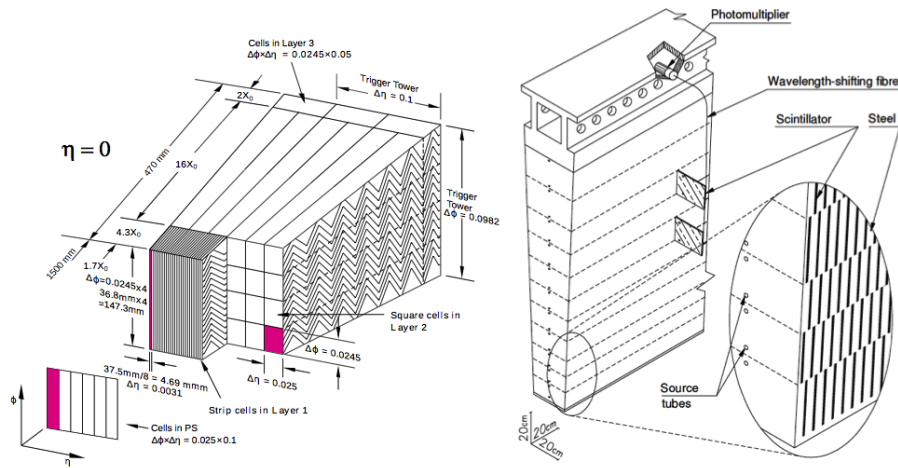
Figure 3.10: Scheme of a barrel module of the EM calorimeter with the different layers visible (left). Basic structure of the TiCal steel scintillator with the tiles, optical readout, fibers and photomultipliers (right).

- 2nd Sampling, where clusters of energy below 50 GeV are fully contained.
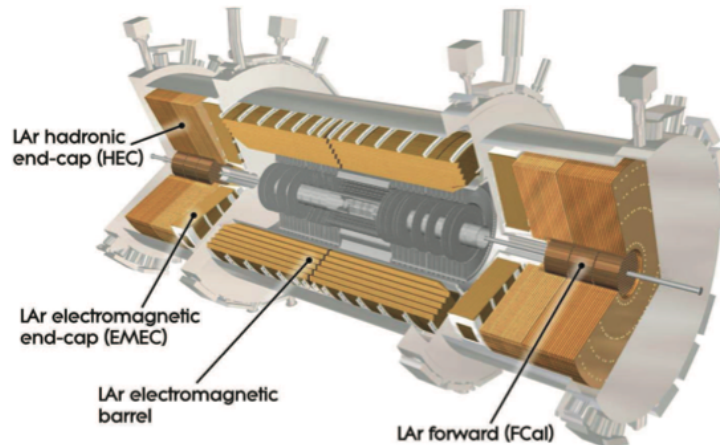
Figure 3.11: Cutaway view of the liquid Argon calorimeter.

- 3rd Sampling, only the highest energy electrons and photons will reach this depth in the detector.

In the forward region calorimeter, also liquid Argon technology can hold on the high radiation levels. The design has parallel copper plates that are absorbers and are located perpendicular to the beam. The very forward hadronic calorimeter is made of Copper and Tungsten, materials necessary to limit the width and depth of the showers from high energy jets close to the beam pipe.

The Tile Calorimeter

The Hadronic Tile Calorimeter detector (TileCal) is a sampling calorimeter that uses a structure of steel plates as absorber of various dimensions, and scintillating tiles as active material. It consists on three barrels, one central barrel of 5.6m long (LB) and two extended barrels (EB) of 2.9m long each. The EB's are divided azimuthally into 64 modules (figure 3.12). The inner radius of the detector is approximately 2.2 m and the outer radius approximately 4.2 m.

The TileCal is located in the central rapidity region, reaching out $|\eta| = 1.7$, where the LAr ends. The tiles are arranged perpendicularly to the beam line of the LHC, which provides good homogeneity in energy resolution. This sub-detector is characterized with good energy resolution over the whole ϕ range covered, good linearity from few GeV to TeV and excellent uniformity in both ϕ and η directions. The light created in the tile scintillators by ionizing particles, is read out by wavelength shifting fibers coupled to photomultipliers placed outside of the calorimeter and attached to the tiles in the radial direction (Figure 3.13).

A more detailed description of TileCal, required for a fully understanding of the detector studies presented in this work, is shown in Chapter 4.
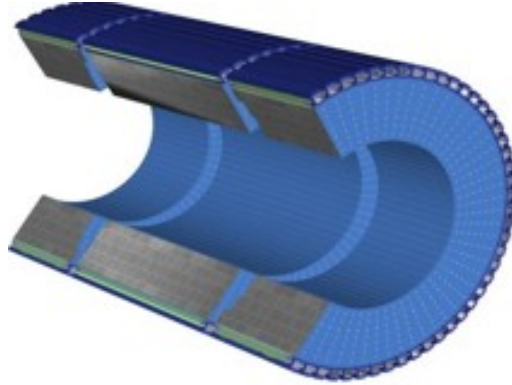
Figure 3.12: Cutaway view of the barrels of Tile Calorimeter. Both kind of barrels, the LB and EB, as well as the 64 modules, are positioned in the azimuthal direction.
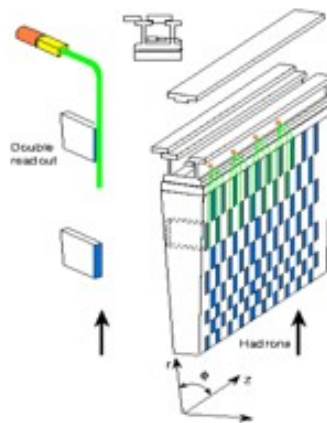
Figure 3.13: Design principle of the Tile Calorimeter.

3.3.5 The Muon Spectrometer

The muon spectrometer [5] is the outer part of the ATLAS detector. The main purpose of this subdetector is to measure the charge and energy of the muons that escape from the hadronic calorimeter. It can measure the pseudo-rapidity up to $|\eta| < 2.7$ and to trigger these particles in the region $|\eta| < 2.4$. Figure 3.14 shows
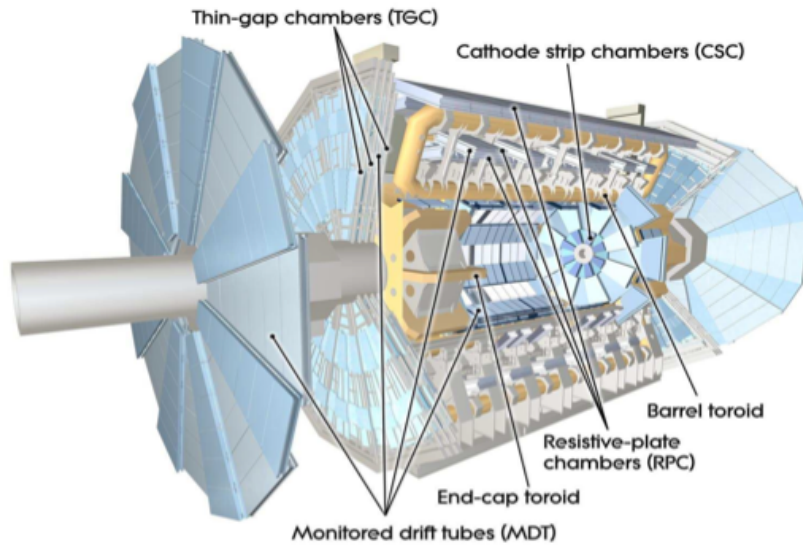
Figure 3.14: The ATLAS muon detector.

the general layout of the muon detector.

The system is instrumented separately due to the high background rates at LHC, that makes the muon drift chambers to operate with hight levels of occupancy. The barrel region contains precision-tracking chambers arranged in three cylindrical layers around the beam, named Monitor Drift Tubes (MDT), and chambers for trigger purposes, named Resistive Plate Chambers (RPC). In the transition and end-cap regions that are in front of and behind the two end-cap toroid magnets, the chambers are installed in three planes perpendicular to the beam, containing Monitored Drift Tubes chambers (MDT) and Cathode Strip Chambers (CSC) for tracks precision measurements, and Thin-Gap Chambers (TGC) for triggering purposes.

This means, that in the sub-detector, there are four kind of chambers of which two are for triggering purposes, RPC and TGC dedicated to the fast muon trigger for muons with $p_T > 6$ GeV from 40 Mhz proton-proton collisions, and two chambers for precision tracking, MDT and CSC, used for precise p_T measurements. The measure is based on the deflection of the muon tracks that traverse the large air-core toroid magnetic field. Table 3.3 shows information of the number of chambers, read-out channels and covered area required by the sub-detector. Figure 3.15 shows the side and transverse views with the location of the chambers and different components.

Table 3.3: Muon Spectrometer overview for Precision Chambers at the top, and for Trigger Chambers at the bottom.

	Precision Chambers	
	CSC	MDT
Numbers of chambers	32	1194
Number read-out channels	67 000	370 000
Coverage	$2.0<|\eta|<2.7$	$|\eta|<2.7$ (inner layer: $|\eta|<2.7$)
Area covered (m^2)	27	5500
Function	precision tracking	precision tracking
	Trigger Chambers	
	RCP	TGC
Numbers of chambers	596	192
Number read-out channels	355 000	440 000
Coverage	$|\eta|<1.05$	$1.5\ |\eta|<2.7$
Area covered (m^2)	3650	2900
Function	triggering	triggering
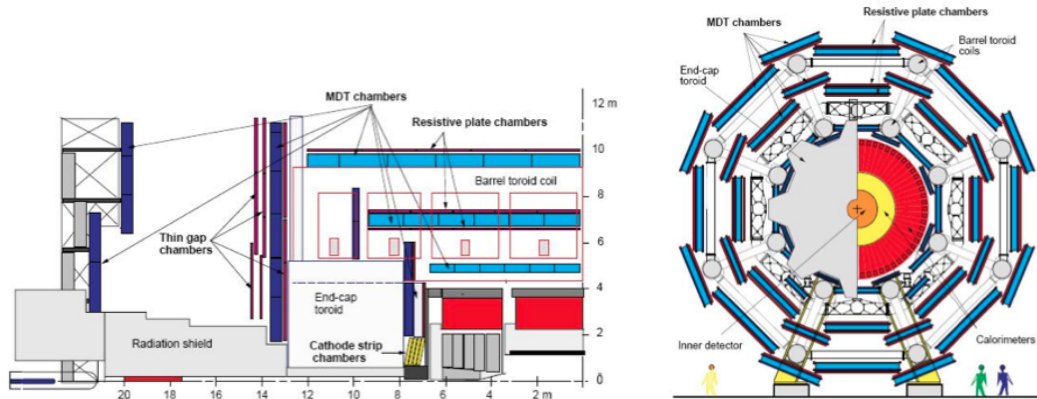
Figure 3.15: Side view of one quadrant of the muon spectrometer (left) and transverse view (right).

3.3.6   The Magnet System

The magnet system consists of two main parts: the central solenoid which provides the magnetic field for the Inner Detector and an outer system with large air-core toroids generating the magnetic field for the muon spectrometer. This second part is placed outside the hadronic calorimeter and generates a toroidal field in the barrel region, that is centered in the beam pipe. A layout of the end-caps outside

of the hadronic calorimeter and the eight toroids, with the computed magnetic field integrals as a function of $|\eta|$ predicted from the innermost to the outermost MDT layer in one toroid octant, for infinite momentum muons, is shown in figure 3.16.

The magnetic field along the z-direction generated by the central solenoid is 2 T at the interaction point. It covers 25.3 m in length and a distance between 9.4 m and 20.1 m for the barrel. The end-cap region covers a distance between 1.65 m and 10.7 m with axial length of 5.0 m. The magnetic field is not uniform, especially in $1.35 < \eta < 1.65$ barrel-endcap transition region, due to the superposition of the magnetic field produced by both magnet systems. The conductor and coild-winding technology, based on winding a pure Al-Stabilized Nb/Ti/Cu conductor into the coils, is the same in the barrel and the end-cap toroids. Both, the BT and the ECT, are enclosed in Aluminum casings. The coils are placed in the cooling modules where liquid helium at temperature of 4.5 K is used. Table 3.4, summarizes the main parameters of the magnet system. Figure 3.17 shows the external toroids magnet.
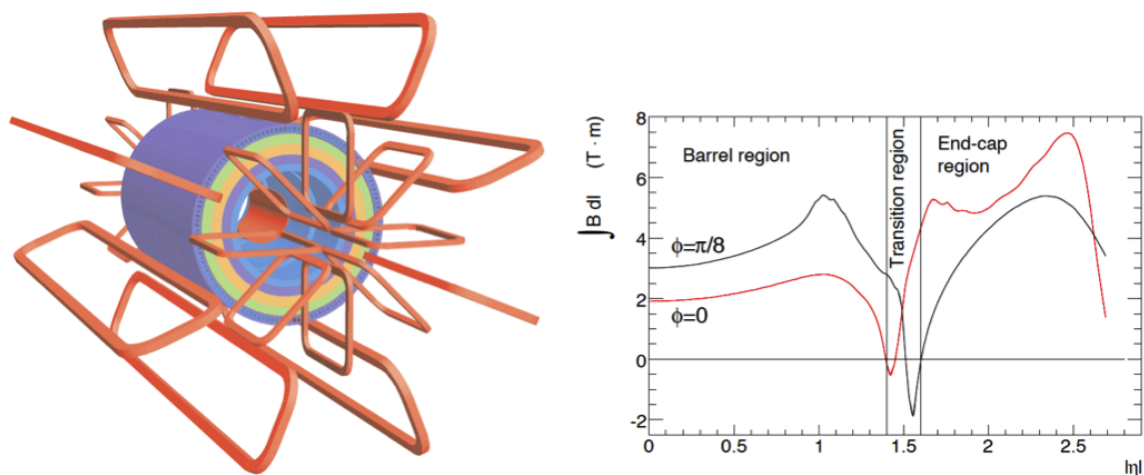
Figure 3.16: Geometry of the magnet system and tile calorimeter steel, with the eight barrel toroid and the end-cap coils (left) and the magnetic field integrals as a function of $|\eta|$ (right).
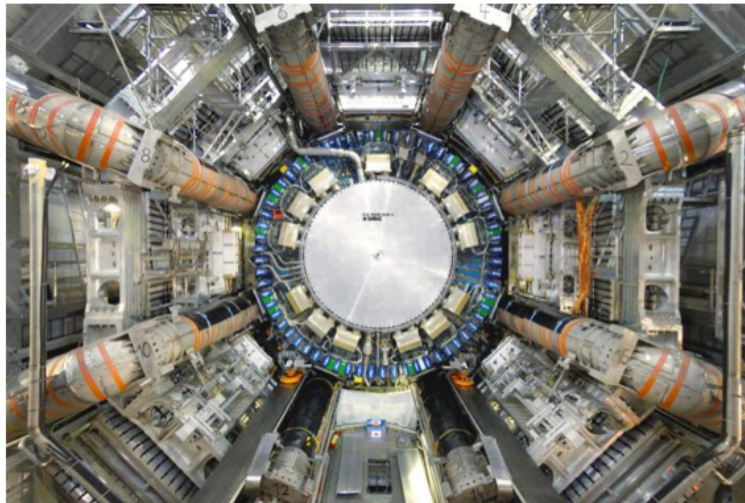
Figure 3.17: Photo with a front view of the external toroids magnet of ATLAS.

The purpose of the toroid magnet system is to bend muons that escape from the calorimeters and measure their momentum through the muon detectors. The deflection of the charged particles that traverse the toroidal field is perpendicular to the direction of the deflection provided by the solenoid magnet in the ID.

Table 3.4: Magnet system parameters overview.

	Barrel Toroid	End-Cap Toroid	Central Solenoid
Dimensions			
inner diameter (m)	9.4	1.65	2.46
outer diameter (m)	20.1	10.7	2.63
axial length (m)	25.3	5.0	5.30
number of coils	8	2x8	1
Mass			
conductor (tons)	118	2x20.5	3.8
cold mass (tons)	370	2x160	5.4
total assembly (tons)	830	2x239	5.7
Coil			
central field			2.0 T
field integral	2-6 Tm	4-8 Tm	

3.3.7   Data Trigger and Acquisition in ATLAS

The aim of the ATLAS Trigger and Data Acquisition system (TDAQ) is to reduce the rate of candidate collisions from 40 MHz to around 200 Hz without lost of interesting events, performing a selection of a fraction of events of interest and storing them. The ATLAS TDAQ is based on three levels of online event selection. Each level of trigger refines the decisions made by the previous level reducing the amount of data. The trigger system selects events by identifying signatures of muon, electron, photon, jet, tau and B meson candidates. It allows as well, to use global event signatures, such as missing transverse energy.

Level 1 trigger (L1) is a hardware trigger based on information coming from the calorimetry system and the muon chambers. It must define the region of interest (RoI) for each event, which are the places where the possible objects of interest might be present. The event information within the RoIs is passed to the L1 trigger from the read-out buffers (ROBs) to the second level trigger (L2). The time in which data of all sub-detectors can be stored in a pipeline (latency), is 2 μs that leads to a target rate of 75 kHz.

L2 is a software based on RoI trigger, which only considers the information in which L1 confirms the existence of any RoI. It uses its full granularity and the ID to make decision. It accesses selectively data from the Read-Out Buffers (ROB), to the data required, in order to make the L2 decision. All the events passing the L2 are collected from the ROBs by the so-called Event Builder and passed to the third trigger level, named Event Filter (EF). The target rate in L2 is kHz, with a latency of 1 ms to 10 ms.

Level 3, is named the Event Filter (EF), which takes events selected from L2 trigger. The EF reduces the rate and determines if the event is permanently stored. The algorithms used in the EF are computed offline. The EF runs on a computer farm near the ATLAS pit, which allows for a relatively long decision time of $\sim$1 second. Full event information is accessed by the EF and its target rate is around 200 Hz. Figure 3.18 shows the three different levels of which is composed the system. The software in which these tree-levels triggers are based, is called the High Level Trigger (HLT).

3.4   Particle Reconstruction

The complex ATLAS detector systems and object oriented software allow the particle reconstruction and identification for the experiment. The main parameters and particle reconstruction performed in the different parts of the detector, which are needed for physic analysis are described below.
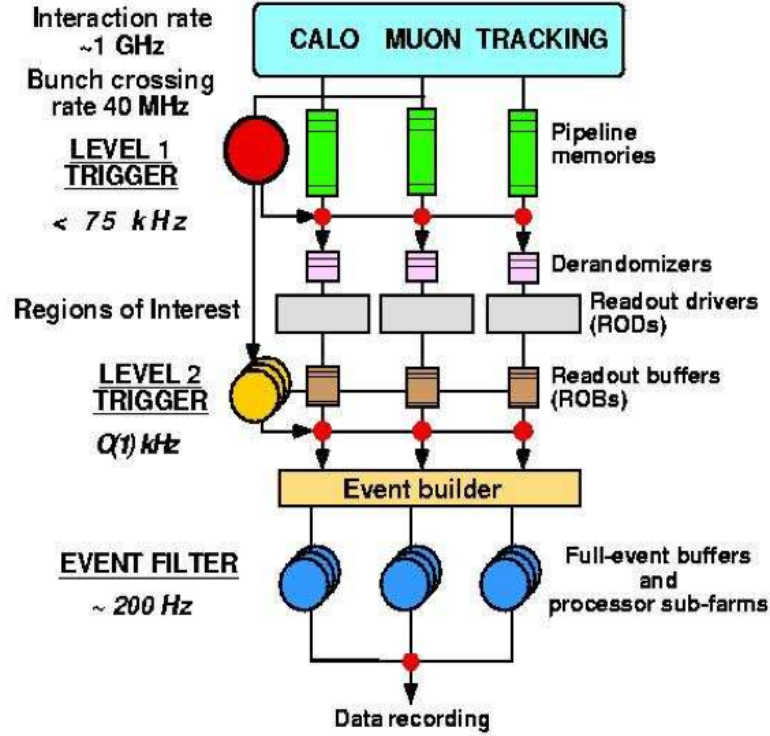
Figure 3.18: Diagram of the trigger and data acquisition system.

3.4.1   Track and vertex reconstruction

Track and vertex reconstruction are performed within the ID. Due to the solenoid magnetic field, helical trajectories are parametrized inside the ID using this set of five parameters:

- Transverse impact parameter, d_0.

- Longitudinal impact parameter at the interaction point, $z_0 \sin\theta$.

- Azimuthal angle, ϕ.

- Polar angle, $\cot\theta$.

- Inverse transverse momentum, q/p_T, being q the charge of the track.

As the coordinates in ATLAS are given regarding the origin (0,0,0), they are expressed as $\pi = (d_0, z_0, \phi_0, \theta_0, q/p)$.

The track reconstruction starts with the hit information from 3 layers of the Pixel detector and the first layer of the SCT sub-detectors, where the track is seeded. Then, the track is extended to the other parts of the SCT where a fitting is performed and becomes track candidate. The chosen tracks are extrapolated to the TRT and refitted with full information from the three detectors, after a vertex algorithm is used to reconstruct the primary vertex. Finally, a reconstruction algorithm is applied to identify secondary vertices and photon conversion.

3.4.2   Jet reconstruction

Jet reconstruction follows three steps in calorimeters, clustering, jet finding, and energy calibration. The first one starts from each calorimeter cluster reconstructed by the topological cluster algorithm, where the seed cells require high energy deposits: all the neighboring cells are associated to the cluster. The next-to-next neighboring cells are added if certain conditions are fulfilled. A four-vector parameter (E, p_x, p_y, p_z), is reconstructed with null cluster mass.

To find the jet, each cluster is associated in a cone based on the seed. Then its centroid is calculated and the cone around the new centroid is redrawn. After finding a stable cone a split-merge algorithm to separate jets is applied, depending on the energy fraction and the overlapping region.

The distance between cluster a and cluster b in the $p_T - R$ plane (d_{ab}) is,

$$d_{ab} = \min(p_{T,a}^{-2}, p_{T,b}^{-2}) \frac{\Delta R(a,b)^2}{R^2} \tag{3.4}$$

where $\Delta R(a,b) = \sqrt{(\Delta \eta_{ab}^2 + \Delta \phi_{ab}^2)}$, and $R = 0.4$ is the distance parameter to perform jet finding. From this cluster information, the *anti-k_T* algorithm [11], allows a successive recombination of pairs of clusters in an iterative procedure in order to increase the relative p_T. The cut in ΔR is real, which means that particles are not associated if they are outside the distance R.

Finally an energy calibration is required since the observed energy does not represent the energy from its original parton, quark or gluon jet. It has to consider the energy loss due to a non-detected neutron, the effects from noise, presence of death material, cracks on the calorimeter and the bending of the tracks inside the jet cone due to the solenoid magnet. Another issue to consider is the increase or energy loss due to Initial State Radiation (ISR) and Final State Radiation (FSR), pile up or underlying events. For this purpose, calibration parameters are derived from data, using energy-balanced events like $\gamma + jet$ or *di-jet* events, which allow to check the reconstructed energy of the jet as a function of the p_T and η.

3.4.3   Electron reconstruction

Electron reconstruction is performed with the calorimeters. It starts with a seeded electromagnetic cluster with transverse energy on top of 2.5 GeV. The tracks coming from the inner tracker are extrapolated to the electromagnetic calorimeter, and a matching is performed. Then, the ratio between the energy of the cluster and the momentum of the track is required to be < 10, to confirm that the electromagnetic jet comes from an electron. 93% of the true isolated electrons with $|\eta| < 2.5$ and $E_T > 20$ GeV, remain as electron candidates.

3.4.4   Muon reconstruction

Based on different track reconstruction, three strategies for muon identification are used in the ATLAS experiment. They can be classified as:

- **Standalone:** Muons reconstruction is named *standalone* when only the MS is used. Tracks found in the MS are extrapolate to the beam line. The muon track reconstruction is defined by the MS acceptance, within $| \eta |< 2.7$. The track segments consist on straight lines in a single MDT or CSC station. The candidates are built from segments, starting from the outer and middle stations and extrapolating back through the magnetic field to the segments reconstructed in the other stations.

- **Segment-tag:** it is the combination of an ID track and a MS segment, which is a straight line track in an ID muon station. ID tracks are extrapolated to the inner muon stations and linked to reconstructed muon segments. The reconstructed muons have improved the *standalone* muon reconstruction, because at momenta below to 6 GeV, muon tracks do not always reach the middle and outer muon stations. In the barrel/end-cap transition region with $1.1 < |\eta| < 1.7$, the middle stations are missing for the initial data taking and the standalone reconstruction efficiency is therefore reduced in this region. This, together with the difficulty of the regions with $|\eta| \sim 0$, where the geometrical acceptance of the muon stations is reduced, make also more useful the segment-tag identification.

- **Combined:** The muons that arrive to MS also leave their signatures in all sub-detectors of ATLAS, including the ID and the calorimeters. An optimal muon identification is performed by building tracks in the different layers of the MDT, then extrapolating the tracks into the ID, taking into account the energy loss and multiple scattering in the calorimeters. A matching between the extrapolated track and the tracks found in the inner tracker is performed.

In this case, the reconstructed muon is named *combined*.

The combination of the MS with the ID tracks, must be in the $| \eta |< 2.5$, as defined by the ID acceptance. This combination improves the momentum resolution for tracks with $p_T < 100 GeV$. The MS track parameters are determined at the inner stations, which yield the first set of measurements in the MS. The track is then propagated back to the interaction point and the momentum is corrected for the energy loss in the calorimeters and in the ID. The matching condition for the combined muons ($\chi^2_{\mathrm{matching}}$) could be defined as

$$\chi^2_{\mathrm{matching}} = (T_{MS} - T_{ID})^T (C_{MS} + C_{ID})^{-1} (T_{MS} - T_{ID})^T, \qquad (3.5)$$

T being a vector of track parameters, and C is the covariance matrix obtained from the fit. *Combined* muons can be found by matching standalone muons to nearby Inner Detector tracks and then combining the measurements from the two systems. Then, tagged muons are found by extrapolating Inner Detector tracks to the spectrometer detectors and searching for the nearest hits.

Figure 3.19, shows the path of a low-p_T and a high-p_T muon in ATLAS. The magnetic field curves the low-p_T muon trajectory, sending it to the innermost MS stations.

3.4.5   Tau reconstruction

Tau lepton reconstruction is of especial interest for this work. The main background for these particles in ATLAS is represented by QCD jets, so it is required to distinguish tau from jets with high rejection power. Taus are characterized because they exhibit a collimated calorimeter cluster, low charged tracks multiplicity and a displaced secondary vertex. Their decays through hadronic channels represent the 65% ($\tau \to \pi^{+/-} n\pi^0 \nu$), while the other 35% corresponds to leptonic channels ($\tau \to e\nu$ or $\tau \to \mu\nu$). These leptons have a short lifetime of 2.9×10^{-13}s. Reconstruction of tau leptons is performed from the hadronic decay τ-jets, since it is more difficult to distinguish leptonic decaying taus from the leptons that arrive from the interaction point. The taus decaying hadronically can be classified by to the number of charged tracks (N_{track}) present in their decays: 1-*prong* (τ_1), being 85% and having only 1 charged track inside the jet, and *multi-prong* (τ_3), being 15% and requiring $N_{\mathrm{track}} \geq 2$. Table 3.5 shows the decay modes of the hadronic decaying τ.
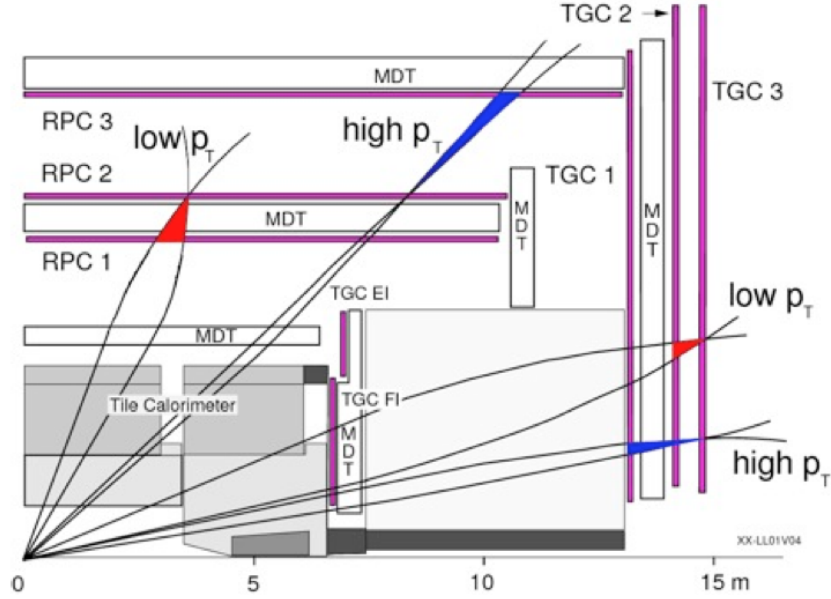
Figure 3.19: Representation of the path of a low-p_T and a high-p_T muon in ATLAS

The number of isolated charged tracks (1 or 3) characterize the τ-jets, as well as an intermediate jet width, e/γ jet $< \tau$ jet $<$ gluon/guark jet. They have an odd number of isolated tracks, inside the core region, with collimated energy in the electromagnetic calorimeter, and deposit part of the energy inside the hadronic calorimeter, due to the initial pions produced.

The reconstruction starts, applying the $anti$-k_T algorithm to calorimeter jets that have $|\eta| < 2.5$ and $p_T > 10$ GeV. Then, a four-vector parameter is calculated based on the topological clusters associated to the jet, the mass being zero. Energy track must have $p_T > 1$ GeV and be associated to the τ candidates if they are within the distance $\Delta R < 0.2$. The number of pixel hits must be ≥ 2. The number of pixels in addition to SCT hits must be ≥ 7, with a distance of the closest approach of the track to the reconstructed primary vertex < 1 mm, and $|z_0 \sin \theta| < 1.5$ mm.

The energy of the τ-jet is represented as the energy deposition within $\Delta R < 0.4$, inside the jet after correcting to the particle level jet. The energy calibration is applied by using MC. Figure 3.20 shows an example of a reconstruction of a τ-jet inside the detector.

Table 3.5: Branching ratios of the hadronic decaying tau jet.

1-prong hadronic decay mode	
$\tau^- \to \pi^- \nu_\tau$	18%
$\tau^- \to \pi^- \pi^0 \nu_\tau$	40%
$\tau^- \to \pi^- \pi^0 \pi^0 \nu_\tau$	15%
$\tau^- \to \pi^- \pi^0 \pi^0 \pi^0 \nu_\tau$	2%
others modes with K^-	2%
multi-prong hadronic decay mode	
$\tau^- \to \pi^- \pi^+ \pi^- \nu_\tau$	15%
$\tau^- \to \pi^- \pi^+ \pi^- \pi^0 \nu_\tau$	7%
others modes with K^-	1%
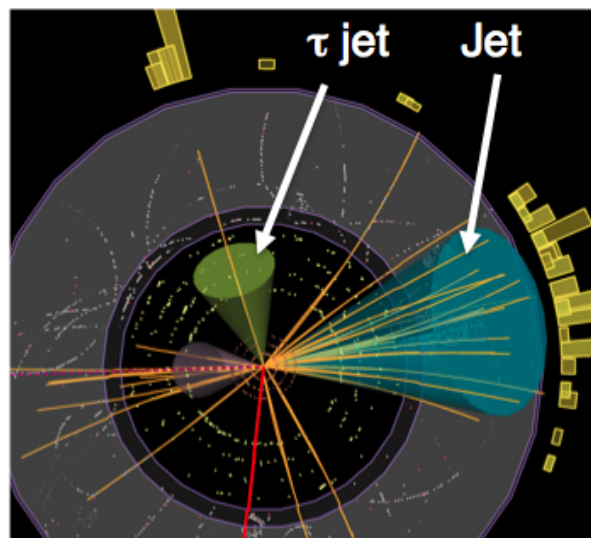
Figure 3.20: Reconstruction of a tau jet inside the detector, showing the different topology of a τ-jet and a gluon/quark jet.

3.5   ATLAS Computing

In order to perform the physic analysis of the stored data, analysis tools made up of software and middleware have been developed by the ATLAS collaboration [12]. The complexity of the whole experiment requires tailored software developments. This is divided in two main building blocks, the *Athena* software framework and the *Distributed Computed* tools built on top of Grid middleware, developed to store and distribute the huge quantities of data generated by the LHC.

ATLAS offline software, based on the *Athena* framework, can be used to perform tasks as:

- simulation of possible physic performed in the detector, detector response to different actions, and trigger simulations;

- reconstruction of simulated or real data;

- analysis of the detected reconstructed events.

3.5.1   Athena framework

The *Athena* software [13] has been developed for the ATLAS experiment inside a framework that allows communication between different algorithms. It is a control framework based in the Gaudi architecture, a tool that provides interfaces and services for building high energy physics experiment frameworks in the domain of event data processing applications [14]. *Athena* framework allows dynamic libraries loading and it is organized in modules that allow different configuration of various algorithms to be executed. These files provide the user the ability to specify what is needed for the algorithms using Python scripting, allowing to determine the run-time configuration of the algorithm used, specifying which algorithms need to be run and in which order.

To run *Athena*, it is necessary in addition to the *JobObtions*, a certain environment set by sourcing the Configuration Management Tool (CMT), access to databases and command lines for arguments configuration. The CMT is used by ATLAS [15] to manage configurations, build software and to set up the user environment. This tool supports the decomposition of the software into packages, or groups of packages. The external packages are interfaced to CMT by defining a glue package, where configuration specifications for this external package are detailed.

The *Athena* software aims to produce generation, simulation, digitization and reconstruction of the events generated or detected in the experiment. The generation is based on different random number MC generators. The simulation, digitization and reconstruction algorithms of the systems can be implemented independently from each other. The tracking of the produced particles along the detector used Geant4 toolkit [16]. The digit-objets are stored after the digitization, where the electronic of the detector on the objets is simulated. The reconstruction uses various algorithms for track fitting, pattern recognition and energy measurements, among other calculations, using the digitized information. From the Raw Data Object (RDO) in the raw channels, it is possible to refine the data. The output of the reconstruction are data files named Event Data Summary (ESD) files, which contain more detailed information of an event for reconstruction and calibration.

From ESD, it is possible to obtain Analysis Object Data (AOD) files, which are important for physics analysis and then the Derived Physics Data (DPD), intended for interactive analysis. The chain followed by the Athena software is illustrated in figure 3.21.
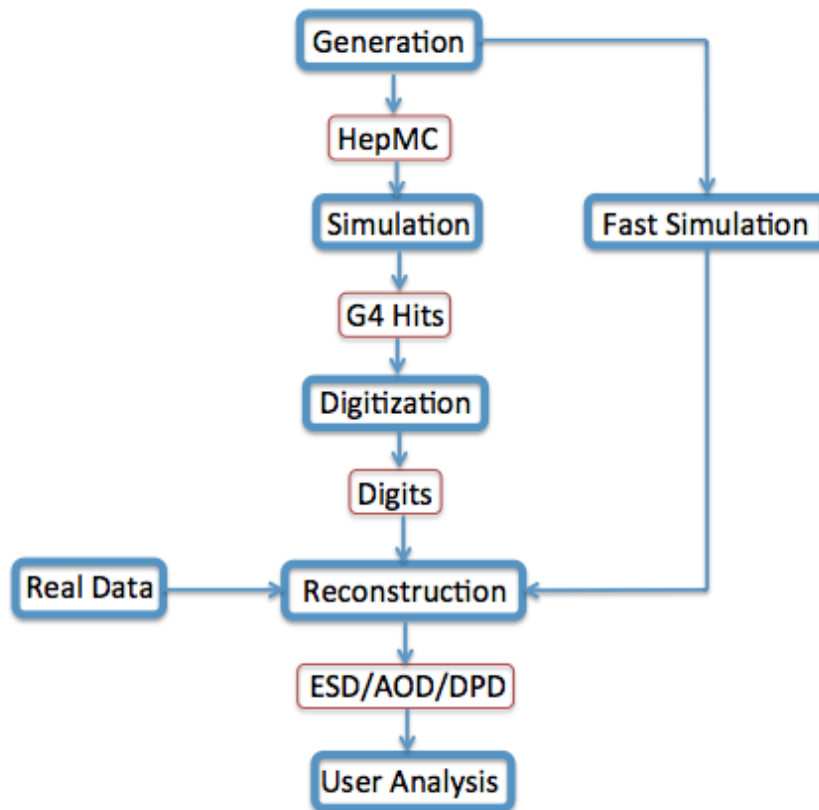
Figure 3.21: Diagram of the Athena software chain. In blue squares are the main steps: generation, simulation, digitization and reconstruction.

3.5.2 GRID computing

The huge amount of data that the LHC generates, requires large storage and computational resources for distribution and analysis. For this purpose it has been developed and implemented a distributed computational data grid under the name of LHC Computing Grid project (LCG). This computing resource provides the infrastructure needed for the physics analysis and simulations.

The raw data from LHC is recorded first in the Tier-0 center at CERN, where a calibration is performed, a first reconstruction of data and its storage. Then,

a second copy of the raw data is distributed to Tier-1 centers that manage the permanent storage of raw data, and simulated and re-processed data. Tier-1 centers provide computational resources for re-processing and analysis, and allow to send data to Tiers-2 centers for permanent storage. These, provide computational resources and storage services for Monte Carlo event simulations and allow to final users to perform analysis. In the end, Tier-3 centers are allowed to process and analyze the LHC data, in facilities at universities and laboratories.
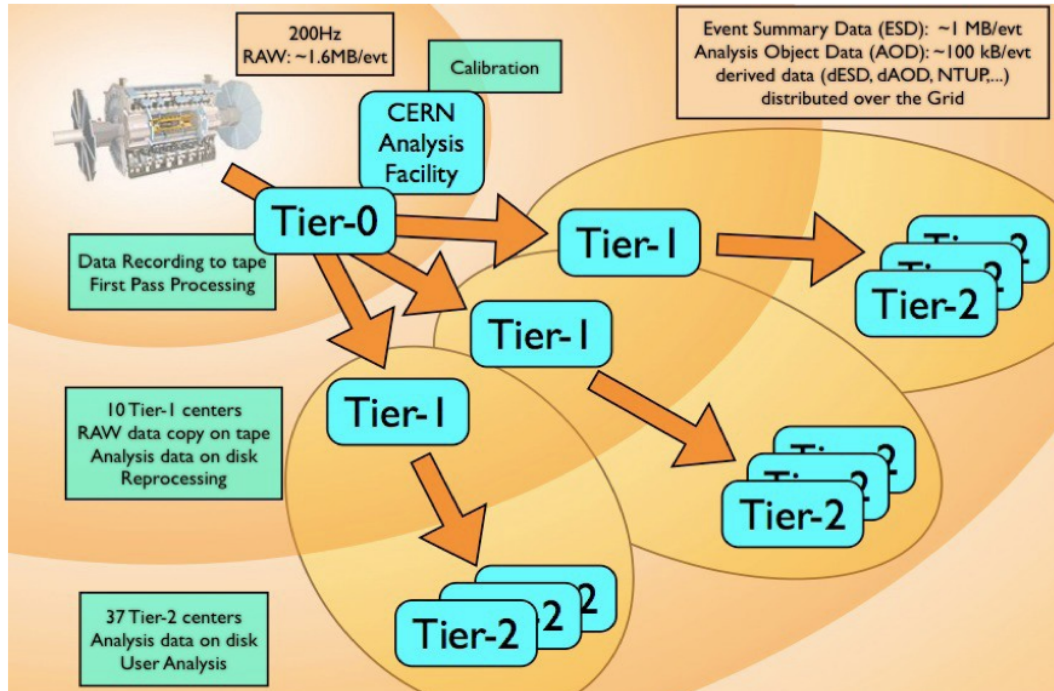
Figure 3.22: Sketch of ATLAS tier centers distribution and amounts of the different kind of data stored.

The distributed analysis is performed starting with a pre-distribution of data to sites, where jobs are splitted. To submit data, different ways can be used such as *Panda* system, which centralize MC simulation and data reconstruction, via the *Distributed Data Management* (DQ2), which centralize data traffic, or via *Distributed User Analysis*, which de-centralize individual analysis.

The LCG project involves complex software and hardware developments, where a large bandwidth is needed for data distribution. The software must be compatible with different hardware systems and guarantee coherent software in all computers. It must manage and process to avoid missing or corrupted data, and provide mechanisms for data access.

Chapter 4

Muon Studies with TileCal & Level-2 Trigger

This chapter summarized in two parts, some contributions to the commissioning of the Tile Calorimeter (TileCal) and Muon Level-2 Trigger systems in the ATLAS detector. The first part is dedicated to TileCal, describing the sub-detectors components of interest for the understanding of the presented study. Following this, the description and results on data quality assessment performed in May 2009 are presented. These results were intended for commissioning and preparation of the TileCal, before the start up with real data taking. The objective during commissioning was to identify the components of the TileCal front-end electronic that fail or have any problem during operation. The second part of this chapter is devoted to studies with TileMuID, algorithm based on TileCal and mainly used for commissioning in the Muon Level-2 trigger. The chapter also contains the description of the trigger and results of some tests performed with TileMuID algorithm, using cosmic rays taken in fall 2009. Muon Level-2 Trigger results presented in this chapter take part of an ATLAS note [27].

4.1 TileCal Electronics and Calibration System

As explained in section 3.3.4, the Hadronic Tile Calorimeter is a part of the ATLAS calorimeter system, which measures the energy of neutral and charged particles. The system consists of metal plates named absorbers, where as a result of the particle interactions, incident energy is transformed into a shower of particles that are detected by the sensing elements, the other important part of the calorimeters. Figure 4.1 shows a section of the ATLAS detector pointing to TileCal. The TileCal sub-detector is composed of 3 barrels, one central barrel with a length of 5.6 m named Long Barrel (LB) and two Extended Barrels (EB) with a length of 2.9 m

each. The inner radius of the detector is approximately 2.2 m and the outer radius is 4.2 m. Each barrel is divided azimuthally into 64 wedges, the modules. The active material are tiles of scintillating plastic, which emit light as a consequence of the energy deposition in them. Wave-Length Shifting (WLS) optical fibers collect the light produced in the tiles. The fibers have been doped with special elements that absorb the mainly blue light from the scintillator and reemit the light in the green interval. A fraction of this green light is captured in the fiber by internal reflection at the core-cladding boundary. The light is transmitted through the fiber to a photo-multiplier tube (PMT). To highlight the light yield, the other end of the fiber is coated with Aluminum to make a mirror surface. Figure 4.2 shows different photos of the sub-detector during its assembling. On the left and center, the WLS optical fibers used to collect the light produced in the tiles can be observed. On the right, the whole view of TileCal is shown.
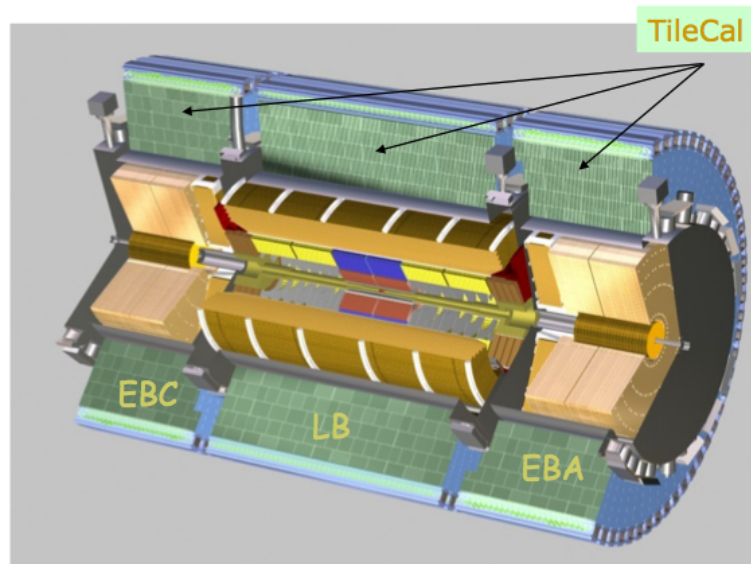
Figure 4.1: Cutaway view of the ATLAS detector. The barrels of TileCal correspond with the green color parts of the scheme.

4.1.1   TileCal Front-End Electronics

The TileCal front-end electronics is placed in the so-called drawers inside the girders which support the calorimeter modules. These are compact structures coupled forming a new structure named super-drawer, located inside the back-beam region of the Tile Calorimeter modules and containing the photomultipliers

Figure 4.2: TileCal sub-detector is made in a sandwich-like structure where scintillator tiles are placed between metal sheets. On the left, photo of the WLS fiber bundles. In the center the image of the fibers during assembly. On the right a whole view of the assembly of the TileCal.

blocks, the HV distributors and the pipelines. There are 256 super-drawers, one per each half barrel module and per each EB module. Figure 4.3 shows the sketches of the drawer (left) and the photomultiplier block (right). Figure 4.4 shows the interface location in the electronic drawer.
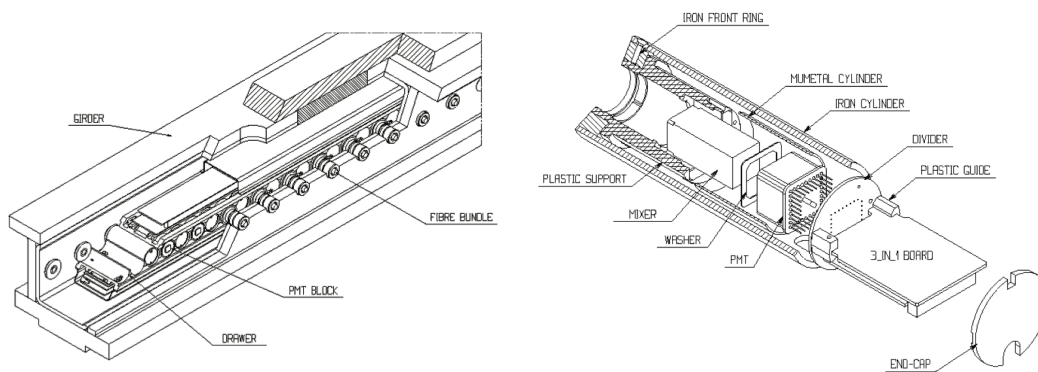
Figure 4.3: Sketches of the drawer (left) and the photomultiplier block (right) with the different parts labeled.

PMTs

The photomultipliers transform light signals from the calorimeter cells into electronic signals. Each PMT block is composed, basically, of a photomultiplier tube, a high voltage divider, a 3-in-1 card and a light mixer, the assembling corresponds to one channel for read-out. There is one PMT block assigned to each of the about 10000 fiber bundles in Tile Calorimeter, the main characteristics and functions of the blocks components mentioned above, are:
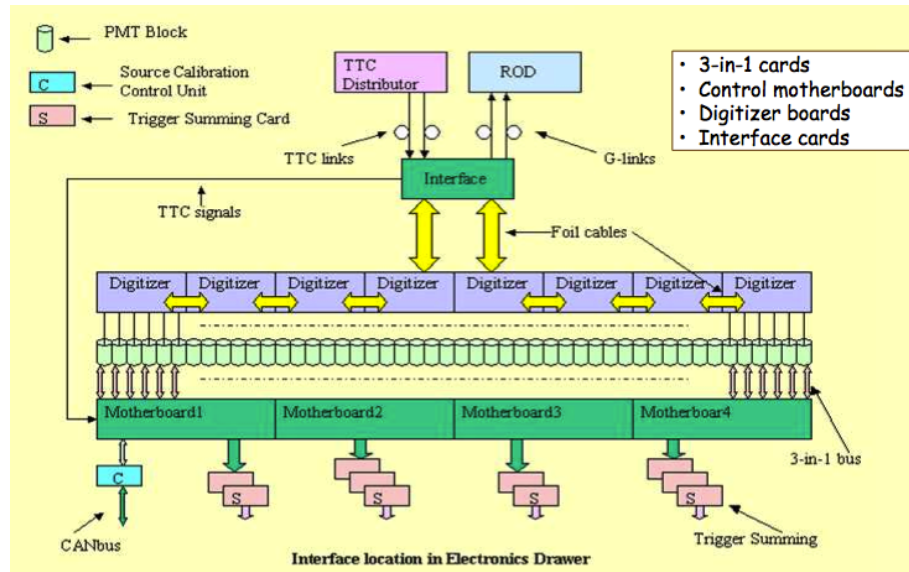
Figure 4.4: Sketch showing the front-end electronics in TileCal. It is composed of 3-in-1 cards, control motherboards, digitizer boards, interface cards and PMTs.

- **Photomultiplier tube:** it is responsible for converting the light signal from the fiber bundles into electric charge. It works linearly in a wide range, from very low signals, as the ones from $low\text{-}p_T$ muons, up to the signals from very energetic jets.

- **Light Mixer:** it is responsible for mixing the light that arrives from the fibers in the bundle, in a way that there is no correlation between the position of the fiber and the area of the photocathode receiving the light.

- **3-in-1 Board:** its main function is to provide a high and a low gain shaped pulse for the digitizer boards, the slow integration of the PMT signals for monitoring and calibration, and the pulse for the charge injection calibration system.

- **Magnetic Shielding:** it must prevent variations in the gain as a result of the residual magnetics fields from the ATLAS solenoid and toroids.

- **HV Dividers:** they divide the high voltage between the dynodes of the PMT. The TileCal divider is used as well as a socket to allow the connection of the PMT to the front-end electronics without any interconnecting wires.

Digitizer System

Fast pulse signals from the 3-in-1 cards are digitized and a digital pipeline is sent down. On receipt of a L1 accepted signal, the digitizer boards capture an event frame, which is a string of digitizations. The events or data frames are stored locally and queued for transmission to the interface link. The data are presented to the digitizer boards by the 3-in-1 system, delivered with two versions of each signal, which are a high and a low gain version of 64 gain ratio. This analog data is digitized and stored temporarily. The digitizers, formed mainly by Analog to Digital Converters (ADCs) for Trigger and Timing Control (TTC) information, receipt and customize the input from the Data Management Unit (TileDMU) [17]. The TileDMU is in charge of reformatting and reordering the digitized data and send them to the interface links. Each TileDMU manages 3 ADCs, and each digitizer board has 2 TileDMUs. Therefore there are 8 Digitizer boards for CB super-drawers and 6 for EB super-drawers.

Interface Links

The interface links have two main functionalities:

- Receive the TTC information and distribute it to digitizers equipped with the TTCrx chip (the TTC receiver).

- Receive the data from the 8 digitizer boards in a drawer, deserializing them and sending them through an optical link to the input stage of the RODs.

To provide redundancy, dual channel read-out were implemented with two optical fibers that provide the same TTC and read-out information.

4.1.2   TileCal Back-End Electronics

In the back-end electronics the main element is the Read-Out System. It is composed of 32 Read-Out Driver (ROD) cards, based on a custom 9U VME64x boards equipped with up to four Processing Units (PUs). The RODs are placed in 4 crates corresponding to the 4 TileCal partitions for data acquisition. Each partition is managed by a TTC crate, equipped by standard TTC modules for the LHC experiments. The PUs process the data coming from the TileCal front-end electronics, to feed the second level trigger with information of energy deposited in the calorimeter and other relevant quantities.

Read-Out Drivers (ROD)

The ROD is a 9U VME module that receives as input the fibers information from the interface links, which contain the digitized samples of the electronic pulses at

a L1 rate of 100 kHz. In one ROD there are 8 input fibers from 8 different super-drawers, which means that the whole calorimeter needs 32 RODs. The RODs process the data in real time and send them to the L2 trigger, being responsible for error detection and busy generation, among other tasks. They are equipped with Digital Signal Processors (DSPs), which run reconstruction algorithms that can be applied online to processed information in real time, apart of the raw data sent to L2 trigger. Figure 4.5 shows a picture of the ROD motherboard.

The DSPs can apply different algorithms depending on the trigger type of the data (physics, pedestal, laser, charge injection) and they can be programmed in high-level languages, such as C language. A reconstruction algorithm, the so-called Optimal Filtering, which gives as output the energy, timing and a quality factor for all the processed channels, is implemented in the ROD DSP. In addition, two other algorithms for HLT have been implemented. The first, is an online low-p_T muon tagging algorithm that is able to identify muons only from the deposited energy in TileCal and outputs the coordinates of those muons to L2 trigger in order to define secondary RoIs [30]. The second, is an algorithm to compute the transverse energy per super-drawer.

The Read-Out Drivers main features can be summarized as:

- **Data processing:** raw data from the first level de-randomizers at the L1A event rate of 100 kHz. The ROD provides the energy, timing and a quality factor to the next trigger level by processing the data with the algorithms implemented in the PUs.

- **Trigger:** TTC signals are presented at each module, providing ROD L1 bunch crossing identifier and trigger type.

- **Data links:** at L1A event rate of 100 kHz, the ROD sends the data to the Read-Out Buffers (ROBs), using the standard ATLAS Read-Out Links (ROLs).

- **Error detection:** the ROD checks that the owner Bunch Crossing Identification (BCID) and L1 identification (L1ID) number, match with the numbers received from the front-end. An error flag is set if a mismatch is detected.

- **Busy generation:** the Trigger and Busy Module (TBM) provides a busy signal, which stops the L1A generation, performing an OR operation with the ROD busy signals coming from all the RODs in a partition.

- **Local monitoring:** part of the data can be read through VME for monitoring tasks without introducing dead-time or additional latency.
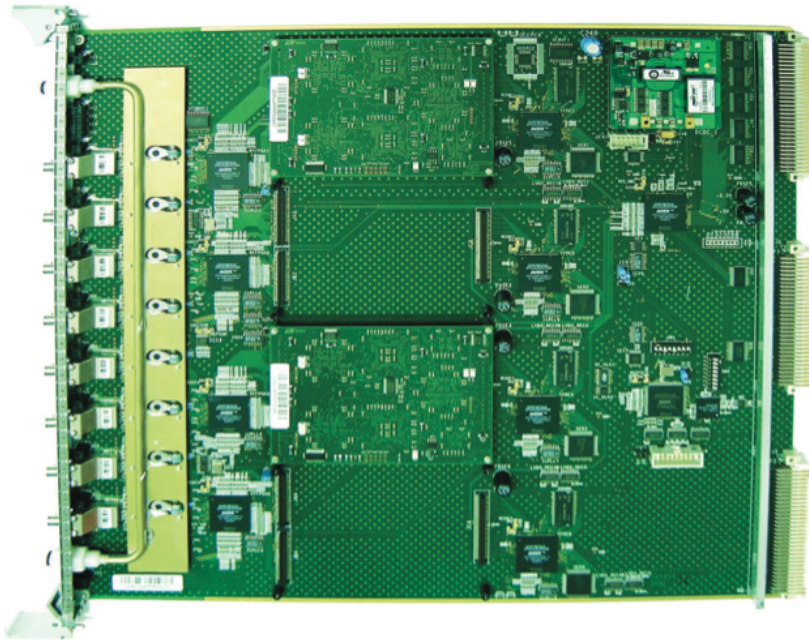
Figure 4.5: Picture of a ROD motherboard. On the left, one can see 8 inputs to read-out the data from 8 super-drawers.

Optical Multiplexer Board (OMB)

The data coming from the front-end are transmitted to the back-end with redundancy. Two fibers carry the same data from the interface cards to the ROD. This redundancy is mandatory in order to prevent the effect of the data corruption in the front-end electronics due to damages caused by the radiation. To exploit it, an Optical Multiplexer Board (OMB) [18] has been implemented. It is a 9U VME module that selects data from one of the two front-end links and transfers it to the ROD, which can be used as well to inject data to the ROD for test purposes. Figure 4.6 shows diagrams of the two working modes of OMBS: test mode (left) and injector mode (right).

4.1.3   TileCal Calibration System

To calibrate and monitor the calorimeter, various systems have been designed for the different elements in the electronic chain [19]. They are summarized as:

- **A Cesium (Cs) radioactive source system**, used to measure the quality of the optical response of each calorimeter cell, to equalize the signal response

Figure 4.6: OMB Check Mode (left) and OMB Injector Mode (right).

and to monitor it with time. It allows to scan all the tiles through a small pipe. When the source crosses a tile, the scintillation light is collected and transformed into charge by the PMT. In this way, all the channels are inter-calibrated. It is possible to set the high voltage of all the channels to the desired value of the conversion factor between particle energy and PMT pulse charge.

- **A laser system**, used to calibrate and monitor the response of the PMTs, in particular the stability of their gains and their global linearity. This system is also used for timing purposes. It allows monitoring the response of the mixers and PMTs to light.

- **A Charge Injection System (CIS)**, used to calibrate the relative response of the PMT signal readout electronics and to track any variation with time. The CIS makes possible to send charged pulses to the digitization electronics, so linearity and gain can be checked. There is also an integrator that monitors the overall response over time.

During commissioning, reconstruction and monitoring algorithms were executed to provide online event display and histograms. In this way, it was possible to monitor the data quality during calibration and other detector operations. High Level Trigger algorithms were also used to provide data streams adequate for different purposes such as alignment and calibration elements. Figure 4.7 represents the optical and electronic readout system listed before.

Figure 4.7: Scheme of the optical and electronic readout, including the calibration and monitoring systems of the Tile Calorimeter.

4.2 TileCal Data Quality Assessment

During the installation and first phases of the Tile Calorimeter, a deep commissioning of the sub-detector was required, due to the number of electronic channels and the high rate of data taking to verify the correct behavior of the hardware and software systems. The commissioning was performed with cosmic muons through all the phases of the data acquisition and analysis (monitoring, reconstruction, validation of calibration signals and processing data). A set of tools were developed to allow a fast analysis of the results, with web interfaces for remote monitoring and data quality assessment [22]. These tools range from the hardware detector verification tests and the *online* monitoring to the *offline* reconstruction, allowing a fast and partly automated analysis of the results. In this section, the different evaluation processes to check the quality of the data collected with the detector are described. Analysis results using the DQ tools, that have contributed to the commissioning of the TileCal, are also shown.

4.2.1 Strategies, Stages and Tools for DQA

The Data Quality Assessment (DQA) project inside the framework of Data Preparation in TileCal sub-detector, is the process that allows to collect data in an efficiently way and to use them for physics analysis. The DQA uses tools and technologies very different one from each other, like online software, ROOT macros [20], and web interfaces that implies the need of different expertises. The data quality

tasks are based on the performance of the hardware at L1, and allow to identify issues in the operation of the detector as the convenience in the use of monitoring tools when the data are taken efficiently, or the use of special calibration runs to investigate TileCal status. The DQA process is performed in three different steps:

1. Decoding of the raw data and preparation of reconstructed quantities.

2. Filling histograms with the reconstructed quantities.

3. DQA processes that use histograms to produce quality flags.
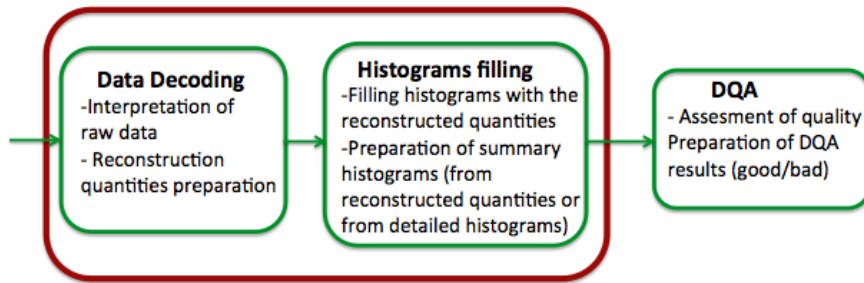
Figure 4.8: Scheme showing the DQA process.

Figure 4.8 shows an scheme with the processes of DQA. Steps number 1 and 2 are called the *Monitoring processes*, and are performed with the same application, Athena (see Section 3.5.1) and GNAM, a low-level monitoring system that interacts with the DAQ, allowing separation of common actions from the detector specific ones [21]. Step 3, is the *DQA process* itself, and it is performed inside the Data Quality Monitoring Framework (DQMF) and histogram display. The process includes the check of histograms, visualization and storage.

TileCal Runs

The data are acquired and stored by the TDAQ system and then reconstructed with the ATLAS offline reconstruction software (*Athena*). The different types of runs acquired for TileCal detector during the commissioning phase were:

- **Noise runs:** the events were taken by a random trigger. Since no signal is expected, it is possible to monitor the level of the electronic noise.

- **Charge injection runs:** a charge is injected in the electronic readout by the CIS. The charge is varied in amplitude and phase, allowing checking the front-end electronics response.

- **Laser runs:** light from a laser is injected directly in the PMTs. The data taken allow to check the presence of dead channels, the linearity of the readout chain and the detector timing.

- **Slow integrator runs:** similar to CIS runs, but the readout is performed through a parallel readout.

- **Trigger runs:** where the correct response of TileCal trigger analog output is checked.

- **Cosmic trigger runs:** cosmic muons are detected with a special trigger setup. They allow to verify the system stability and detailed offline analysis performance studies.

For any of these run types, a data quality process was developed. The data quality tests can be grouped in two macro areas, *online* and *offline* data quality. In the first, the tools used give a feedback on the status of the system in a very short time. In the second, the tools used require the reconstruction and analysis of the data by offline software, and give a feedback in a longer time-scale.

4.2.2   Online Data Quality

The *online data quality* is performed in real time, during data acquisition with the tools available in the context of TDAQ. Before the data are acquired, a series of runs are performed in order to verify the correct operation of the front-end modules, as measure of the electronic noise. The system used is the ATLAS Detector Verification System (DVS) [23], which uses TDAQ configuration database to execute the test. After verification of the proper performance of the modules and possible error identification, the detector is ready for data taking. For the different type of runs, the raw data are acquired with the TDAQ software and sent to mass storage for later offline analysis. ATLAS TDAQ allows to check the data flow at the different levels in the acquisition chain. The quality of the data acquired by TileCal is verified by different online monitoring processes, following a strategy that consists in performing online monitoring at the very first stage of the data acquisition, directly in the RODs before the TileCal data-fragments enter the event building network.A large number of detailed histograms are produced by the monitoring system of TileCal. Only a few of them are really needed to verify

the status of the detector, and the rest are complementary and may help in case of error. To easily navigate through the histograms, the Online Histogram Presenter (OHP) was developed and included in the TDAQ [25].

The are four different technologies for the TileCal detector monitoring:

1. **GNAM Monitoring:** TileCal plug-ins have been developed for the GNAM monitoring framework [24]. PMT level quantities as timing, noise, energy or pulse shapes, are reconstructed.

2. **DSP Monitoring:** dedicated monitoring code is running on the DSPs, which are responsible of the drawer read-out as explained in section 4.1.1. Quantities with estimation of the noise level or error counting are monitored for each one of the 128 TileCal DSPs.

3. **ROD Monitoring:** Each ROD module contains four read-out DSP chips, which are responsible for the read-out of eight drawers. Then, a total of 8 RODs are located in the same crate, performing the read-out of one entire section of the TileCal. A single-board computer in each crate monitors the global status of the crate, including the number of events flowing and error counters.

4. **Monitoring based on Athena:** the online monitoring uses the offline reconstruction framework *Athena*, (section 3.5.1). The access of the system to tools as databases or calibration constants, allows to develop with offline-quality a monitoring application for reconstruction quantities. This tool is especially used during the long cosmic runs, where muon tracks are reconstructed with quantities as the energy deposition.

4.2.3   Offline Data Quality

The *offline data quality* is performed on recorded data as soon as they are available, with a full reconstruction of the events. This allows to study in detail the behavior of the TileCal as a function of time. The process is carried out in three different steps:

1. **Reconstruction and monitoring.** A few quantities are monitored producing detailed histograms. Those include checks on CRC errors, corruption of data stream, dead channels, measurement of the noise level and the measurements of the signal amplitude over injected charge ratio for the CIS runs. A detailed histogram is also produced for each module. To produce the summary of the histograms with details, a package based on *Athena* and named *TileMonitoring*, was developed.

2. **Automatic data quality checks.** An automatic system that verify the validity of the histogram content allows to check a large number of histograms. The input are the histograms produced during reconstruction and gives back data quality flags with results: *good*, *bad* or *to be investigated*. This system was developed using the Data Quality Monitoring Framework (DQMF), initially developed to check the results produced by online monitoring tasks.

3. **Histograms and DQ result presentation.** A database is used to easily access the plots and the data quality results. For each run, an entry is inserted with the list of all tested modules and the results from DQMF. This information is accessible by the Web Interfaces for Shifters (WIS) (figure 4.9). The DQ results are organized in a tree structure, containing the information corresponding to a functional aspect of the module: noise level, data integrity, timing or response to injected charge. Based on the status of the leaves, a DQ result is calculated for each group. In figure 4.10, the DQ result tree for one module is showed. *Green* color indicates that the status of the module is good, *yellow* means that there are some problems and *red* that something is wrong.

Run ☒	Run Type ☒	⊞ Run Date ☒	#events ☒	Setup ☒	Modules ☒ View Ntuples Status and detailed comments	Overview ☒ OK	Some Problems	Bad	Not to be Analized	Not Analized	# of Modules	Histogram ☒	Plots ☒	Shifter ☒
117181	Ped	30/05/2009 01:59:47	32000	LBA-LBC-EBA-EBC-sector-1-3-5-7-9-11-13-15		0%	0%	0%	0%	100%	256			
117180	Ped	30/05/2009 01:36:27	32000	LBA-LBC-EBA-EBC-sector-1-3-5-7-9-11-13-15		0%	0%	0%	0%	100%	256			
117179	Ped	30/05/2009 01:16:00	17945	LBA-LBC-EBA-EBC-sector-1-3-5-7-9-11-13-15		0%	0%	0%	0%	100%	256			
117178	Ped	30/05/2009 00:53:07	32000	LBA-LBC-EBA-EBC-sector-1-3-5-7-9-11-13-15		0%	0%	0%	0%	100%	256			
117177	Ped	30/05/2009 00:48:14	25	LBA-LBC-EBA-EBC-sector-1-3-5-7-9-11-13-15		0%	0%	0%	0%	100%	220			
117176	Ped	30/05/2009 00:23:18	32000	LBA-LBC-EBA-EBC-sector-1-3-5-7-9-11-13-15		0%	0%	0%	0%	100%	256			
116890	Las	28/05/2009 18:36:03	82004	LBA-LBC-EBA-EBC-sector-1-3-5-7-9-11-13-15		6%	8%	0%	0%	86%	256			Stanislav NEMECEK
116857	MonoCIS	28/05/2009 16:24:33	10010	LBA-LBC-EBA-EBC-sector-1-3-5-7-9-11-13-15		1%	0%	0%	0%	99%	256			Stanislav NEMECEK
116851	MonoCIS	28/05/2009 16:21:13	10007	LBA-LBC-EBA-EBC-sector-1-3-5-7-9-11-13-15		0%	0%	0%	0%	100%	256			
116754	Las	28/05/2009 10:17:23	10005	LBA-LBC-EBA-EBC-sector-1-3-5-7-9-11-13-15		0%	0%	0%	0%	100%	256			
116752	Las	28/05/2009 10:06:44	10014	LBA-LBC-EBA-EBC-sector-1-3-5-7-9-11-13-15		0%	0%	0%	0%	100%	256			
116748	Las	28/05/2009 09:52:07	368	LBA-LBC-EBA-EBC-sector-1-3-5-7-9-11-13-15		9%	3%	0%	0%	88%	256			Stanislav NEMECEK
116743	Ped	28/05/2009 09:40:25	10007	LBA-LBC-EBA-EBC-sector-1-3-5-7-9-11-13-15		0%	0%	0%	0%	100%	256			
116742	CIS	28/05/2009 09:35:53	4932	LBA-LBC-EBA-EBC-sector-1-3-5-7-9-11-13-15		0%	0%	0%	0%	100%	256			
116740	MonoCIS	28/05/2009 09:29:23	10011	LBA-LBC-EBA-EBC-sector-1-3-5-7-9-11-13-15		82%	16%	1%	1%	0%	256			Eva VALLADOLID GALLEGO
116697	Las	27/05/2009 18:18:22	85384	LBA-LBC-EBA-EBC-sector-1-3-5-7-9-11-13-15		0%	0%	0%	0%	100%	256			

Figure 4.9: Shot screens of the WIS. The status of the module is flagged with red/yellow/green colors.

Some samples from different calibration runs can be found in the Appendix A.
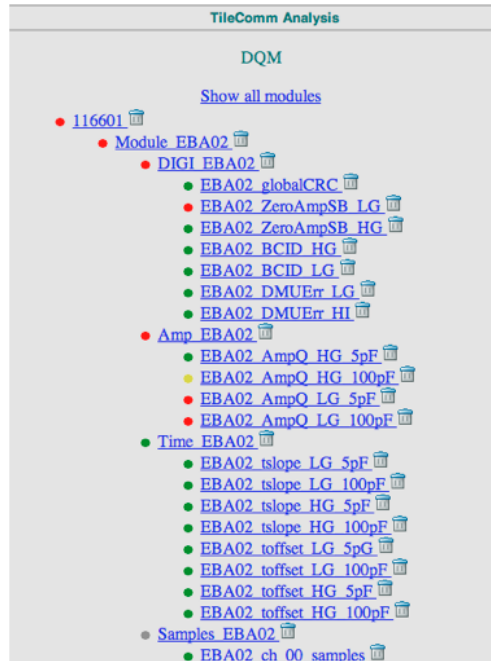
Figure 4.10: Tree organization with flag color for the status of EBA02 TileCal module.

4.3 Test Results Using Cosmic Data

In this section some test results obtained with the previously described tools are showed. Random and cosmic physics runs, as well as noise levels, number of events over a threshold, cluster reconstruction and muon reconstruction are evaluated through representative histograms. The analysis starts checking the runs taken by ATLAS and selecting the ones that have enough statistics with the WIS interface.

For a *Random Muon Stream* (RNMD), which is a random trigger, it is expected that no hot channels appear if everything is working well. Good results must show no events or strange values. Figure 4.11, shows a hot spot in the average noise representation for $\eta \sim 0.75$ and $\phi \sim 0.1$ (left). Checking a hardware oriented numbering representation (right), it is observed some activity in LBC 35 module. Figure 4.12 (left), shows how many events are over a threshold of 300 MeV. The value is sensible to the *tail* of the noise and not to the mean value. The module partition (right), is more useful to determine what is producing this *red* spot. Figure 4.13 shows the cluster reconstruction centered at zero, where no problems are observed.
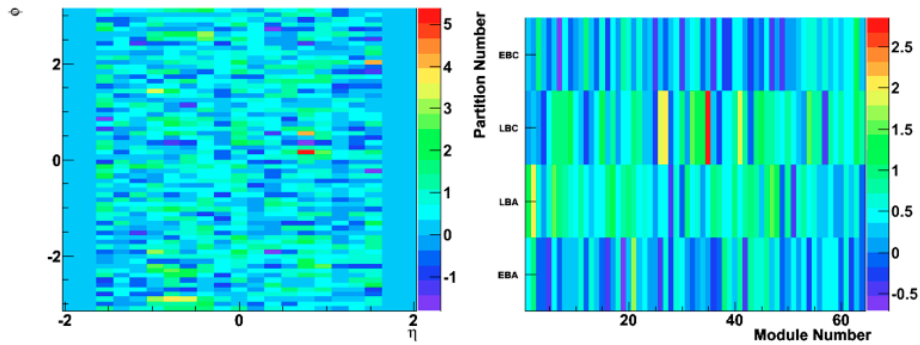
Figure 4.11: On the left, values of the average noise level as a function of η and ϕ. On the right, depending of the module number. A high rate in module LBC35 is observed.
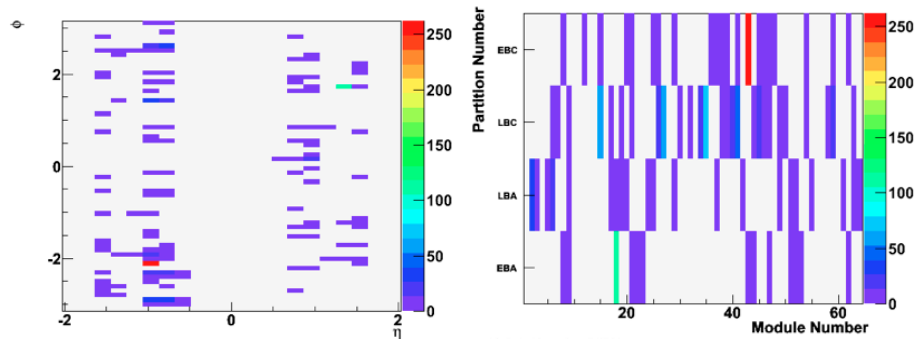
Figure 4.12: Number of events over a threshold of 300 MeV, depending on η-ϕ coordinates on the left, and on module partition on the right. It is observed high noise level in EBC 43 module.

Next figures show representative plots from the *Cosmic Muon* stream. Figure 4.14, where one can observe the muons crossing TileCal, displays the occupancy in η-ϕ coordinates, with a red mark detected. Figure 4.15(a), shows the reconstruction of muons crossing the detector, where it is represented the cosmic distribution data (black crosses) over the reference distribution, as a function of the detector coordinates. Figure 4.15(b) shows the maximum value of the entries, in perpendicular direction, which correspond with $sin(\theta = 90^o) = 1$. Figure 4.16, represents the distribution of the energy loss for the reconstructed muons. The muon energy loss shows a clear dE/dx peak close to 2 MeV/mm. Muons have a behavior of Minimum Ionizing Particles (MIP) showing an average energy and a
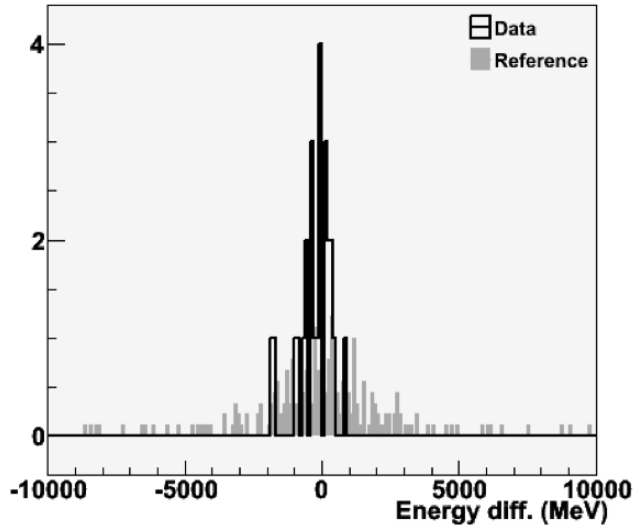
Figure 4.13: Cluster reconstruction centered at the zero.

characteristic wavelength.

As a conclusion of this section, we can say that the implementation of the TileCal monitoring system during the commissioning period helped to achieve the correct behavior of the detector, eventually becoming an indispensable tool. The TileCal front-end electronics data quality check performed by different steps, both *online* and *offline*, worked properly and allowed an efficient data taking and processing.

4.4 TileCal Muon Level-2 Trigger Studies

After the LHC incident in September 2008, the ATLAS experiment changed to a combined operating mode, taking data on cosmic rays that were used to calibrate the detector. Later, during the start-up phases of LHC operation, the overall performance of the ATLAS muon trigger system was studied with cosmic data, collected in autumn 2009. This section describes the three different muon trigger levels, and shows results from studies performed with TileMuID algorithm implemented at Level-2 (L2) Muon Trigger using this data and contributing to the commissioning of both: second level Muon Trigger and Tile Calorimeter system. The TileMuID algorithm, described in section 4.4.2, follows a strategy for tagging low p_T muons at L2 trigger in TileCal. The results presented in this work, which suffered of low statistic, take part of an ATLAS note [27], together with all muon
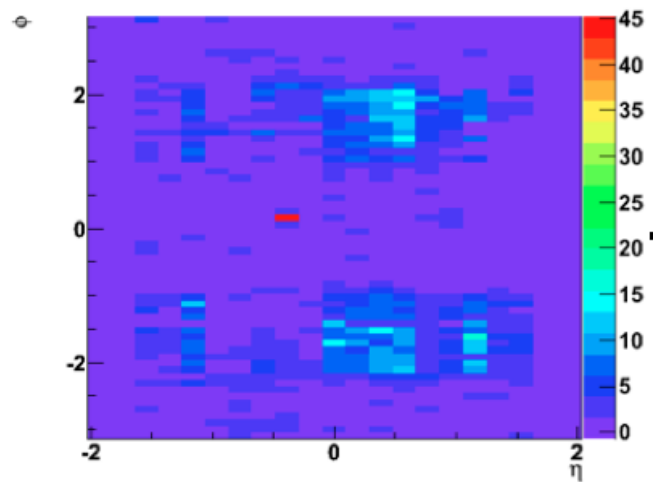
Figure 4.14: Occupancies as expected in η-ϕ coordinates, were a hot spot can be seen. One can observe the muons entering TileCal with the different shades of blue.

(a)

(b)
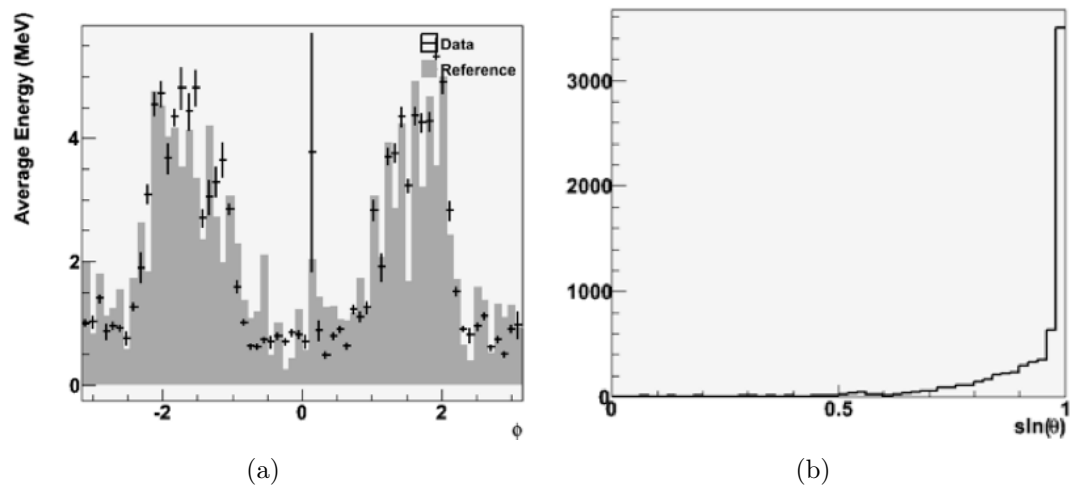
Figure 4.15: Typical appearance in the reconstruction of muons crossing the detector (left). Maximum level reached in perpendicular direction (right).
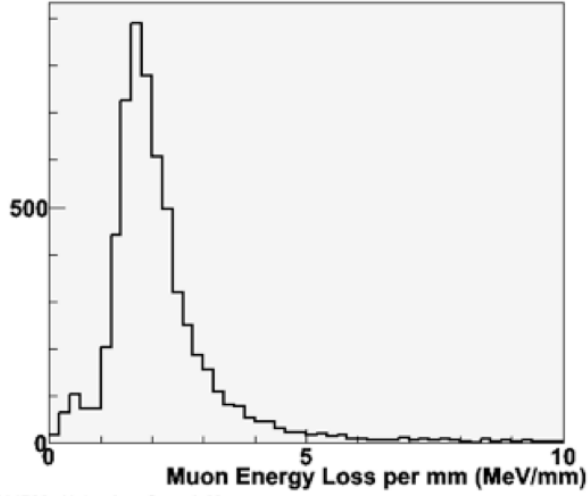
Figure 4.16: Muon Energy Loss reconstruction in TileCal. The distribution has the MIP characteristic peak around 2 MeV/mm.

trigger algorithms. The studies were performed at $\sqrt{s} = 900$ GeV.

4.4.1   Muon Trigger Overview

Muon candidates from collision events can be triggered with a L1 minimum bias trigger. Following some requirements made on ID tracks and timing information from the Minimum Bias Trigger Scintillator (MBTS) or the LAr end-caps calorimeter, it was possible to obtain selected muon candidates based on selected requesting cuts depending on the offline reconstruction. These muons were used to study the performance of the muon trigger at each level by looking at the ones passing the lowest L1 transverse momentum thresholds, and then processed and selected by the trigger algorithms of each level.

Similar to the ATLAS trigger general structure, the muon trigger system has three different levels: a hardware Level-1 (L1) and a software High Level Trigger (HLT), comprising Level-2 (L2) and the Event Filter (EF). The HLT starts from a *Region of Interest* (RoI), defined by the L1 trigger. The reconstruction uses extraction algorithms that request detector data associated with the RoI, to identify muons. The result of the reconstruction at the HLT level is passed through some hypothesis algorithms to determine whether an event is further processed or discarded. A set of cuts was applied on the p_T of the muon candidate to set

HLT thresholds. In this study, the effective thresholds were slightly lower than nominal ones, due that at the nominal value the efficiency was 90% of the corresponding one without cuts, meaning that the p_T cut applied on muon triggered with a determined chain, ought to be lower and dependent on the algorithm that imposes the cut and the resolution in the different components of the detector. That means for example, that the p_T cut applied on muon triggered with the $mu4$ chain is lower than 4 GeV and depends on the algorithm imposing the cut and on its expected resolution in the different parts of the detector. Finally, a decision that takes into account pre-scale and pass-through factors, allows to reject the event or to continue.

Figure 4.17 shows the diagrams of the general TDAQ and trigger systems with the designed values, explained as well in section 3.3.7.
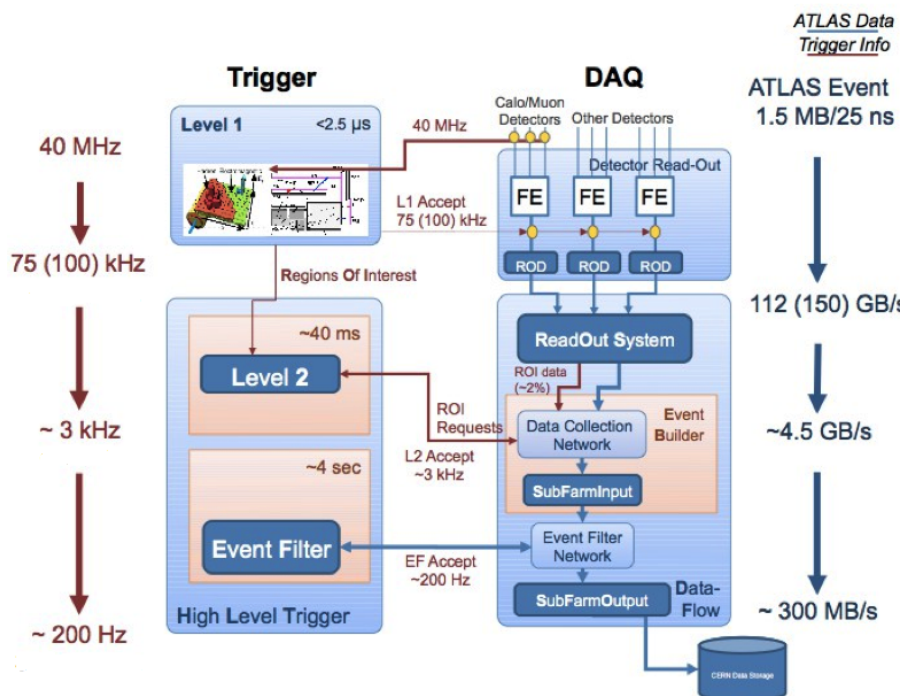
Figure 4.17: TDAQ and trigger diagrams at the designed values.

Muon Level-1 Trigger

The L1 muon trigger is designed to select muon events with high p_T. It allows the correct association to the Bunch Crossing (BC), using the Resistive Plate Chambers (RPC) in the barrel, which are located in the region $\mid \eta \mid < 1.05$, and

also the Thin Gap Chambers (TGC) in the end-caps, located in $1.05 <| \eta |< 2.4$. The electronic system rejects most of the background collisions in less than 2.5 μs, handling the information that comes mainly from the calorimeter and the muon detectors. The trigger algorithms search for hit coincidences within different RPC or TGC detector layers inside programmed geometrical windows. By this way, it is possible to define the muon p_T and to select muons above six programmable thresholds. They provide harsh estimation of the muon positions from coordinates η and ϕ. A special L1 configuration that increased the acceptance was set with the largest coincidence windows (L1_MU0), allowing the reconstruction of tracks not pointing to the interaction region. The number of L1 muon candidates for the six different thresholds was calculated by the Muon to Central Trigger Processor Interface (MuCTPI) [28], extracting the muon candidates information from the barrel and the endcap. Figure 4.18, represents a diagram of the L1 general trigger system. One can see there the Central Trigger Processor (CTP) with inputs coming from the calorimeters, muon spectrometer and additional signals. L1 level trigger receives LHC 40 MHz clock signals and distributes the decision and clock to sub-system front-end electronics and to HLT.
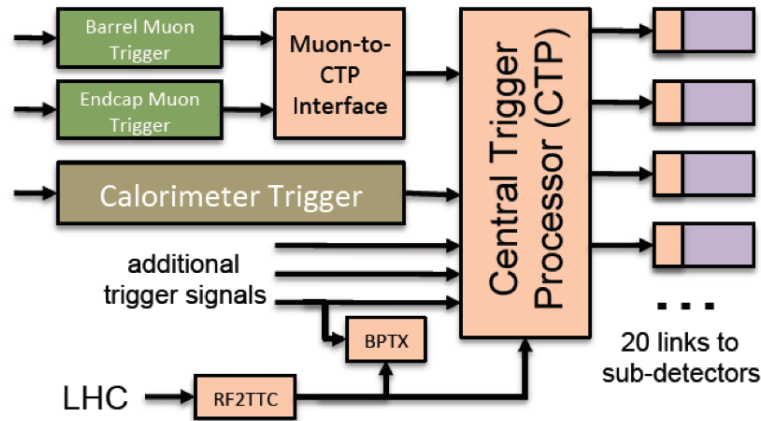
Figure 4.18: Diagram of the L1 trigger system.

Muon Level-2 Trigger

The second level muon trigger system is composed of different algorithms that use different strategies to study the muon candidates [29]. Together, they form the Muon Trigger Slice. The component algorithms and a brief description of them, are presented below:

- **TrigMuFast**: this L2 muon standalone algorithm is seeded by the RoIs defined by L1 and given by the RPCs and TGCs. It reconstructs the muon

tracks by the use of the Muon Spectrometer stand-alone information. There is a pattern recognition algorithm that selects hits from the Monitored Drift Tubes and the Muon Spectrometer stations, within a region defined by the L1 trigger. Then, a linear track fit is performed in each station to obtain the intersection of the muon trajectory with the station itself and its slope. At last, from these parameters, it is performed the p_T assignment via the look-up-tables (LUTs).

- **TrigMuComb**: this algorithm combines the reconstructed tracks in the ID, with the tracks coming from MS and found by the L2 muon standalone algorithm, TrigMuFast. The transverse momentum is calculated as a weighted average of ID and TrigMuFast transverse momenta. The algorithm improves the final momentum resolution, allowing the reduction of the trigger rates. It is used to improve the accuracy of the muon reconstruction at L2 level, as well as the pions and kaons rejection.

- **TrigMuIso**: this algorithm is used to discriminate between isolated and non-isolated muon candidates, this is feasible by checking energy deposits in the electromagnetic and hadron calorimeters and ID tracks, in the cone region of the muon candidate. It can be seeded by either TrigMuFast or TrigMuComb, and can be used to reject muons from beauty and charm semileptonic decays.

- **TrigMuTile**: also known as TileMuId. This algorithm, is described with more detail in section 4.4.2. It is seeded by the L1 RoIs provided by the RPCs and TGCs of the Muon Spectrometer. TileMuID identifies low-p_T projective muons in TileCal and can perform a matching with the ID tracks. It has been designed for the improvement of trigger in B-physics events.

Figure 4.19 shows a scheme of the ATLAS detector, pointing to the RoIs location defined by the pseudorapidity η and azimuthal angle ϕ coordinates.

Muon EF Trigger

The Muon EF trigger has access to the full event with full granularity. Two alternative algorithms, both part of the Muon Trigger Slice, are implemented. Both make use of the offline muon reconstruction algorithms to confirm or discard the candidates from L2. Their description is listed below:

- **TrigMuonEF**: this algorithm starts from tracks reconstructed in the Muon Spectrometer and extrapolate them back to the Interaction Point, refining the L2 hypotheses.
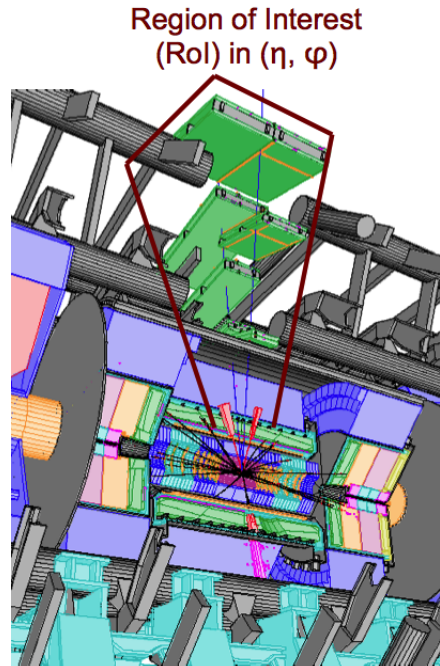
Figure 4.19: RoIs in η and ϕ coordinates in the ATLAS detector.

- **TrigMuGirl**: this algorithm reconstructs muon candidates in the Muon Spectrometer extrapolating the Inner Detector tracks, performing muon identification outward. It allows the selection of slow particle candidates.

Figure 4.20, shows a diagram of the Muon Trigger Slice, with the different algorithms presented inside the corresponding level. The full bandwidth and processing time are also indicated.

4.4.2   TileMuId algorithm

At L2 trigger level, TileCal has the possibility of tagging low p_T muons. The identification can be performed in p_T and η range, where the efficiency of the muon spectrometer is not so accurate. The algorithm integrated offline and at HLT, is named $TrigMuTile$ or $TileMuId$. It was mainly designed to improve trigger in B-physics events, where muons produce track segments only in the innermost layer of the MS, reaching RPC or TGC detectors with relatively poor probability. The algorithm also provides redundancy and robustness to the muon HLT and was used for commissioning, until the LHC startup period with collisions. It is based on the typical MIP-like energy deposition in the calorimeter and its geometrical segmentation.
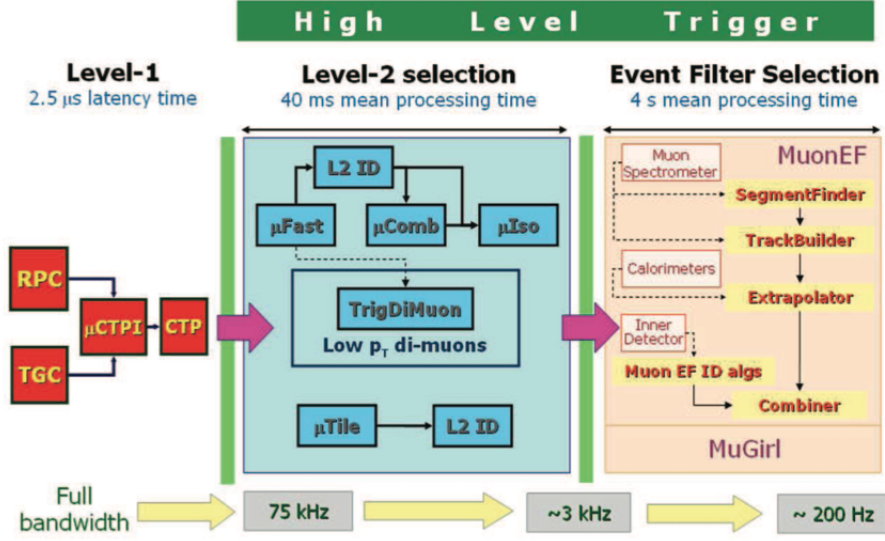
Figure 4.20: Muon Trigger Slice diagram.

TileCal is divided in three longitudinal samplings, named A, BC and D layers, and in η-projective towers, as it is showed in figure 4.21. The granularity in the outermost layer η x ϕ, is 0.2 x 0.1. Each cell in the D layer is associated to two different towers in the A and BC layers. The identification procedure starts by searching for muon candidates in the outermost TileCal layer, which contains the cleanest signals due to the screening effects of the inner layers against low energy hadrons and minimum bias pile-up. Then it is checked if the energy deposited in a D-layer cell is compatible with a MIP. In that case, a muon candidate is defined. To select whether a MIP-like deposition is found, the requirement of the cell energy (E_{cell}) to be comprised between a lower (Thr_{lower}) and a higher (Thr_{higher}) energy thresholds is applied, as indicated in equation 4.1.

$$Thr_{lower} < E_{cell} < Thr_{higher} \qquad (4.1)$$

The lower energy threshold discards noise fluctuations or minimum bias pile-up. The higher energy threshold is used to discard hadronic showers and tails. The search continues to the BC-layer cells in the two towers associated to the D-cell, the central and innermost layers according to projective patterns in η toward the IP, where the muon candidate is found. In case the conditions are also fulfilled in the BC layer, the corresponding A-layer cell is checked for a muon-like energy deposition. At each step, it is evaluated the compatibility of the cell energy with the energy expected to be deposited by a muon. Finally, if cells in the three layers are found in a projective pattern, whose energy depositions can be described by the

equation 4.1, the coordinates η and ϕ are estimated as the average of the crossed cells in the three layers, and the muon is tagged. In some cases the muon can go through the transition between the cells in the η direction and therefore leave signal in more than one tower. In consequence, a mechanism is implemented in TileMuId to prevent the same physical muon to be tagged twice in adjacent towers.
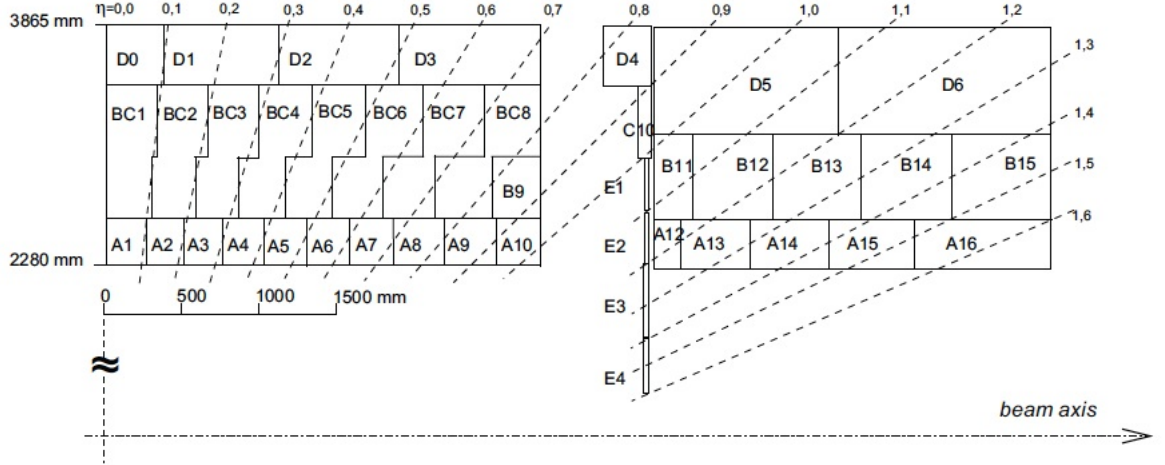
Figure 4.21: Logical segmentation of the TileCal modules as a function of η.

Two different strategies can be applied to identify muons: a full scan search in the TileCal, more independent of the MS trigger, but time-consuming, and a search in a specific region defined by the L1 muon RoI, which provides faster results but were a few percentage of events is lost. In order to reconstruct muons, two different criteria are defined: the *tight selection* or the *loose selection*. The first is the default condition of applying the same requirement of the condition given by equation 4.1 in the three TileCal layers. The second requires the energy in the three layers to be $E_{cell} > Thr_{lower}$, and the condition $E_{cell} < Thr_{higher}$ is only imposed in two of the three cells. In this way, it is possible to recover muons which deposit a large amount of energy in a small volume.

Versions of the TileMuId algorithm

The TileMuId, seeded by L1 muon RoIs provided by the RPCs and TGCs, was implemented in different versions. The component algorithms that run at the L2 trigger, are the following:

- **TrigTileLookForMuAlg:** it was fully implemented in the *Athena* framework. This algorithm came into *AllTEAlgo* [31] base class, accessing the TileCell objects around the L1 RoIs, where the TileMuId algorithm was applied. The output of TrigTileLookForMuAlg contained the information from the muons tagged.

- **TrigTileRODMuAlg:** it was a ROD-based implementation. TileMuId was also inside the ROD DSPs processors. This algorithm inherit as well from *AllTEAlgo* base class and it was executed for all the events taken by L1 trigger. It access the ROB fragments around L1, taking the TileMuId information computed at the ROD level, and encodes the results in the output data format in a dedicated fragment. An specific software in the L2 trigger, recovers the information to be used in the HLT environment [32].

- **TrigTileMuFex:** TileCal muon candidates can be also combined with the Inner Detector tracks. The ID uses *TrigIDSCAN* by default. Monitoring histograms are available to check the algorithm performance [33]. This implementation comes from *FexAlgo* base class [31]. It combines the TileCal information given by TrigTileLookForMuAlg or TrigTileRODMuAlg with the ID tracks. The tracks, provided by ID trigger algorithms, are extrapolated from the ID to the TileCal radius, and then stored.

In this work, the TileMuId algorithm applied is TrigTileLookForMuAlg. Section 4.6 shows the results of the study performed using cosmic data, intended for commissioning of the Muon HLT and TileCal.

4.5   Cosmic data samples

During the 2009 data taking and until the final HLT commissioning, the HLT was running online, based on the L1 RoIs but without selecting or rejecting events actively. The L1 RoI content was examined and the events were directed into the different recording streams. This procedure allowed the performance of the HLT algorithms to be studied later in the collision events. Cosmic and collision data where collected during the startup phases of the LHC for muon trigger commissioning. The TileMuID algorithm implemented at L2 ran with cosmic data and only the runs flagged globally as good by Data Quality Assessment procedure, were considered.

The ATLAS detector is mainly reached by cosmic rays via the two big pits and with incident angles close to the vertical. Those particles are expected to be triggered in the MS mostly by the RPC chambers. During data taking, special trigger configurations were used, in order to improve triggering on particles non

pointing to the IP. The analysis presented in this work have been performed by using subsets of cosmic data, corresponding in total to few millions of events, acquired during the run periods in Fall 2009. The analyzed events, were selected unbiased as triggered by the ID. The L1 muon trigger, selected tracks with six different p_T inclusive thresholds (three low-p_T and three high-p_T) and sent the information to the CTP. Five of the six thresholds did not discern between end-caps or barrel, while the remaining one was aimed to RPC commissioning. IP-pointing constraint was applied in the definition of the higher p_T thresholds, both in η and ϕ projections. These L1 items seeded the different muon chains built in HLT, allowed for a full commissioning and monitoring of all L2 and EF algorithms.

4.6   Results from TileMuId Studies

This section shows the results from TileMuId tests, under the conditions described in section 4.5, running $TileLookForMu$ algorithm with Athena release 15.5.5.5, which uses mu_4tile chain. A low threshold of 300 MeV has been applied for all the cells.

4.6.1   TileMuId Performance with respect L1

Figure 4.22 represents the correlation for the ϕ coordinate between the Level-1 muon RoIs and the muons tagged by TileMuId algorithm, with a granularity of $\sim$0.01 rad and before combining with the tracks in the ID. The data are cosmic ray muons triggered by L2. The distribution shows a good correlation, although the efficiency of the muon tagged is affected in the lower part of the detector.

4.6.2   TileMuId Stand-alone Performance

Figure 4.23 (left) shows the azimuthal angle distribution in TileCal obtained with the L2 TileMuId algorithm. There, it is observed the typical up-down shape, as to be expected for cosmic muons passing through the calorimeter. The distribution shows an asymmetry due to the fact that more muons are identified at the top of the barrel than at the bottom. The reason for this asymmetry could be due not only to the lack of statistic, but to the fact that the Muon Spectrometer gives bigger L1 RoI values at the top (since cosmic come from top to bottom), and the RoIs are sent to L2 by L1 barrel muon chamber. Figure 4.23 (right) shows the ϕ distribution obtained from online monitoring. The same asymmetry is observed between negative and positive ϕ. Another hypothesis of this asymmetry, could be because low p_T muons, certainly do not satisfy the trigger requirements after passing the calorimeter. Usually more events should be found in the ϕ coordinate
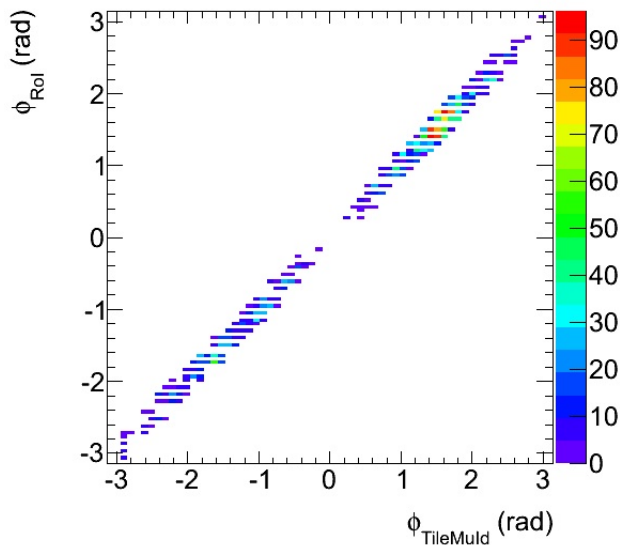
Figure 4.22: Correlation between the ϕ coordinate of the Level-1 muon RoIs and the muons tagged by TileMuId.

corresponding to the up-down direction, as expected for the cosmic ray dependence on $\cos\theta$ [34]. Figure 4.24 shows the TileCal η distribution, more symmetrical as it is expected. In the picture one can observe the structure for the central barrel and the extended barrels. The shape shows a slight discrepancy with the expected one [33], due to noise dependency with η. This led to the usage of a database to store the lower energy thresholds for further use with real data, allowing the definition of different lower energy thresholds for each cell, depending of the noise level.

Finally, figure 4.25 shows the energy deposited in the TileCal by cosmic muons triggered by TileMuId. The distribution shows a tail, due to cosmic muons that deposit a large amount of their energy in a single cell. As mentioned before, a cut on minimal cell energy > 300 MeV was applied to take into account and reduce the effects of the electronic noise. A peak in the energy deposited is observed around 2 GeV, compatible with the behavior of minimum ionizing particles in TileCal, and consistently to what can be observed on MC simulations [33].

Even though the cosmic rays topology is not the optimal for muon identification with TileMuId, as the algorithm was designed to tag muons from collision data, the performance of the algorithm at the L2 muon trigger with cosmic data was useful for the commissioning of the detector. The low p_T muon chains running TileMuId defined in the muon L2 trigger menu, provided an alternative method
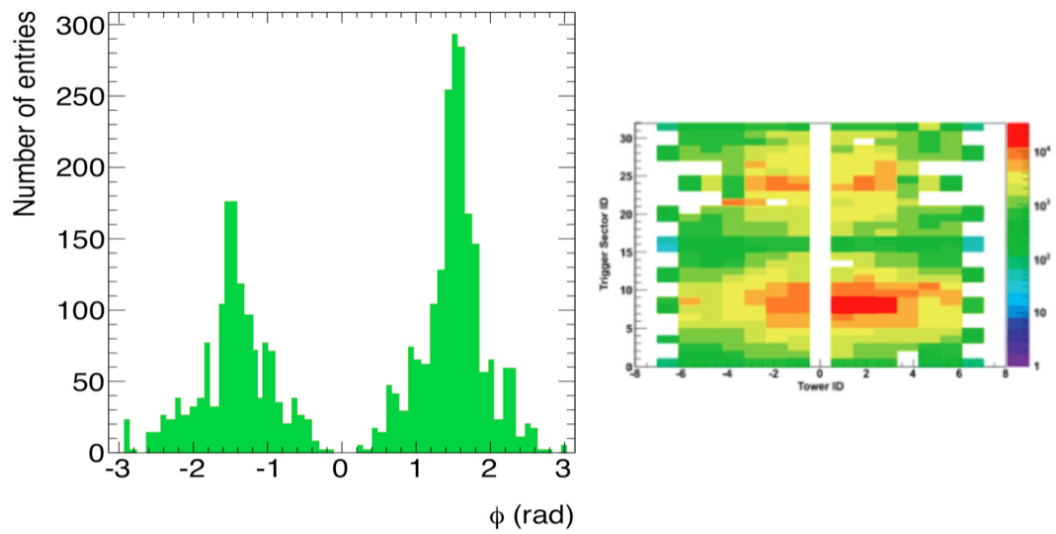
Figure 4.23: On the left, ϕ distribution in TileCal for cosmic ray muons triggered by L2. An asymmetry is observed in the lower part of the detector. On the right, same distribution obtained from online monitoring.
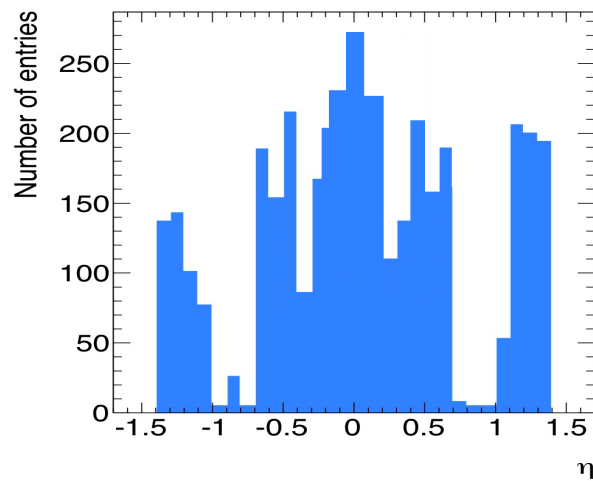
Figure 4.24: η distribution of cosmic rays in TileCal.
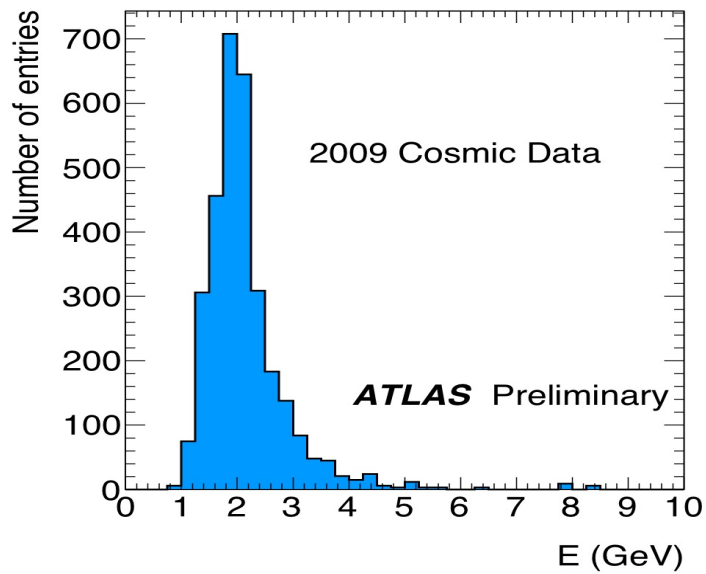
Figure 4.25: Energy distribution in TileCal for cosmic ray muons triggered by L2. Data were collected in autumn 2009.

to check the MS standalone trigger. The chains were seeded by muon L1 RoIs. The information from TileMuId was used to confirm the muon spectrometer L2 trigger robustness, given redundancy in noisy/dead regions and in full scan search mode, to enhance the selection efficiency for very soft muons not reaching the spectrometer.

Chapter 5

$t\bar{t}$ Studies with τ in the Final State

This chapter contains a measurement of the top quark ($t\bar{t}$) production cross section ($\sigma_{t\bar{t}}$) with a lepton, electron or muon, and a hadronically decaying τ-lepton in the final state, using 4.73 fb^{-1} *proton-proton* collision data at a center of mass energy $\sqrt{7}$ TeV, performed in the framework of the ATLAS experiment. The final states with a lepton and a hadronically decaying τ-lepton are represented as $t\bar{t} \rightarrow W(\rightarrow \tau_{had}\nu_\tau)W(\rightarrow l\nu_l)b\bar{b}$ and $t\bar{t} \rightarrow W(\rightarrow \tau_{had}\nu_\tau)W(\rightarrow \tau(\rightarrow l\nu_l\nu_\tau)\nu_\tau)b\bar{b}$, where l denotes an electron or a muon, and τ_{had} denotes the hadronically decaying τ-lepton. Figure 5.1 shows the diagram for $t\bar{t}$ production from gluon-gluon fusion, the dominant production mechanism at the LHC, in which one W decays to a tau and a neutrino and the other W decays to an electron or muon and a neutrino. A main ingredient of this analysis is the reconstruction and identification of hadronically decaying τ leptons. Therefore an exhaustive study of the mis-identification probabilities of τ in the γ + jets channel (τ fake rates), is performed before measuring the $t\bar{t}$ cross-section, in order to control de quality of the tau reconstruction and identification included in the sample of 4.73 fb^{-1}. Also the calculation of the corrections for the Z simulation samples within this analysis (scale factors) to bring the MC into closer agreement, is included.

The outline of the chapter is performed as follow:

1. The common object definition of the whole analysis is showed in section 5.1. In subsection 5.1.6, it is showed the τ fake rates estimation study, a complementary study to the tau identification. This analysis calculates the probabilities of τ mis-identification using BDT (Booster Decision Tree) and LLH (LikeLiHood) τ-identification algorithms, as well as the number of vertices versus its p_T. The Data and MC samples description is displayed in section 5.2.

2. The Z scale factors values for 4.73 fb^{-1} are calculated in section 5.3. It is

73

completed with studies of the dependency of the scale factors with η and BDT_j shape, showed in appendix B.

3. The selection of events to extract the $t\bar{t}$ events, is displayed in section 5.4. Candidate events are extracted by requiring a lepton, e or μ, in the final state of the τ hadronic decay. It is required to have more than two jets, where at least one of them being identified as originated from b-$quark$, as well as a large missing transverse energy (E_T^{miss}). The application of the kinematic selection criteria and the b-tagging left as dominant background $t\bar{t} \rightarrow l + jet$, in which the jet fakes a hadronic tau decay. The most powerful discriminator between signal and the remaining background is tau identification, which is considered in the rest of the analysis. After these descriptions, the results with control tables and plots of the events that passed the selection, are displayed in section 5.5.

4. The background method for cross-section estimation based on fitting differentiated background templates for gluon/quark jets faking τ leptons is showed in section 5.6. The method has been developed to extract the signals at 2 fb^{-1} [64] and it is applied to the whole dataset collected by the AT-LAS detector in 2011 aiming to improve the precision of the measurement published with 2 fb^{-1} [65], as well as the background model originated by jets falsifying hadronically decaying tau leptons. This work shows the application to samples at 4.73 fb^{-1}. It is based on fits to Boosted Decision Tree (BDT) output distribution to extract the number of $t\bar{t}$ events using a differentiated set of BDT background templates obtained from control data samples dominated by $W + jet$ events. The signal is selected by fitting the BDT output distribution with three templates: a quark rich background template, a gluon background template and a signal template derived from MC events from processes with a τ-lepton, applied in section 5.7. The background model is also improved by reducing the statistical uncertainty.

5. An evaluation of the relevant systematics is performed in section 5.8, to finally obtain a measurement of the t-quark pair production cross section, showed in section 5.9. The cross-section ($\sigma_{t\bar{t}}$) is calculated as,

$$\sigma_{t\bar{t}(Measured)} = \frac{S_{(\mathrm{Measured})}}{S_{(\mathrm{Expected})}} \cdot \sigma_{t\bar{t}(Theoretical)} \tag{5.1}$$

where $S_{(\mathrm{Measured})}$ is the measured signal, $S_{(\mathrm{Expected})}$ is the expected signal, and $\sigma_{t\bar{t}(Theoretical)}$ the theoretical cross section, which is taken as 177.3 pb (for top quark mass of 172.5 GeV) [66,67].
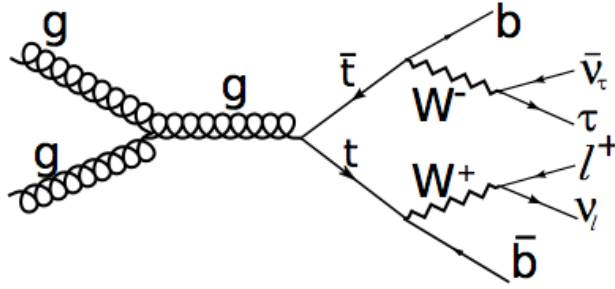
Figure 5.1: Diagram of the $t\bar{t}$ production from gluon-gluon fusion in the final state. One W decays to a lepton (electron or muon) and a neutrino, and the other W decays into a tau and a neutrino.

5.1   Common Object Selection

To identify the physical processes as $E_T{}^{miss}$, leptons or jets, it is necessary the object definition starting from reconstructed objects, as explained in section 3.4. It is used all the standard reconstructed object definitions and corrections as recommended by the Top Reconstruction Group [47]. Below, it is showed the selection criteria for physical objects with additional criteria used in this analysis, with some details on the reconstruction and identification.

5.1.1   Electrons

Isolated electron candidates are required to pass a 'tight' criteria, which includes cuts on calorimeter, tracking and combined variables to separate isolated electrons from jets. Electrons must be into the region $|\eta_{cluster}| < 2.47$, where the pseudorapidity of the calorimeter energy cluster is associated to the electron. They have a transverse energy, $E_T > 25$ GeV. The electrons must also pass an E_T isolation cut in a cone of $\Delta R = 0.2$ derived for 90% efficiency along with a p_T isolation cut in a cone of $\Delta R = 0.3$ derived for the same efficiency. The electrons must have a longitudinal impact parameter z_0 with respect to the primary vertex < 2 mm. At last, if the electron overlaps with a good muon, is removed from the event if it rest within a cone of $\Delta R = 0.4$ of the muon. Data recommendations are taken from [48].

5.1.2   Muons

Muons candidates are reconstructed using the MUID algorithm to match tracks from the Inner Detector with tracks in the Muon Spectrometer. They are required to have $p_T > 20$ GeV and $|\eta| < 2.5$ GeV, passing the 'tight' criteria designed to reduce muon misidentification and isolation cuts: the calorimetry energy, in a cone of radius $\Delta R = 0.2$ around the muon track, < 4 GeV and the sum of the p_T of the tracks, reconstructed in the inner tracker in a cone $\Delta R = 0.3$ around the muon track, < 2.5 GeV. The ID track associated to each muon is required to have at least one Pixel hit or have crossed one dead pixel sensor, the sum of the number of SCT hits and number of crossed dead SCT sensors must be > 5, the number of SCT holes plus the number of pixel holes must not be greater than 3 and there must be a B-Layer hit if it is expected. If the muon overlaps with a good electron, but considering good electrons down to $E_T = 20$ GeV, it is removed from the event if it lies within a cone of $\Delta R = 0.4$ of the electron. If the muon overlaps with a good jet, as defined following this, it is removed from the event if it lies within a cone of $\Delta R = 0.4$ of the jet.

5.1.3   Jets

Jets are reconstructed with the *anti-k_t* algorithm [49], with a distance parameter of R = 0.4. Jet candidates are required to have $p_T > 25$ GeV and $|\eta| < 2.5$ [48] and with a jet vertex fraction (JVF) > 0.75. Any jet close to any good electron, is removed from the event if it lies within a cone of $\Delta R = 0.4$ of the electron.

5.1.4   *b*-jets

The *t*-quark produces one *b*-quark in the decay, which means that $t\bar{t}$ events contain at least two *b*-quarks. They are reconstructed in the calorimeter as jets and tagged as b-jets. In this analysis at least one *b*-jets is required, what reduces drastically the W+jets background. It is also applied the algorithm MV1, which allows to tag the jets originated from *b*-quarks, using a multivariate discriminant that exploits the long lifetime, high mass and high decay multiplicities of *b*-hadrons. If the MV1 discriminant value is greater than 0.6017, a jet is considered *b*-tagged, which corresponds to an average efficiency of 70% [48,50].

5.1.5   Missing transverse energy

In the case of leptonic decays, there are two sources of E_T^{miss} that make difficult to reconstruct the transverse masses of the two W bosons. The E_T^{miss}, is reconstructed from the vector sum of all calorimeter cells with $|\eta| < 4.5$, projected onto

the transverse plane and operated for other objects in the event. This quantity is used as the signature of undetected neutrino. The energy values of cells associated with jets are corrected using the jet energy scale and the τ's are treated as jets. To compute the contribution from cells associated with electrons, the electron energy calibration is taken into account. There are included also the contributions from muons passing the selection requirements, but are removed those corresponding to cells associated with the muon [48].

5.1.6 τ identification

The $t\bar{t}$ events have a large jet multiplicity. For this reason, it is very important to have a good identification of the real τ's of the event and give high jet rejection. The τ decay can be hadronic in a 65% of the cases, or leptonic, in the remaining 35%. Only the hadronic one is used for the reconstruction, due that the leptonic decaying τ is not distinguishable to that of primary leptons from the interaction point. In this analysis, the τ candidates are reconstructed using calorimeter jets performed with the *anti-k_t* algorithm. These seed jets are calibrated with the Local Calibration (LC) scheme. The τ energy, based on the calorimeter cluster energy, is reconstructed using the default energy scale by *tauRec* [52] in release 17. Tracks with $p_T > 1$ GeV and passing some minimum quality criteria are then associated to the τ candidates. The τ candidate must have $|\eta_\tau| < 2.3$, $p_T^\tau > 20$ GeV, $0 < N_{\text{trk}} < 4$, and the leading τ track must have $p_T > 4$ GeV [48]. Also a muon veto is required to reduce the muon background. The τ candidates with one associated track are named 1-*prong* candidates (τ_1), and those with more than one associated track are the τ_3 candidates (multi-*prong*). The candidates that overlap with 'loose' muons and electron whitin $\Delta R(\ell, \tau) < 0.4$ and the ones that overlap with b-tagged jets ($\Delta R(b\text{-jet}, \tau) < 0.4$), are removed. A cut based on a *medium* Boosted Decision Tree (BDT_e) is applied as electron veto, to remove electrons identified as τ candidates that have not been identified as an electron candidate. The BDT variable, of great importance in this analysis, will be explained bellow in this section. The *medium* working point corresponds to 85% efficiency for $Z \to \tau\tau$ [52]. The additional rejection for electrons after removing isolated electrons that overlap with τ candidates is a factor of 60. Some of the refined variables used for τ identification are:

- Track radius (R_{track}): the p_T weighted track radius measured from the τ candidate axis.

- Core energy fraction (f_{cor}): the fraction of transverse energy in the core within $\Delta R < 0.1$ of the tau candidate.

- Electromagnetic radius (R_{EM}): the transverse energy weighted average in the electromagnetic and hadron calorimeter, measured from the τ candidate axis. Only cells in the EM calorimeter with $\Delta R < 0.4$, are used:

$$\Delta R = \sqrt{(\Delta\eta)^2 + (\Delta\phi)^2} \tag{5.2}$$

- Cluster mass ($m_{\text{eff. clusters}}$): the invariant mass calculated from the constituent clusters of the jet seed.

- Track Mass (m_{track}): invariant mass computed from the constituent tracks of the τ candidate.

- Leading track momentum fraction (f_{track}): the transverse momentum of the leading p_T track within $\Delta R < 0.2$ from τ jet axis, compared to the transverse momentum of the τ candidate.

- Number of isolation tracks ($N_{\text{track}}^{\text{iso}}$): Number of tracks having the isolation within $0.2 < \Delta R(\tau \text{ jet, track}) < 0.4$.

After τ reconstruction, ATLAS uses mainly two different techniques to separate τ from jets: Likelihood (LLH) and Booster Decision Trees (BDT) algorithms, apart from other simple cuts.

- **LLH** identification: the likelihood function is defined as the product of the identification variables distributions:

$$L_{\text{S(Bkg)}} = \prod_{i=1}^{N} p_i^{S(Bkg)}(x_i) \tag{5.3}$$

being $S(Bkg)$ referred to signal (background), and $p_i^{S(Bkg)}$ is the signal probability density function of variable x_i. The likelihood function leaves correlations between variables and indicates the joint probability distribution for the input variables. From the log-likelihood ratio between signal and background, is built a discriminant defined as:

$$d = ln(\frac{L_S}{L_{Bkg}}) = \sum_{i=1}^{N} ln(\frac{p_i^{S}(x_i)}{p_i^{Bkg}(x_i)}) \tag{5.4}$$

- **BDT** identification: This analysis uses the BDT for τ identification [53]. This variable allows to discriminate τ jet against electron, quark and gluon originated jets. The BDT uses simple cut-based analysis into the multivariate

algorithm with a continuous discriminant output that goes from 0 to 1. During training, a decision tree selects the variable and cut value which gives the most separation between signal and background (in this case, τ's and jets). Events that fail a particular cut in the decision tree, are not discarded and continue being considered by the algorithm. In this way, an individual variable can be reused many times. Selecting successively the best available variable, a simple decision tree makes continuos cuts through the space defined in the input variable. The 'boosting' process create a second decision tree optimized to apply to the candidates that were misclassified by the first tree. A large number of trees can be created. At the end of the process, the final BDT consists on the weighted average over many trees. The calculated bookmark of a single candidate, is close to 1.0 if it is closer to be the signal, and 0.0 if is more likely the background. Also the Boosted Decision Tree τ-jet discriminant (BDT_j), which rejects hadronic jets faking τ leptons is used in this study. This variable has been tested in [52], using $Z \to \tau\tau$ MC as signal and dijet data.

Following this, an study of the mis-identification probability of τ leptons from hadronic jets is performed, using 2011 data samples with a view to validate the BDT method for tau identification, one of the main ingredients in this work.

τ ID studies: Fake Rates Estimation from $\gamma + jets$ Samples

The fake rate or mis-identification probability, is an interesting aspect on $t\bar{t}$ cross-section analysis, where the τ_{ID} is not equally performant against all type of jets. In the next, the fake rate of τ leptons from hadronic jets is evaluated with a $\gamma + jets$ selection, corresponding to 2011 data-taking periods with an integrated luminosity of ~34 pb^{-1}. This samples have a high amount of jets coming from light quarks. They are studied applying different methods for tau identification, using BDT and LLH algorithms, in order to validate the best for 2011 data.

Different quality requirements are chosen: *loose*, *medium* and *tight* selections corresponding to different τ identification efficiency working points ($\sim60\%,\sim45\%$, $\sim30\%$, respectively of signal efficiency). The obtained results, are compatible with the ones obtained with 2010 samples [62] using another version of the reconstruction, which validate the use of the BDT algorithm for tau identification with 2011 data samples, applied in the main analysis of this work.

τ Fake Rate Definition

The τ fake rate is defined as the number of jets passing the τ_{ID} (or identifies τ's), divided by the number of jets (or τ's candidates):

$$f_{ID} = \frac{\text{Number of probe jets identified as } \tau \text{ leptons}}{\text{Number of probe jets reconstructed as } \tau \text{ leptons}} \qquad (5.5)$$

The mis-identification probability of τ leptons from hadronic jets, can be determined from topologies where a jet is balanced in p_T and ϕ by a γ. Compared with the di-jet and three-jet topology where the fraction of quark jets is about 50% integrated over p_T, for the $\gamma + jet$ channel, the fraction is increased to about 90% [62]. The efficiency of the fake rate depends on the event selection, the p_T distribution of the τ candidates considered, and the type of the parton that initiates the jets.

τ Identification Criteria

Two identification criteria for τ, have been applied. The ATLAS τ identification, depends on multivariate techniques that separate the signal from the quark and gluon jet backgrounds. The use of these different variables, which are combined into multi-variate methods, increase the discrimination power [61]. Both variables, LLH, which apply the likelihood ratio formed using signal (MC) and background probability distribution functions, and BDT, which uses information from multiple decision trees to form a weighted score for signal and background hypotheses, were previously described.

The analysis of these identification variables is complemented with the study of the dependence with the number of primary vertices found in the event on the mis-identification probability.

Preselection and Event Selection for fake rate estimation

The event selection starts with the inclusion of the official Good Run List (GRL) [56] for τ's, followed by the corrections from Liquid Argon calorimeter. Then, an event cleaning is performed requiring at least one vertex with 4 traces. After this, it is applied at least one of the event-filter level triggers with transverse energy (E_T) thresholds of the γ at 20, 40 and 60 GeV, including loose photon identification, in order to select the $\gamma + jet$ topology. The preselection of the events also includes tight isolation requirements. A leakage correction that rejects γ's that have more than 6 GeV of energy outside the isolation region, has been added. In a next step, no bad jet is required with $p_T < 20$ GeV and energy < 0. This is followed by the requirement of at least one good jet and at least one good γ. The next condition demands the $D\phi$ angle between leading good photon and leading good

jet > 2.94. The measure of the distance between the τ candidate and the leading jet, must be lower than 0.2. Finally it is required the p_T of the sub-leading good jet be lower than 10% of the leading good photon p_T. The electron selection follows recommendations from Top Reconstruction group [57]. The developed analysis code is available at the Subversion code management system in ATLAS (SVN) [58]. The event selection for γ, $jets$ and τ, are listed as follows:

- one *tight* γ candidate in the event is required with a $p_T > 15$ GeV and pseudo-rapidity $\eta < 2.5$. The selection follows the recommendations from Standard Model Direct Photon analysis [59], checking for bad clusters and leakage corrections,

- the jet in the event is selected requiring to have $\eta < 2.5$, with $p_T > 20$ GeV and positive energy. Also the $AntiKt4TopoEM$ jet algorithm [60] is applied,

- the preselected τ is required with $p_T > 15$ GeV, $\eta < 2.3$, number of tracks $N_{tracks} < 4$, and positive charge.

Results on Event Selection and Identification Criteria

The analysis starts with the search of the leading jet, followed by the selection of the leading γ. Then, it is checked if the leading γ and the leading jet are back-to-back, in that case the nearest τ candidate to the jet with distance less than 0.2 is considered. An overlap removal is performed between τ-jet probe and electrons, that rejects most of the identified electrons after photon trigger requirement. Table 5.1 shows the cut-flow, with the number of events for the different cuts and the efficiency of the calculated events. Some plots have been performed to control the effect of the different cuts. Figure 5.2(a), shows the angle between leading photon and leading jet, where the cut in $D\phi(\gamma - Jet) > 2.94$, is indicated. Figure 5.2(b) represents the nearest τ candidate to jet with distance lower than 0.2.

Histograms showing results of the fake rate evaluation as a function of τ lepton p_T, performed with BDT and LLH selections and as a function of the number of vertices, are displayed in the following.

Fake Rate results with BDT versus τ_{p_T}

Figures 5.3(a) and 5.3(b), for 1-*prong* and 3-*prong* cases, show the fake rate as a function of τ-lepton p_T, for BDT *medium*, *loose* and *tight* variables. The fake rate values should be as lower as possible, by definition. In these results, the limits are very close to the expected ones, being the case of the low p_T, slightly higher to the values used as reference in the study with tight selection [62], but close to the

Table 5.1: Cutflow table with fake rate efficiency estimation from $\gamma + jets$ samples.

	$\gamma + Jets$ (N. of events)	$Fake\ Rate\ Efficiency$
GRL	51568255	
$Event\ Cleaning$	51562991	99.99 ± 0.00
$Trigger$	5366034	10.41 ± 0.00
$No\ Bad\ Jet$	5331779	99.36 ± 0.00
$At\ Least\ 1\ Good\ JET$	5231181	98.11 ± 0.01
$At\ Least\ 1\ Good\ \gamma$	802019	15.33 ± 0.02
$D\phi(\gamma - Jet) > 2.94$	348149	43.41 ± 0.06
$DR_{min}\ (\tau - jet) < 0.2$	71917	20.66 ± 0.07
$p_T(Jet_{subl.}) < 10\%$ of the $p_T(\gamma_{lead.})$	44438	61.79 ± 0.18

(a)   (b)
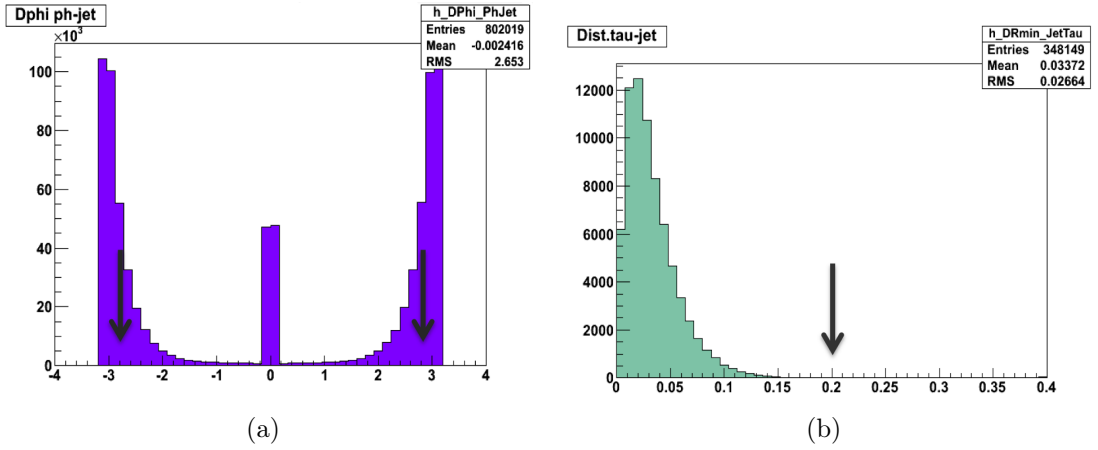
Figure 5.2: Figure (a) represents $D\phi$ angle between leading γ and leading jet. The arrows indicate where the cuts have been performed. Figure (b) represents the τ-jet distance(below 0.2).
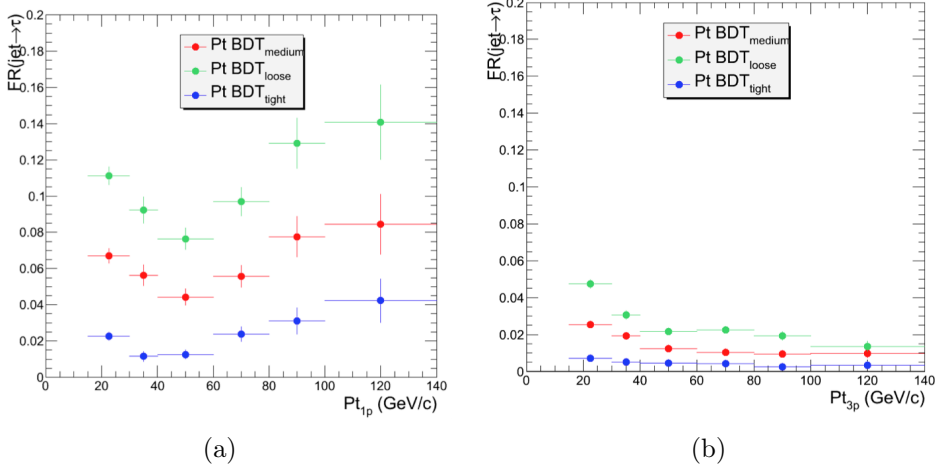
Figure 5.3: Fake rates versus p_T for τ-BDT *medium*, *loose* and *tight* variables. (a) for 1-*prong* and (b) for 3-*prong* configurations.

expected ones. Results for 1-*prong* case are ranged from 0.01% to 0.15%, being the *tight* selection between 0.02 and 0.04 the most accurate. For 3-*prong* case, the probability are between 0.005% and 0.05%. Figure 5.4 shows the mis-identification probability, as a function of τ-BDT lepton versus η and ϕ angles. It is expected to be closer to a flat distribution. The obtained results are in good agreement with the expected values.

Fake Rate results with LLH versus τ_{p_T}

Next results show the mis-identification probability as a function of τ-lepton p_T, for τ LLH *medium*, *loose* and *tight* selections. In this case, the results are higher when compared with BDT selections. The reason could be that not include the electron veto based on BDTe may influence the results. In figures 5.5(a) and 5.5(b), the fake rates for τ-LLH versus the p_T are showed. The obtained values range from 0.02% to 0.25% for 1-*prong* case, and from 0.005% to 0.16%, for 3-*prong* case. Figure 5.6 shows the results versus η and ϕ angles in a similar representation than in the BDT case.

Fake Rate results with BDT_{medium} versus $N_{vertices}$

Next figures show the effect of the number of primary vertices found in the event on the mis-identification probability as a function of τ-lepton p_T for the $\gamma+jets$ topology. Figures 5.7(a) and 5.7(b), show fake rates versus the number of primary vertices with BDT_{Medium} variable. The number of different primary vertices studied must be lower than 2, 4, 6, 8 and 12 in the different cases. These distributions
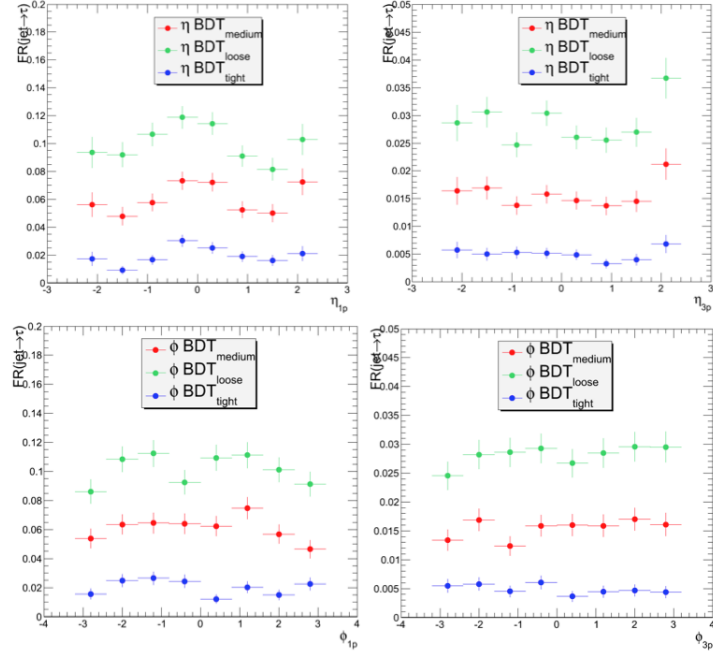
Figure 5.4: Fake rates for τ BDT selection. On the top the fake rate as a function of η for 1-prong on the left, and 3-prong on the right. On the bottom, similar representation for ϕ case.
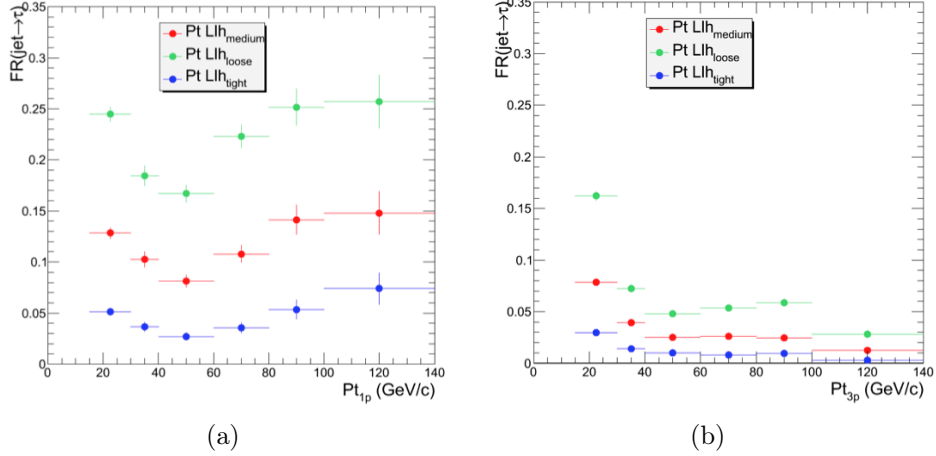
Figure 5.5: Fakes rates in p_T for τ-LLH *medium*, *loose* and *tight* variables. (a) for 1-prong case and (b) for 3 prong case.
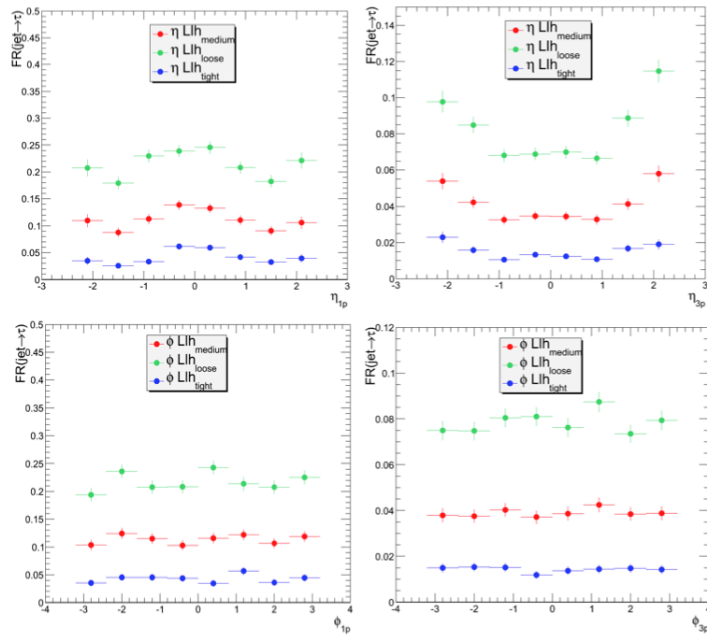
Figure 5.6: Fake rate as a function of τ-LLH versus η and ϕ. On the top the fake rate as a function of η for 1-prong on the left, and 3-prong on the right. On the bottom, similar representation for ϕ case.
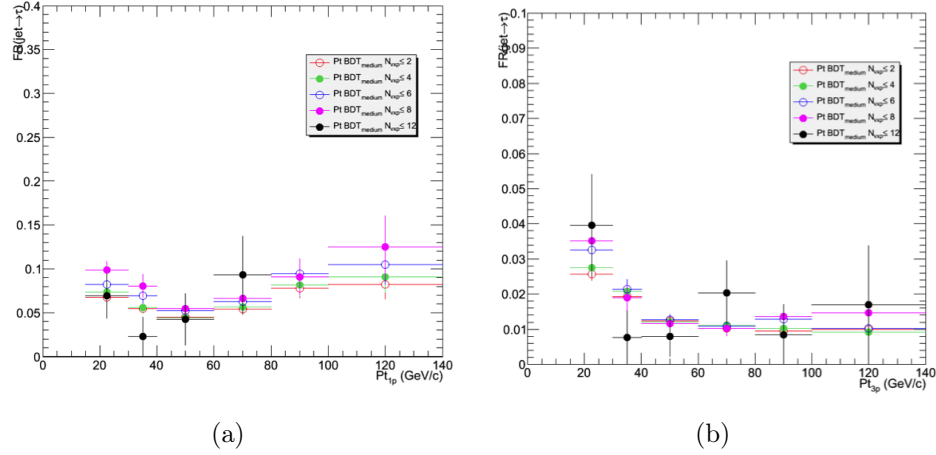
Figure 5.7: Mis-identification probability as a function of the p_T for different $\gamma +$ *jets* topologies, characterized by the number of primary vertices <2, 4, 6, 8, 10 and 12. 1-*prong* case on the left and 3-*prong* case on the right.

show values closer to the expected ones, with the higher ones below to 0.15. The probabilities range from 0.02% to 0.13% for 1-*prong* case, and from 0.005% to 0.04% for 3-*prong* case. The results are consistent with the referenced ones [62], displayed in figure 5.8 for 1-*prong* case and *tight* working conditions.

5.2   Data and Simulation Samples

This analysis uses *pp* collision data recorded by the ATLAS detector in 2011 with a center-of-mass energy of $\sqrt{s} = 7$ TeV. It includes *luminosity blocks* (segments of ATLAS data runs) if they were collected during periods in which the LHC was circulating stable colliding beams and all detector components of ATLAS were producing data of sufficient quality to E_T^{miss} determination, electron, muon and jet identification, to be used for physics analyses. The total integrated luminosity for the sample is calculated to be 4.73 fb^{-1}, considering the luminosity block selection. The estimated luminosity has an uncertainty of 1.8% [35].

Simulation samples are used to optimize the selection procedures, calculate the signal acceptance, and evaluate the contributions from some background processes:

- For $t\bar{t}$ signal, the Powheg [95] generator is used with an assumed top-quark mass of 172.5 GeV and with the NLO parton density function (PDF) set CTEQ66 [37].

- To model background processes such as $W + jets$, Z+jet, and diboson (WW, WZ, ZZ) events production with multiple jets, single top quark events and
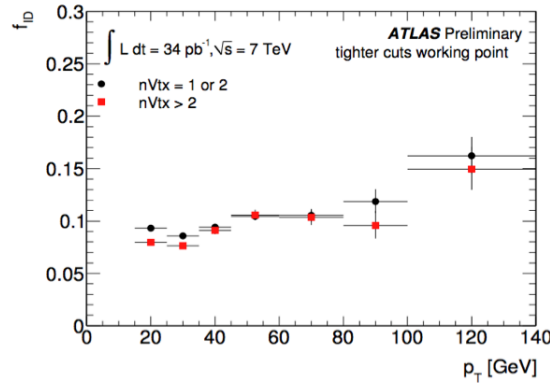
Figure 5.8: Reference plot from [62], for measured mis-identification probability of τ leptons in γ+jet channel with the primary vertex representation. The values of the low p_T obtained in this work are consistent with the expected values.

diboson WW, WZ, and ZZ with multi-jets events are used. W+jets events with up to 5 partons and Z/γ^*+jets events with $m(\ell^+\ell^-)>40$ GeV and up to 5 partons are generated by the ALPGEN generator [93].

- The MLM matching scheme of the ALPGEN generator is used to remove overlaps between n and $n+1$ parton samples with parameters RCLUS=0.7 and ETCLUS=20 GeV.

- The LO PDF set CTEQ6L is used for all backgrounds described above.

- The next-to-leading (NLO) generator [94] MC@NLO is used for single top-quark production, invoking the 'diagram removal scheme' to remove overlaps between the single top quark and the $t\bar{t}$ final states.

The production cross-section of $t\bar{t}$ in Monte Carlo samples is normalized to 177.3 pb as obtained from approximate NNLO+NNL calculations [40]. The cross-sections for W/Z+jets and diboson with jets have been rescaled by a factor of 1.2 to match NNLO calculations of their inclusive cross-sections. Furthermore, the Alpgen W/Z+jets MC samples do not correctly reproduce the jet multiplicity in data. Scale factors derived by comparing event selections in data with the Alpgen MC have been applied. In the case of application to $Z \to \tau\tau$, the scale factors for Z+jets depend on the true MC p_T of the Z: in order to ensure that the kinematic range of the $Z \to \mu\mu$ and $Z \to ee$ (from which the scale factors have to be derived) have to match (or be similar) to the ones of the $Z \to \tau\tau$ (were the energy is lower due to the neutrino decay), the corresponding scale factors have to be applied (see the calculation in section 5.3).

All samples that use HERWIG [41] for parton evolution and hadronization rely on JIMMY [43] for the underlying event model. The τ decays are handled by TAUOLA [44]. On average, eight pile-up events are overlaid in all simulated events. After event generation, all samples are processed by the standard ATLAS detector and trigger simulation software and are subjected to the same reconstruction algorithms as for data. All samples are from 2011 MC production and they are listed in [69].

5.3 Z+jets scale factors calculation

The Z+jets MC production obtained by a simulator, does not reproduce in a right way the observed jet multiplicity in data. For this reason, scale factors are calculated to bring the MC into a closer agreement with data. They add a parametrization by Zp_T, which is necessary for the application to the $Z \to \tau\tau$ samples. To obtain the correction factors, they are derived by comparing Z selection in MC and data in regions of jet multiplicity, applying to the same simulation samples as well as those of $Z \to \tau\tau$, using $Z \to ee$ ($Z \to \mu\mu$) events that can be selected in data with very low background contamination.

5.3.1 Event Selection for Z scale factors calculation

Cleaned Z events can be obtained using the ee ($\mu\mu$) channels. The events of Z$\to ee$ (Z$\to \mu\mu$) have been selected by:

- requiring exactly two opposite signed isolated electrons (muons),

- the firing of a single electron (muon) trigger (corresponding to the flavor of the fired trigger),

- the reconstructed Z mass must be in the window $80 < M_Z < 100$ GeV,

- sideband of events in which $60 < M_Z < 70$ GeV or $110 < M_Z < 120$ GeV, are subtracted as background.

Events passing this selection are classified according to the number of jets with $p_T > 25$ GeV, in order to derive the jet multiplicity dependent correction factors. Electrons, muons, and jets are required to get over the object selection criteria described in Section 5.1.

5.3.2 Z scale factors per jet multiplicity and in bins of p_T

Scale factors are evaluated by comparing the efficiencies between simulated Z events in MC and the ones in data. The central value is applied to MC to absorb the difference between MC and data, and its error becomes a systematic uncertainty. The lepton momentum scale and the resolution, as well as its uncertainties are evaluated by MC, allowing to reproduce the invariant mass of the dilepton system in data.

Figure 5.9, shows the M_Z distributions in bins of jet multiplicity for $Z \to ll$, being $ll = ee, \mu\mu$. The Z mass peak reconstructed from the two leptons is showed before $80 < M_Z < 100$ GeV requirement and sideband subtraction for zero, one and more than two jets. It is showed how the background subtracted in data is small and almost negligible the effect of the subtraction on the true number of Z's. The scale factors derived from the ratio of the total number of events in data and MC calculated for each $Z \to ll$ are listed in table 5.2. They are derived using $Z \to \mu\mu$ and $Z \to ee$ separately.

Figure 5.10, shows Zp_T distributions in bins of jet multiplicity for $Z \to ll$ after the sideband subtraction. There are small differences at low Zp_T between data and MC, as can be seen in the plots, which explains why the scale factor are needed. In the 0 jet samples it can be observed less MC events at low Zp_T than in data, while it is the opposite for 1 and more than 2 jets samples.

Table 5.3 shows the obtained scale factors. The differences between $Z \to ee$ and $Z \to \mu\mu$, come of the order of the statistical uncertainty if the p_T of the muons is required to be larger than 25 GeV, as it is for the electrons. The scale factors applied to $Z \to \tau\tau$ are derived as a function of the p_T of the Z's, ensuring that the kinematics between $Z \to ll$ and $Z \to \tau\tau$ is the same prior to the Z decay.

5.3.3 Final Z Scale Factors

The scale factors calculated as the average of the ones obtained with both $Z \to ee$ and $Z \to \mu\mu$ selections, are displayed in this section.

Tables 5.4, 5.5 and 5.6, show the values in bins of the p_T of the Z, corresponding to a number of jets in the event of ≥ 0, ≥ 1 and ≥ 2. These numbers come into the average of the values represented in the figures on the right of each table (figures 5.11, 5.12 and 5.13). The distributions show the scale factors as function of Zp_T, separated for $Z \to ee$ and $Z \to \mu\mu$ selections, where the binning from table 5.3 is appreciated, allowing to see the dependences.
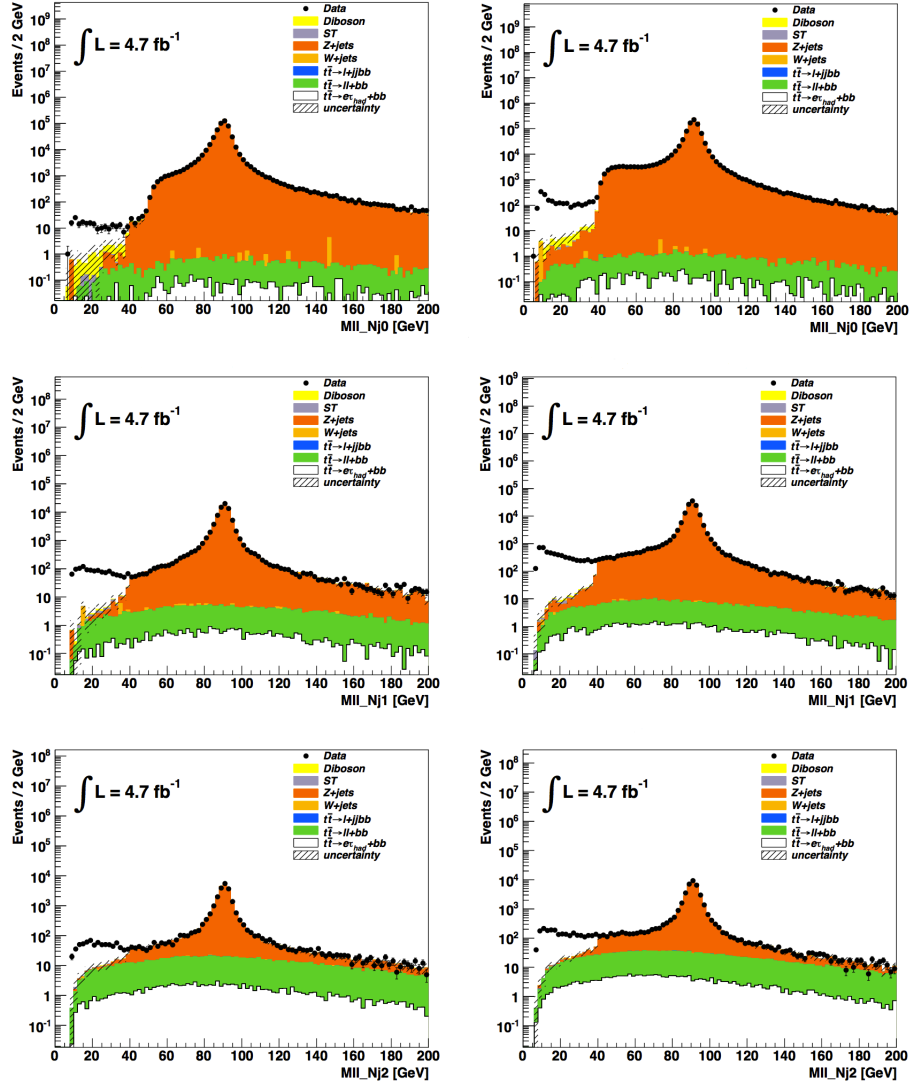
Figure 5.9: Z mass peak reconstructed from the two leptons for $Z \rightarrow ee + jets$ on the left and $Z \rightarrow \mu\mu + jets$ on the right, before $80 < \mathrm{M}_Z < 100$ GeV requirement and sideband subtraction. Figures in the top are for 0 jets, middle for 1 jet, and bottom is for 2 or more jets.

Table 5.2: The scale factors (SF) per number of jets in the event. The scale factors are given by the ratio of events in MC and data per jet multiplicity bin after the sideband subtraction.

		ee	
no.jets	data	MC	SF
0	$5.200\cdot10^5$	$5.590\cdot10^5$	0.931 ± 0.001
1	$0.816\cdot10^5$	$0.825\cdot10^5$	0.989 ± 0.003
≥ 2 jets	$0.234\cdot10^5$	$0.232\cdot10^5$	1.010 ± 0.007

		$\mu\mu$	
no.jets	data	MC	SF
0	$9.200\cdot10^5$	$9.740\cdot10^5$	0.944 ± 0.001
1	$1.530\cdot10^5$	$1.490\cdot10^5$	1.030 ± 0.003
≥ 2 jets	$0.434\cdot10^5$	$0.410\cdot10^5$	1.060 ± 0.005

Figure 5.10: Zp_T reconstructed from the two leptons for Z→ee (top) and Z→ $\mu\mu$ (bottom). The distributions are displayed after $80 < M_Z < 100$ GeV requirement and Z mass sideband subtraction, for two leptons and 0 jet (figures on the left), 1 jet (center) and 2 or more jets (on the right).

Table 5.3: The scale factors, in bins of the p_T of the Z and the number of jets in the event obtained from Z→ee and Z→ $\mu\mu$.

	Z-p_T (ee) SF	**Z-p_T ($\mu\mu$) SF**
0 jets		
0-10 GeV	0.942 ± 0.003	0.958 ± 0.003
10-20GeV	0.897 ± 0.005	0.905 ± 0.003
20-30GeV	0.922 ± 0.008	0.923 ± 0.006
30-40GeV	1.020 ± 0.015	1.030 ± 0.011
40-50GeV	1.090 ± 0.029	1.180 ± 0.022
50-60GeV	1.140 ± 0.049	1.200 ± 0.035
60-70GeV	1.190 ± 0.076	1.070 ± 0.048
70-80GeV	1.000 ± 0.092	1.040 ± 0.067
80-100GeV	0.921 ± 0.095	0.919 ± 0.067
100-200GeV	0.965 ± 0.122	0.738 ± 0.073
1 jets		
0-10 GeV	0.733 ± 0.022	0.759 ± 0.017
10-20GeV	0.986 ± 0.021	1.030 ± 0.016
20-30GeV	0.989 ± 0.016	1.040 ± 0.013
30-40GeV	0.982 ± 0.016	1.010 ± 0.012
40-50GeV	0.993 ± 0.018	1.070 ± 0.014
50-60GeV	1.040 ± 0.023	1.100 ± 0.017
60-70GeV	1.080 ± 0.029	1.090 ± 0.021
70-80GeV	1.050 ± 0.035	1.070 ± 0.026
80-100GeV	1.060 ± 0.033	1.050 ± 0.025
100-200GeV	0.992 ± 0.030	0.997 ± 0.025
≥ 2 jets		
0-10 GeV	0.828 ± 0.051	0.914 ± 0.041
10-20GeV	1.020 ± 0.046	1.060 ± 0.035
20-30GeV	0.993 ± 0.041	1.020 ± 0.030
30-40GeV	1.020 ± 0.041	1.080 ± 0.031
40-50GeV	0.979 ± 0.041	1.100 ± 0.032
50-60GeV	1.000 ± 0.043	1.130 ± 0.034
60-70GeV	1.090 ± 0.050	1.090 ± 0.035
70-80GeV	1.060 ± 0.052	1.100 ± 0.039
80-100GeV	1.070 ± 0.042	1.030 ± 0.031
100-200GeV	1.010 ± 0.031	1.020 ± 0.026

Table 5.7, shows the final values for Z scale factors per number of jets in the event. It is represented the number of Z's in *Zll* for data and MC, given by the ratio of the number of data and MC per jet multiplicity bin, obtained as well as the average of the values in Z*ee* and Z$\mu\mu$ (which come from the values showed in table 5.2). Since the Z$\mu\mu$ and Z*ee* have been averaged, the observed differences are twice as large as the separated uncertainties.

Complementary studies checking the dependency of the scale factors with η and BDT$_j$ shape, can be seen in Appendix B. A more refined calculation of the scale factors using the same technique can be found in [63]. The rest of the analysis, including the cutflow table for data and MC comparison after applying the different events selections and the cross-section calculation of the top quark pair ($t\bar{t}$) production with a lepton and a hadronically decaying τ-lepton in the final state, apply the separated values for muons and electrons selection.

Table 5.4: The scale factors values obtained as the average from Z$\to$ *ee* and Z$\to$ $\mu\mu$, in bins of the p_T of the Z and the number of jets in the event ≥ 0.

Z-p_T	Scale Factors
0 jets	
0 - 10 GeV	0.950 ± 0.003
10-20GeV	0.901 ± 0.004
20-30GeV	0.923 ± 0.007
30-40GeV	1.025 ± 0.013
40-50GeV	1.135 ± 0.025
50-60GeV	1.170 ± 0.042
60-70GeV	1.130 ± 0.062
70-80GeV	1.020 ± 0.079
80-100GeV	0.920 ± 0.081
100-200GeV	0.852 ± 0.097
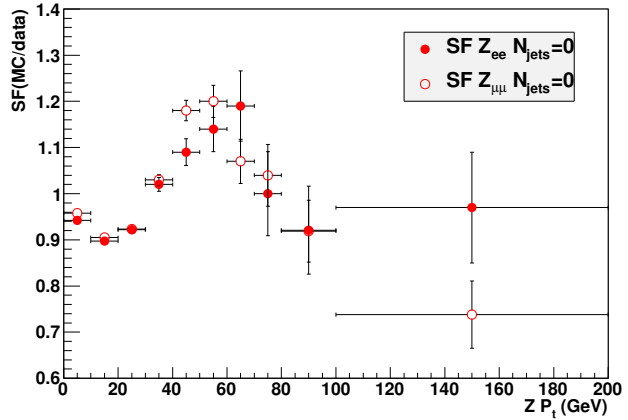
Figure 5.11: The scale factors distribution separated for Z$\to$ *ee* and Z$\to$ $\mu\mu$ selections, in bins of the p_T of the Z and the number of jets in the event ≥ 0.

Table 5.5: The scale factors values obtained as the average from Z→ ee and Z→ $\mu\mu$, in bins of the p_T of the Z and the number of jets in the event ≥ 1.

Z-p_T	Scale Factors
1 jets	
0 - 10 GeV	0.746 ± 0.019
10-20GeV	1.008 ± 0.019
20-30GeV	1.015 ± 0.015
30-40GeV	0.996 ± 0.014
40-50GeV	1.032 ± 0.016
50-60GeV	1.070 ± 0.020
60-70GeV	1.085 ± 0.025
70-80GeV	1.060 ± 0.030
80-100GeV	1.055 ± 0.029
100-200GeV	0.995 ± 0.027
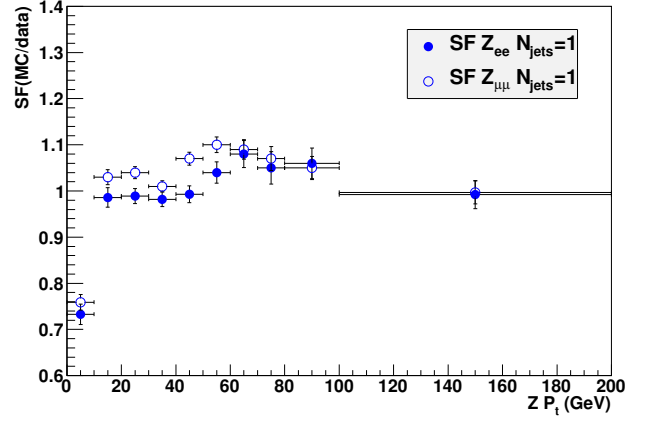
Figure 5.12: The scale factors distribution separated for Z→ ee and Z→ $\mu\mu$ selections, in bins of the p_T of the Z and the number of jets in the event ≥ 1.

Table 5.6: The scale factors values obtained as the average from Z→ ee and Z→ $\mu\mu$, in bins of the p_T of the Z and the number of jets in the event ≥ 2.

Z-p_T	Scale Factors
≥ 2 jets	
0 - 10 GeV	0.871 ± 0.046
10-20GeV	1.040 ± 0.041
20-30GeV	1.007 ± 0.035
30-40GeV	1.050 ± 0.036
40-50GeV	1.040 ± 0.036
50-60GeV	1.065 ± 0.039
60-70GeV	1.090 ± 0.043
70-80GeV	1.080 ± 0.045
80-100GeV	1.050 ± 0.037
100-200GeV	1.015 ± 0.029
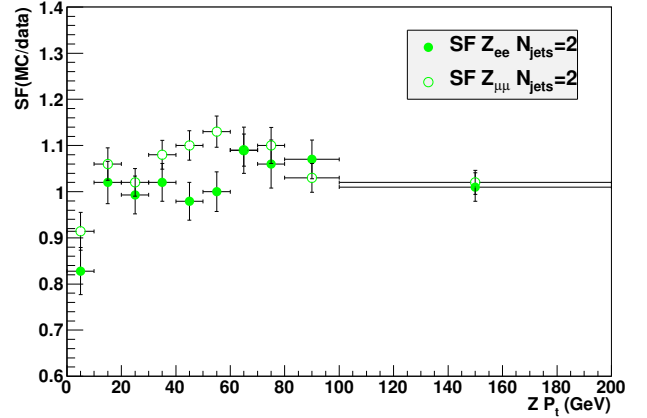
Figure 5.13: The scale factors distribution separated for Z→ ee and Z→ $\mu\mu$ selections, in bins of the p_T of the Z and the number of jets in the event ≥ 2.

Table 5.7: Number of Z in Zll data and MC. The scale factors are given by the ratio of the number of data and MC per jet multiplicity bin, calculated as the average of the numbers obtained from Zee and Z$\mu\mu$ individual samples.

	average		
no.jets	data	MC	SF
0	$7.200 \cdot 10^5$	$7.670 \cdot 10^5$	0.938 ± 0.001
1	$1.170 \cdot 10^5$	$1.160 \cdot 10^5$	1.010 ± 0.003
≥ 2 jets	$0.334 \cdot 10^5$	$0.321 \cdot 10^5$	1.035 ± 0.005

5.4 Event Selection for Top quark production cross-section

This section describes the event selection performed to measure the top quark production cross-section, where the final states with a lepton and a hadronically decaying τ-lepton are represented as $t\bar{t} \rightarrow W(\rightarrow \tau_{had}\nu_\tau)W(\rightarrow l\nu_l)b\bar{b}$ and $t\bar{t} \rightarrow W(\rightarrow \tau_{had}\nu_\tau)W(\rightarrow \tau(\rightarrow l\nu_l\nu_\tau)\nu_\tau)b\bar{b}$, being l the representation of an electron or a muon, and τ_{had} the hadronically decaying τ-lepton. The electron $(e + \tau)$ and the muon $(\mu + \tau)$ channels are considered for the study. A preselection process is performed with an event cleaning algorithm to remove events with known problems and the ones not coming from collisions. The selected events are required to fulfill the following conditions:

- the events are selected online by a single lepton trigger, which varies by data-taking period. The corresponding triggers are listed in [69], with more detailed descriptions. The fired trigger defines which channel the events go with;

- an event must contain a primary vertex with at least five tracks;

- if any jet with $p_T > 20$ GeV fails the jet quality selections, the event is discarded [54];

- one and only one isolated lepton (e or μ);

- at least one τ candidate;

- $E_T^{miss} > 30$ GeV, which allows to reduce QCD multi-jet background;

- at least two jets with $p_T > 25$ GeV not overlapping with one τ candidate. The overlapping jet is the closest jet to a τ candidate within $\Delta R(\tau, jet) < 0.4$.

In the case of two τ candidates a τ_1 is kept if the other is a τ_3. If both are τ_1 or τ_3 both are kept.

- the τ candidate and the lepton must have opposite charge;

- at least one jet identified as b-jet (≥ 1 b-tag). The MV1 tagger is used by requiring a discriminant value ≥ 0.607 (70% efficiency point). Events with ≥ 2 b-tags are also used to test consistency.

The number of observed and expected events after each cut for an integrated luminosity of approximately 4.73 fb^{-1} are shown in table 5.8 for channel $(e + \tau)$ and in table 5.9 for channel $(\mu + \tau)$. First column shows the main representative cuts performed in the selections; the rest of the columns represent the contribution of the different backgrounds ($t\bar{t}(\ell\tau_{had})$, $t\bar{t}(\ell jet)$, $t\bar{t}(\ell\ell)$, Z + jets, W + jets, Single Top, Diboson and the sum of all) and data events after each cut.

After the E_T^{miss} requirement, the Z background is reduced; also an important quantity of QCD background is decreased and in a lesser amount the W+jets. Then, the remaining backgrounds are from W+jets and $t\bar{t} \to l + jets$, where a jet is misidentified as a τ candidate. The W+jets background is then reduced by the b-tag requirement. The events named $t\bar{t}(\ell\ell')$, are $t\bar{t}$ dilepton events with only one lepton reconstructed as a lepton and another lepton or jet reconstructed as a τ. The errors are the statistical uncertainties.

When multiple τ candidates are found, the event is only counted once in the cutflow tables. In section 5.6, where an ameliorated background method for cross section measurement is described, the BDT_j distributions used for the fitting to extract the signal, takes all candidates in the event. In this part of the analysis, it is determined the number of real taus in the signal region using a template fitting procedure. The event selection separates the 1-*prong* and 3-*prong* τ candidates due to the fact that the fitting is performed on the two distributions separately. As the 1-*prong* sample has a significantly higher signal to background ratio, the fitting studies are focused on this sample exclusively.

Table 5.8: $e + \tau$ cut flow for τ_1 and τ_3. $t\bar{t}(\ell\ell')$ are $t\bar{t}$ dilepton events with only one lepton reconstructed as a lepton and a lepton or jet reconstructed as a τ. The errors are the statistical uncertainties.

e 1p-Cut	$t\bar{t}(\ell\tau_{had})$	$t\bar{t}(\ell jet)$	$t\bar{t}(\ell\ell)$	Z + jets	W + jets	Single Top	Diboson	MC Total	Data
$\geq 1\ \tau$ cand	1071 ± 7	4683 ± 15	257 ± 4	41920 ± 130	173182 ± 524	1166 ± 16	1726 ± 8	224005 ± 540	276430
$N_{jet} > 2$	827 ± 6	4328 ± 14	203 ± 3	6697 ± 35	12565 ± 88	571 ± 10	390 ± 4	25580 ± 96	30825
$E_T^{miss} > 30$	711 ± 6	3397 ± 13	182 ± 3	1889 ± 18	8773 ± 73	431 ± 9	238 ± 3	15621 ± 77	16463
OS	697 ± 6	2312 ± 11	100 ± 2	1167 ± 15	5525 ± 57	313 ± 7	158 ± 2	10271 ± 61	10404
≥ 1 b−jet	588 ± 5	1841 ± 9	76 ± 2	97 ± 4	328 ± 14	219 ± 6	18 ± 1	3167 ± 19	3382
≥ 2 b−jet	240 ± 3	660 ± 5	24 ± 1	5 ± 1	17 ± 3	40 ± 3	1 ± 0	988 ± 8	1079
e 3p-Cut	$t\bar{t}(\ell\tau_{had})$	$t\bar{t}(\ell jet)$	$t\bar{t}(\ell\ell)$	Z + jets	W + jets	Single Top	Diboson	MC Total	Data
$\geq 1\ \tau$ cand	393 ± 4	14854 ± 26	870 ± 6	72660 ± 168	430700 ± 806	3009 ± 27	3531 ± 11	526016 ± 824	786278
$N_{jet} > 2$	302 ± 4	13496 ± 25	677 ± 6	15739 ± 53	33144 ± 142	1420 ± 16	787 ± 5	65564 ± 154	84685
$E_T^{miss} > 30$	257 ± 4	10615 ± 22	602 ± 5	4002 ± 27	23357 ± 119	1079 ± 14	484 ± 4	40395 ± 125	44889
OS	248 ± 3	6732 ± 18	307 ± 4	2061 ± 19	13592 ± 92	689 ± 11	296 ± 3	23925 ± 96	26108
≥ 1 b−jet	212 ± 3	5399 ± 16	233 ± 3	175 ± 6	917 ± 29	473 ± 9	36 ± 1	7444 ± 35	8200
≥ 2 b−jet	90 ± 2	1971 ± 9	72 ± 2	11 ± 1	81 ± 13	96 ± 4	3 ± 0	2323 ± 17	2499

Table 5.9: $\mu + \tau$ cut flow for both τ_1 and τ_3 candidates. $t\bar{t}(\ell\ell')$ are $t\bar{t}$ dilepton events with only one lepton reconstructed as a lepton and a lepton or jet reconstructed as a τ. The errors are the statistical uncertainties.

μ 1p-Cut	$t\bar{t}(\ell\tau_{had})$	$t\bar{t}(\ell jet)$	$t\bar{t}(\ell\ell)$	Z + jets	W + jets	Single Top	Diboson	Total	Data
$\geq 1\ \tau$ cand	1362 ± 8	6097 ± 17	326 ± 4	49097 ± 137	275302 ± 680	1488 ± 18	2283 ± 9	335955 ± 695	450885
$N_{jet} > 2$	1062 ± 7	5635 ± 16	261 ± 4	3546 ± 25	19943 ± 120	706 ± 11	448 ± 4	31601 ± 124	40255
$E_T^{miss} > 30$	921 ± 7	4528 ± 15	234 ± 3	1587 ± 17	14584 ± 103	559 ± 10	318 ± 3	22730 ± 106	23536
OS	908 ± 7	3089 ± 12	130 ± 3	1134 ± 14	9150 ± 80	399 ± 8	216 ± 3	15025 ± 82	14773
≥ 1 b$-$jet	756 ± 6	2467 ± 11	98 ± 2	107 ± 5	537 ± 20	274 ± 7	24 ± 1	4262 ± 25	4567
≥ 2 b$-$jet	314 ± 4	894 ± 6	32 ± 1	9 ± 2	33 ± 5	53 ± 3	2 ± 0	1337 ± 9	1393
μ 3p-Cut	$t\bar{t}(\ell\tau_{had})$	$t\bar{t}(\ell jet)$	$t\bar{t}(\ell\ell)$	Z + jets	W + jets	Single Top	Diboson	Total	Data
$\geq 1\ \tau$ cand	497 ± 5	19275 ± 30	1124 ± 7	66010 ± 161	682273 ± 1044	3980 ± 31	4678 ± 13	777837 ± 1058	1276463
$N_{jet} > 2$	382 ± 4	17502 ± 29	876 ± 6	6275 ± 33	52025 ± 190	1775 ± 18	908 ± 6	79742 ± 196	109665
$E_T^{miss} > 30$	330 ± 4	14099 ± 26	785 ± 6	2502 ± 21	38325 ± 162	1396 ± 16	647 ± 5	58085 ± 166	64073
OS	321 ± 4	8949 ± 21	406 ± 4	1359 ± 15	22263 ± 123	900 ± 13	401 ± 4	34599 ± 127	37195
≥ 1 b$-$jet	271 ± 4	7189 ± 18	313 ± 4	136 ± 5	1447 ± 37	612 ± 10	52 ± 1	10019 ± 43	11579
≥ 2 b$-$jet	113 ± 2	2636 ± 11	96 ± 2	10 ± 1	105 ± 10	130 ± 5	4 ± 0	3095 ± 16	3432

5.5   Data and MC comparison

The resulting events after the selection cuts, displayed in tables 5.8 and 5.9, show that the dominant background comes from QCD processes before the cut on E_T^{miss}. These differences are mainly attributed to multi-jet events, which are not included in the previous MC expectations. As the available multi-jet events in MC suffer from low statistics, the multi-jet contribution is derived from data using the same event selection as the main $(\tau + e)$ and $(\tau + \mu)$, but with the isolation requirement on the e and μ inverted. Doing this, the modeling for the QCD multi-jet background has been built using anti-isolated data employed as a control region. At each stage of the event selection, QCD events are normalized using χ^2 fits in $M_T(l, E_T^{\mathrm{miss}})$ distribution, with QCD template. More details about the QCD studies can be found in [69].

Both the QCD templates and the normalization factors at each stage of the selection have been taken from [45]. After all selections the multi-jet background is insignificant. Following the cut on E_T^{miss} and before the 1 b-tag cut, the dominant background is the W+jet process as it was indicated before, being the $t\bar{t} \to l+jets$ the dominant one after the 1 b-tag cut. The majority of the background comes from jet faking τ. The background models for this analysis are derived from data, so the multi-jet background, MC distributions and uncertainties do not affect the cross section measurement.

Figure 5.14 compare τ_1 distributions between data and Monte Carlo, at the relevant stages of the event selection. The distributions show, for the 1-*prong* case, the invariant mass (M_t) before and after the 1 b-tag cut, in both e and μ channels. The black dots distributions correspond to the experimental data, while the MC simulated data are represented by colored histograms. The plots at the bottom of each representation show the relation (Data$-$MC)/MC. The agreement between data and MC is acceptable within the uncertainty. The uncertainties in these representations are refereed to statistical ones. Figure 5.15, shows the 1-*prong BDT* distributions before and after the 1 b-tag cut, for both electron and muon channels, superimposed to the MC samples. Figures 5.16 and 5.17, show respectively the data/MC comparison for the E_T^{miss} distribution before E_T^{miss} requirement, and the data/MC comparison for the number of jets distribution, also before E_T^{miss} requirement.

Following this, the analysis continues with the study of the new background technique to estimate the Cross-Section, applied with 4.73 fb^{-1} samples.
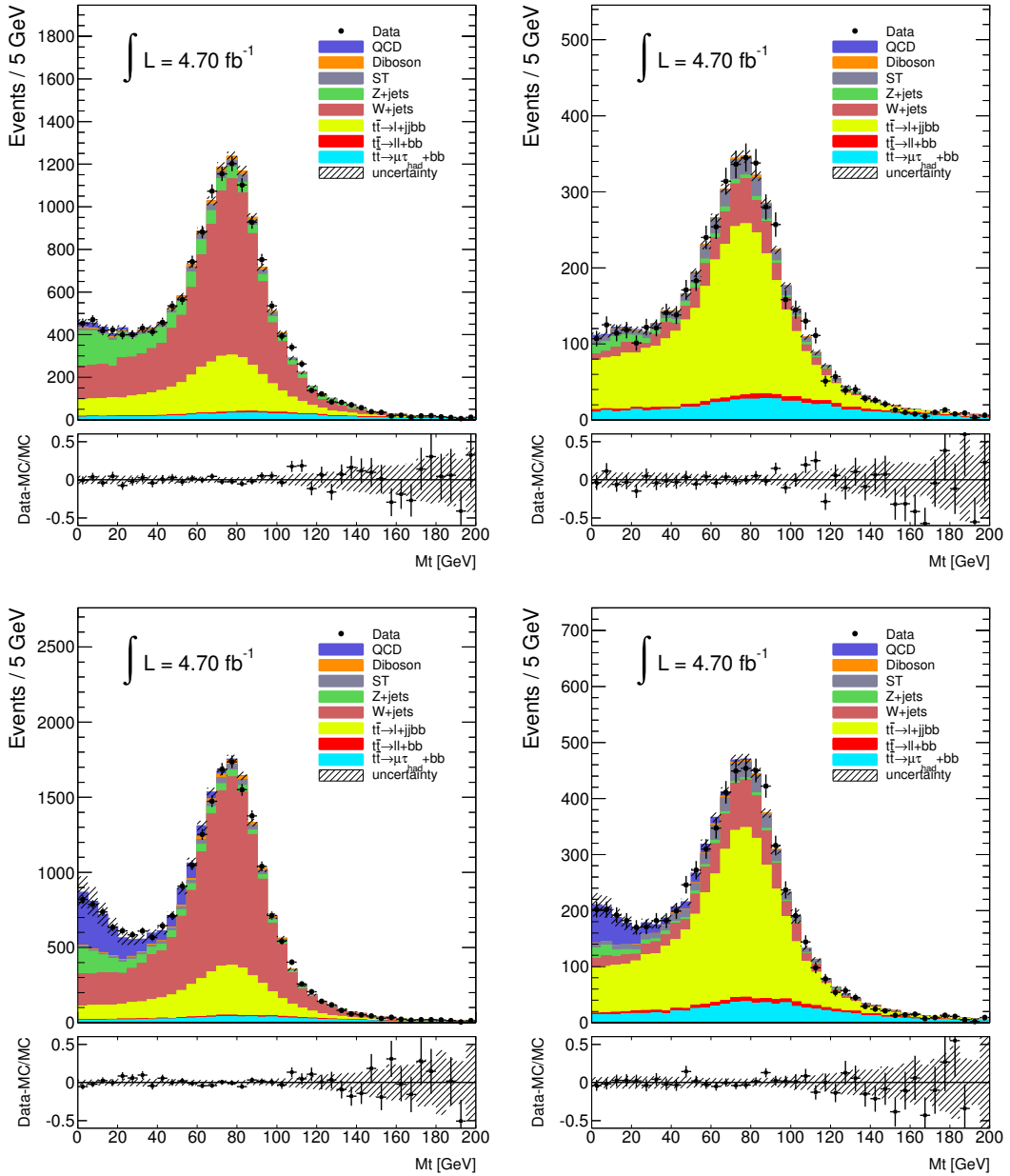
Figure 5.14: Data/MC comparison for the invariant mass (M_t). The distributions are displayed for τ_1 in ($e + \tau$) channel (top) and ($\mu + \tau$) channel (bottom). On the left, before the 1 b-tag cut and on the right, after 1 b-tag cut. The plots at the bottom show the relation (Data-MC)/MC.
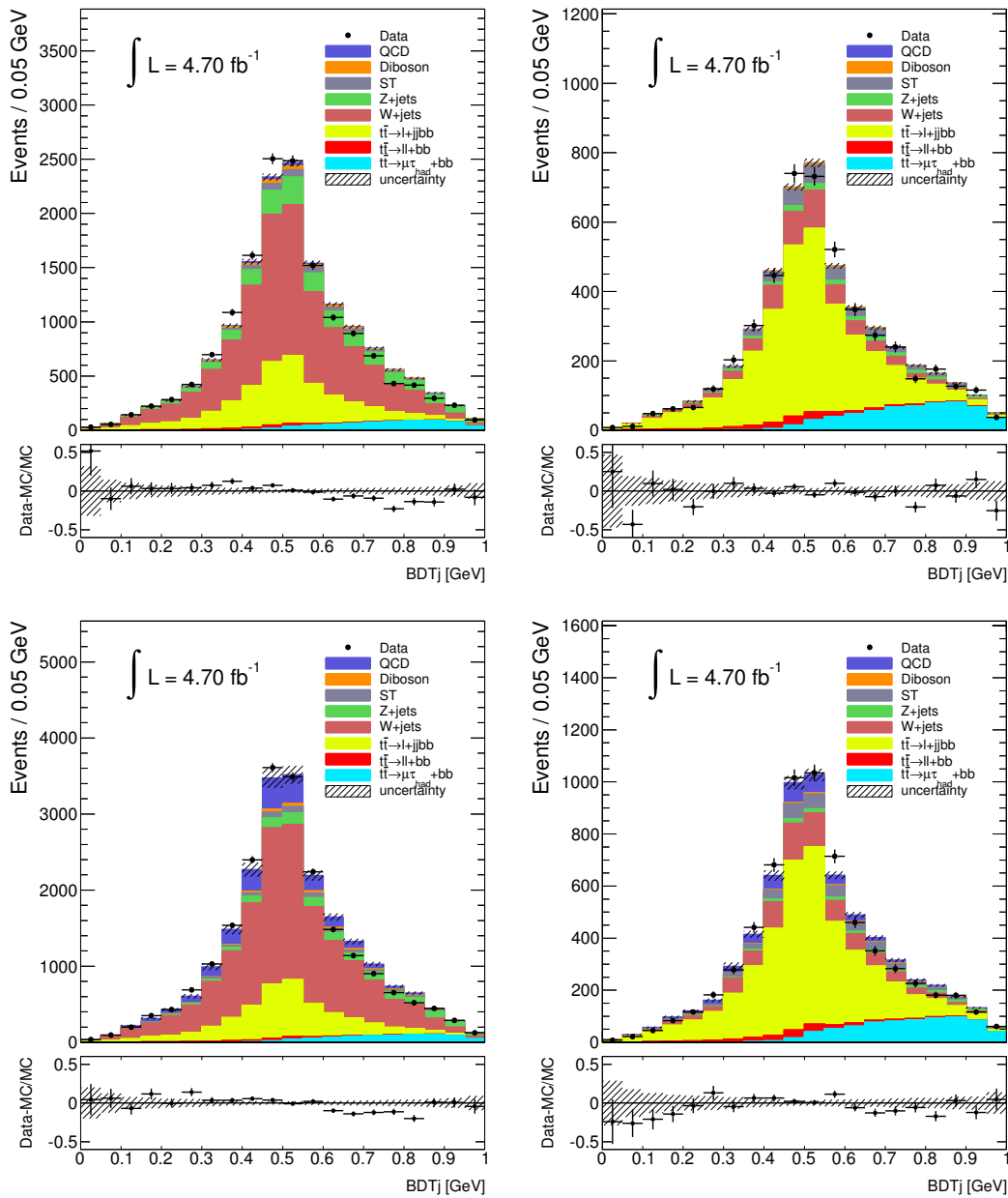
Figure 5.15: Data/MC comparison for the BDT distributions. Figures are displayed for τ_1 in $(e + \tau)$ channel (top) and $(\mu + \tau)$ channel (bottom). On the left, before the 1 b-tag cut and on the right, after 1 b-tag cut. The plots at the bottom show the relation (Data-MC)/MC.
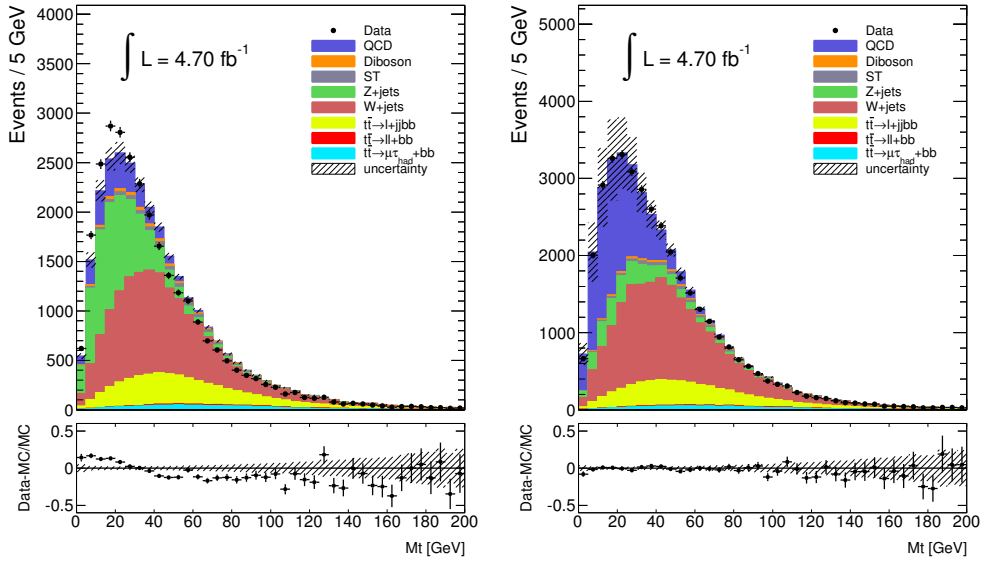
Figure 5.16: τ_1 data/MC comparison for the E_T^{miss} distribution, before E_T^{miss} requirement, on the left for $(e + \tau)$ channel and on the right for $(\mu + \tau)$ channel. The plots at the bottom show the relation (Data-MC)/MC. The plots at the bottom show the relation (Data-MC)/MC.
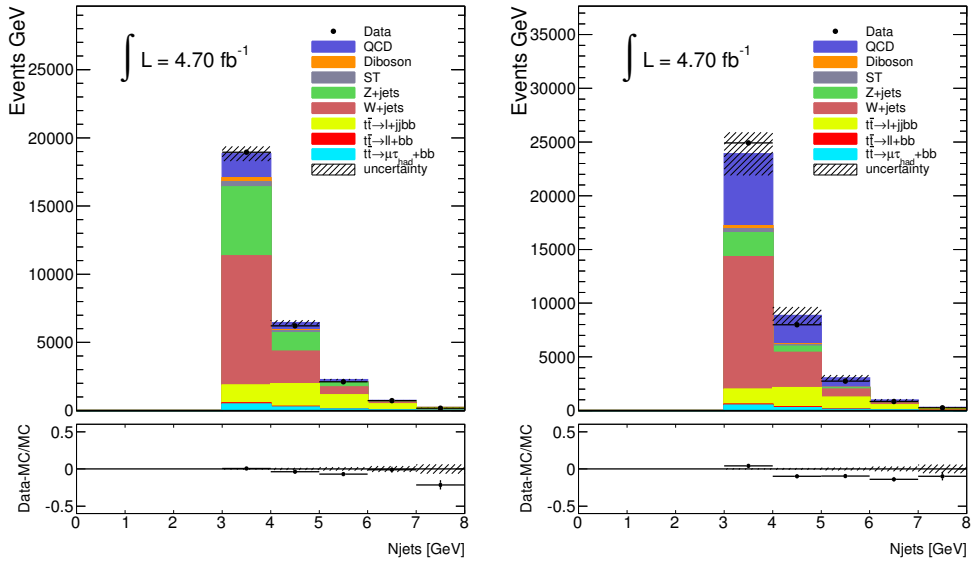
Figure 5.17: Number of jets for 1-*prong* case, in $(e + \tau)$ channel on the left, and in $(\mu + \tau)$ channel on the right. The plots at the bottom show the relation (Data-MC)/MC.

5.6   Background Method for Cross-Section Estimation

A new background technique, based on fitting differentiated templates for gluon and quark jets faking τ lepton, is applied to separate the contribution of processes with τ leptons (signal) from those with jets misidentified as τ (fake τ). BDT_j distributions of selected events are fitted with templates that give the shape for fake τ and τ leptons, where the fake τ template shapes depend on the jet type, with light quark jets reaching higher values of BDT_j than gluon jets. This new background technique developed for 2 fb^{-1} analysis [64], is applied to the whole dataset collected by the ATLAS detector in 2011. In this work it is studied with 4.73 fb^{-1} samples, allowing to ameliorate the background model and aiming to improve the precision of the measurement published with 2 fb^{-1} [68], as well as the background model originated by jets falsifying hadronically decaying tau leptons. Improvements by deeper studies can be found in [69].

The new method fit the OS distribution with background templates in which the sum is the same as for the OS light-quark and gluon misidentified jets. Meaning that BDT_j distributions are obtained for gluon jets misidentified as τ and other differentiated BDT_j distributions, composed mainly by light quark jets OS plus a small mixture of gluon jets coming from $W + jets$ control samples. This new method, uses the whole OS (where the lepton and τ candidate have opposite charge) data selection, to reduce the statistical uncertainty. The background model is improved, including not only the W+jets for the light quarks, but also gluons. Studies on hadronic τ identification using W+jets events, support this new fitting method: a deeper description of the method is given in [63].

The data set is composed of OS $W + 1$ jet, which is rich in light quarks, and SS $W + 1$ jet, which is a mixture of gluons and light quark jets. The quantity of gluons jets in OS and SS data sets should be the same. There are $W + 2$ jets samples where the lower p_T jet has higher probability of being a gluon jet. The fake τ BDT_j taken from OS (SS) $W + 1$ jet data sets is expressed as OS1 (SS1), and similarly OS2 (for SS2) for $W + 2$ jets. In figure 5.18 one can observe the normalized distribution of the BDT variable separated in two p_T regions: the shapes of these distributions can be compared. It is possible to observe the differences between $W + 1$ jet OS and $W + 2$ jets OS. All the distributions of study are showed for the 1-*prong* case.

If the SS distribution is subtracted from the OS distribution (OS-SS) the shapes would be in a very good agreement. These distributions can be described by the next set of equations:

$$\mathrm{OS1} = a_1 \cdot \mathrm{OS_q} + b_1 \cdot Gluons \tag{5.6}$$

$$\mathrm{SS1} = c_1 \cdot \mathrm{SS_q} + b_1 \cdot Gluons \tag{5.7}$$
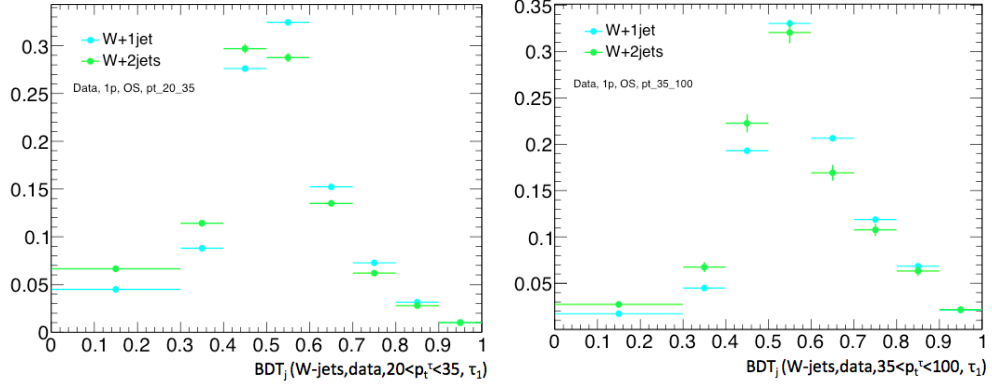
Figure 5.18: BDT_j distributions for τ candidates from $W + 1$ jet and $W + 2$ jets samples for 1-*prong* case. On the left for the first region p_T (25,35) GeV, and on the right for the second one (35,100) GeV.

$$\mathrm{OS2} = a_2 \cdot \mathrm{OS_q} + b_2 \cdot Gluons \tag{5.8}$$

$$\mathrm{SS2} = c_2 \cdot \mathrm{SS_q} + b_2 \cdot Gluons \tag{5.9}$$

where *Gluons* is the corresponding function for gluon jets and $\mathrm{OS_q}$ ($\mathrm{SS_q}$) is a function that characterize the shape of the distribution of light-quark jets contributing to OS (SS). Taking into account that the OS1-SS1 and OS2-SS2 distributions have the same shape, the equations below can be computed as $a_1/c_1 = a_2/c_2$ for each E_T, due that the E_T of τ candidates from $W + 2$ jets is lower than from $W + 1$ jet. Extracting the *Gluons* function from the OS and from the SS distributions separately, the equations can be expressed as:

$$K \cdot Gluon = (N \cdot \mathrm{OS2} - \mathrm{OS1}) \tag{5.10}$$

$$K \cdot Gluon = (N \cdot \mathrm{SS2} - \mathrm{SS1}) \tag{5.11}$$

being N the ratio of the total number of OS1-SS1 events to OS2-SS2 events and $K = N \cdot b_2 - b_1$ is an unknown constant used to extract the *Gluon* function that must be the same for both cases, either SS or OS. In general, the OS1 distributions have higher BDT_j than from gluon jets, due to higher percentage of fake τs from light-quark jets. The extracted gluons ($K \cdot Gluon$ distributions) are showed in figure 5.19. The OS and SS distributions can be added to reduce the statistical uncertainties.

The equation $k_1 \cdot \mathrm{OS1} + k_2 \cdot \mathrm{Gluons}$, can reproduce any BDT_j distribution built with a mixture of light-quark jets and gluons.
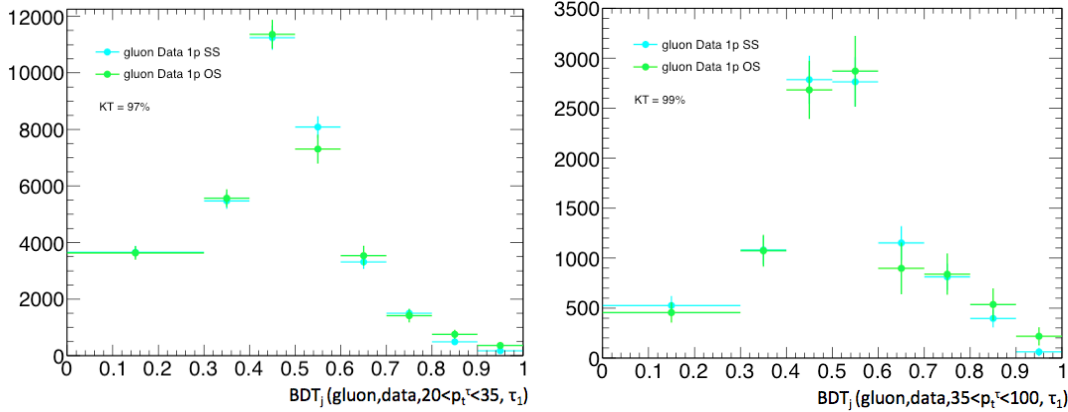
Figure 5.19: BDTj gluon distributions for τ_1 candidates obtained from W+1 jet and W+2 jets OS and SS data samples. On the left for the first region of p_T, (25,35) GeV, and on the right for the second (35,100) GeV.

5.7 Signal extraction by fitting the BDT shape

In this section, the fitting method used to select the signal after a b-tagging requirement and the application of the technique to 4.73 fb^{-1} samples to finally obtain an estimation of the cross-section, is described.

5.7.1 Description of the fitting technique

To perform the template fitting, signal and normalized light quark background are obtained by fitting templates to the data. The selection of events classifies the 1-*prong* and 3-*prong* τ candidates into two templates, and the fit is performed on the two distributions separately. The 1-*prong* sample has a signal with significantly higher ratio with respect to the background, reason why this analysis is focused on this sample. The different types of background can come from processes with a lepton where a jet is misidentified as a τ, from multi-jet processes were both ℓ and τ are misidentified or the ℓ is from a jet not eliminated by the isolation requirement, from processes with two isolated leptons were one of them is mistaken as a τ and from processes other than $t\bar{t}$ that have τ-leptons and an isolated lepton from W decay [69]. The dominant background after preselection and b-tagging selections, is the top quark pair production in the $lepton+jets$ channel, being the TauID the only strong technique for the removal of this background.

Boosted Decision Tree (BDT) selections were introduced as a discriminant variable in the fitting technique (section 5.1.6). This new technique also uses

Boosted Decision Tree τ-jet score (BDT_j), which discriminate shape differences between signal and background. BDT_j distributions for each background process, are different depending of what kind of jet is faking a τ. The procedure is performed on a first step, running all data, MC background and $t\bar{t}$ nominal samples. The signal BDT_j template is derived from MC τ candidates that are truth-matched to a real τ. This MC consist of $t\bar{t} \rightarrow \tau + \ell$ signal, $Z \rightarrow \tau^+\tau^-$, a small contribution from single top and diboson events. The background from processes with two isolated leptons where one of them is misidentified with a τ are mainly $Z \rightarrow ee$ and $t\bar{t}$ events, where the majority of the electrons are eliminated after BDT_e cut and the rest can not be distinguished from τ leptons. Then, the τ candidates truth-matched to real electrons are added to the signal template. The background from processes with a lepton where a jet is misidentified as a τ and from multi-jet processes are considered taken templates derived from data, which consist on gluon jet τ fakes and light-quark jet τ fakes derived from $W+$jets enriched data samples.

A χ^2 fit is performed after enforce the condition that the sum of signal and background must sum up to the number of observed events, using the background and MC signal template:

$$a \cdot \text{W OS} + b \cdot Gluons + c \cdot \text{signal} \tag{5.12}$$

With this fit, the normalization constant that best estimates the BDT_j in the signal region is defined. In this work, the summed e and μ channels results are obtained by fitting the sum of the distributions and the whole study has been performed applying the fits to the samples with at least 1 b-tag, so the collection of events that pass the cuts selection are referred to as the ≥ 1 b-tag and τ_1 samples. Tables 5.10 and 5.11, show the contribution to the signal template.

In summary, as signal events are extracted using the shape to differentiate between signal and background, the distribution of the BDT output score is fitted by the background and the signal template. Then, BDT_j distributions for each background process, are different depending of what kind of jet is faking a τ. Fake τ's originated from gluon or b-jet, normally have lower BDT value. Instead light quarks originated-jet, have an intermediate BDT score between τ and gluon or b-jet.

Table 5.10: Events from Monte Carlo with a true tau matched to the tau candidate that composed the signal template for τ_1. Uncertainties are only statistical.

	$20 \leq P_t^{\tau_1} \leq 35$	$35 \leq P_t^{\tau_1} \leq 100$
	$\tau_{\text{truth}} \rightarrow \tau_{\text{cand}}$	
	≥ 1 b-tag	≥ 1 b-tag
$t\bar{t}(\ell\tau_{had})$	635.4 ± 26.3	645.2 ± 24.8
$t\bar{t}(\ell jet)$	1.2 ± 1.1	1.4 ± 1.2
$t\bar{t}(\ell\ell)$	0.1 ± 0.2	0.1 ± 0.2
Z + jets	54.1 ± 7.3	42.3 ± 7.1
W + jets	0.0 ± 0.0	0.0 ± 0.0
Diboson	1.9 ± 1.6	2.6 ± 1.8
Single Top	24.6 ± 5.2	27.8 ± 5.2
Total	717.3 ± 41.7	719.4 ± 40.3

Table 5.11: Events from MC with a true e matched to the τ candidate that composed the signal template, for τ_1. $t\bar{t}(\ell + \text{jets})$ are $t\bar{t}$ events with one identified lepton and a jet reconstructed as a τ. Sources contributing to jet fakes are W+jets, Z+jets, single top and diboson. Uncertainties are only statistical.

	$20 \leq P_t^{\tau_1} \leq 35$	$35 \leq P_t^{\tau_1} \leq 100$
	$e_{\text{truth}} \rightarrow \tau_{\text{cand}}$	
	≥ 1 b-tag	≥ 1 b-tag
$t\bar{t}(\ell\tau_{had})$	1.5 ± 1.3	0.7 ± 0.9
$t\bar{t}(\ell jet)$	0.2 ± 0.5	0.0 ± 0.0
$t\bar{t}(\ell\ell)$	7.7 ± 2.8	8.1 ± 2.8
Z + jets	1.5 ± 1.4	3.1 ± 1.8
W + jets	0.0 ± 0.0	0.0 ± 0.0
Diboson	0.0 ± 0.1	0.1 ± 0.4
Single Top	0.6 ± 0.9	0.5 ± 0.9
Total	11.5 ± 7.0	12.5 ± 6.8

5.7.2   Application of the fitting technique to 4.73 fb^{-1} samples

Testing the fitting method

The process is tested using two MC samples statistically independent. One of them is used to built the background from jets misidentified as τ candidates for two E_T regions ($20 < E_T < 35$ GeV and $35 < E_T < 100$ GeV). It is fitted with the background templates as it is showed in figure 5.20. The expected background is produced from the expected percentage of $t\bar{t} \rightarrow l + jets$ and $W + jets$. The background template can not reproduce exactly the real background, as the value of χ^2/ndf indicates. Figure 5.21 shows background corrections, that is, the applied difference in % between the fit and the expected background. The signal and background templates are then built with the second MC sample, applying background corrections and performing a fit to extracts the signal in the sample. Figure 5.22 shows the resulted fit for 1 b-*tag*. Figure 5.23 shows the MC fits without correction, displayed to observe the differences with corrected ones. In all the figures, N_{bkg} is the number of events corresponding to MC background, N_{WOS} corresponds to OS W+jets events and N_g to the number of gluons.

After the corrections (figure 5.22), the value of χ^2/ndf is 0.0936 in the first region and 0.0062 in the second one, while the values before the corrections (figure 5.23) are 0.5542 and 1.9325 respectively. The values of the measured signal are 703.64 (first bin) and 721.13 (second bin) after corrections, and 638.69 and 612.41 before them, while the expected signal are 721.69 and 724.75 in each region. Table 5.12 summarizes these fitting results. In spite of a small difference in the expected and measured signal in the first bin of p_T after the corrections, the values of the fits obtained before and after perform them show that the method works well.

Table 5.12: MC expectation and fitting results using statistically independent MC samples as data and for the templates before and after applying corrections. Numbers in the parentheses are χ^2/ndf.

MC fits	S_{MC}	$S_{Fitted}^{BeforeCorrections}$ (χ^2)	$S_{Fitted}^{AfterCorrections}$ (χ^2)
20<E$_T$<35GeV	721.7±6.5	638.7 ±41.3 (0.5542)	703.6 ±51.2 (0.0936)
35<E$_T$<100GeV	724.8±6.4	612.4 ± 39.8 (1.9325)	721.1±39.6 (0.0062)
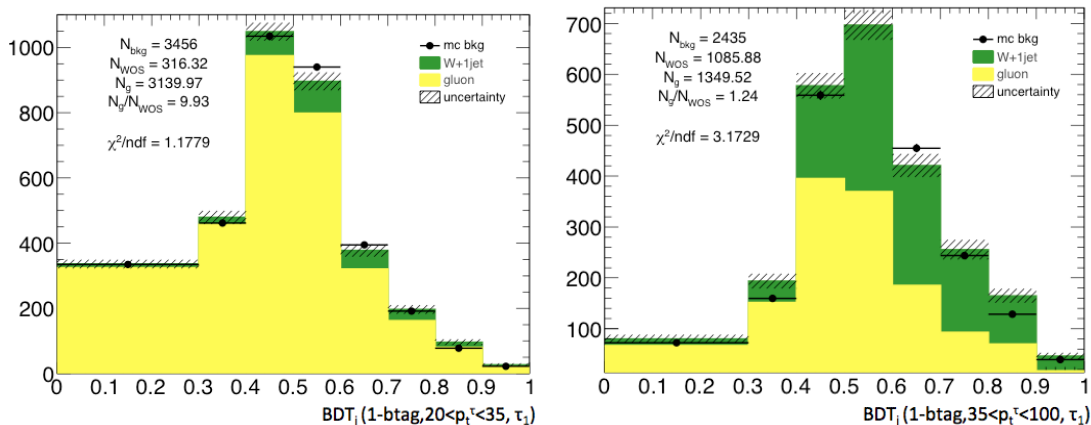
Figure 5.20: MC fits with background templates derived from W+jets MC for τ_1 and events with ≥ 1 b-tag. The fits are performed separately in the first p$_T$ bin on the left ($20 < E_T < 35$ GeV) and the second bin on the right ($35 < E_T < 100$ GeV).
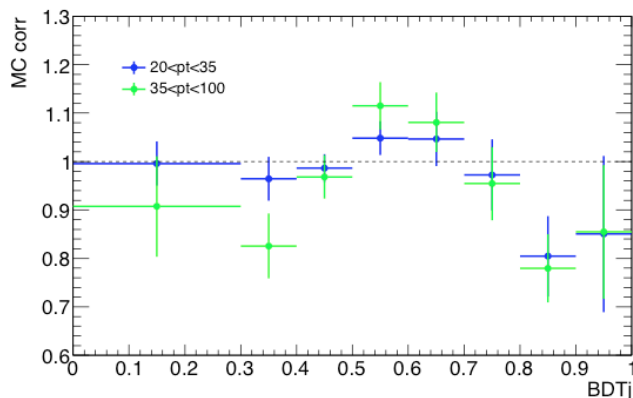
Figure 5.21: MC corrections applied to the τ_1 background templates and for events with ≥ 1 b-tags, for both $20 < E_T < 35$ GeV and $35 < E_T < 100$ GeV bins.

Fits to data

The next step in the application of the method, consists on applying the fitting method to the ATLAS data: by this way it is possible to extract the $t\bar{t} \rightarrow \tau + \ell$ signal. Figure 5.24 shows the final values using these combined templates, also displayed in table 5.13. Fitting results shows a sensible χ^2/ndf around unity, demonstrating that the method is acceptable.
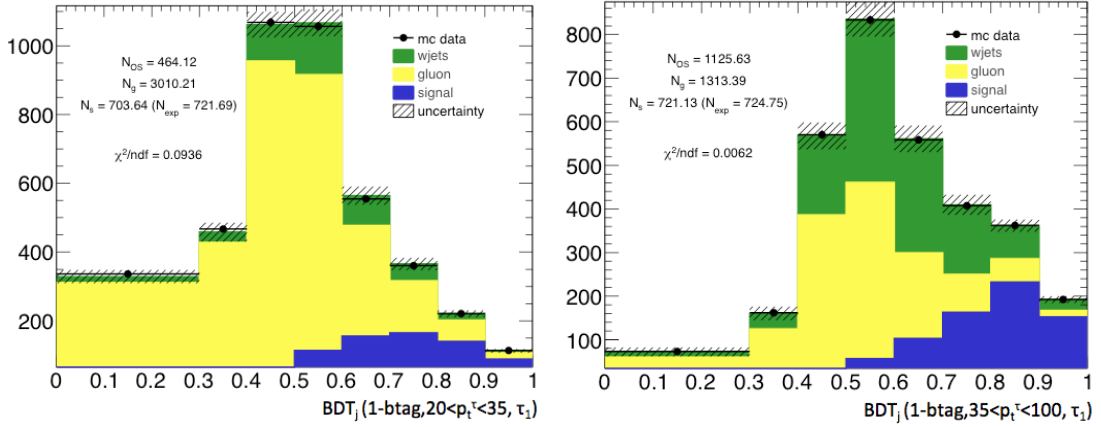
Figure 5.22: MC fit results using corrected background templates for τ_1 and events with ≥ 1 b-tags. On the left for $20 < E_T < 35$ GeV bin and on the right for $35 < E_T < 100$ GeV bin.
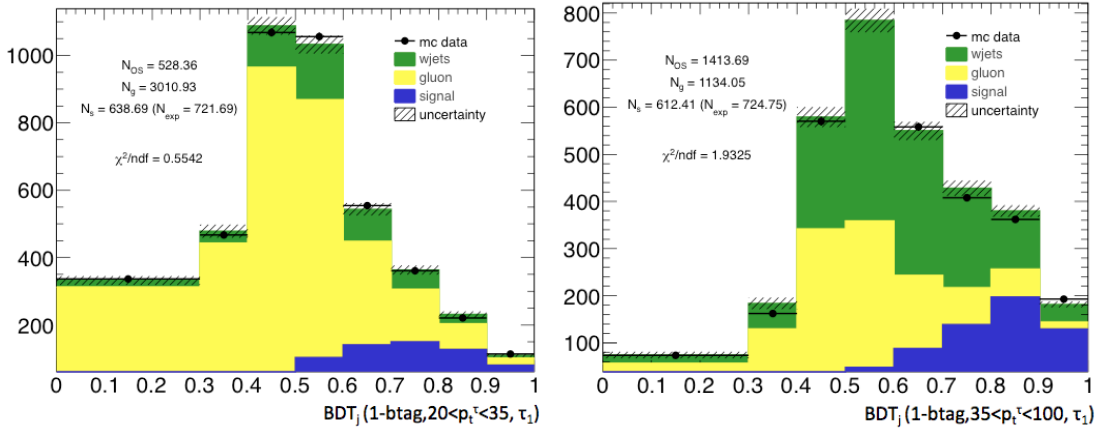
Figure 5.23: MC fit results without corrections for τ_1 and events with ≥ 1 b-tags. On the left for $20 < E_T < 35$ GeV bin and on the right for $35 < E_T < 100$ GeV bin. It can be observed the big difference in the value of χ^2/ndf with respect to the corrected ones.

The values of the expected signal (S_{MC}) are lower that the ones obtained in [69]. This difference could be due to the fact that the $\mu_{\text{truth}} \rightarrow \tau_{\text{cand}}$ background is not included, because at the moment of the analysis it was considered negligible as it was in previous $2\ fb^{-1}$ analysis. Later studies, show that they are not insignificant, and they are included in more precise measures showed in the mentioned note [69].
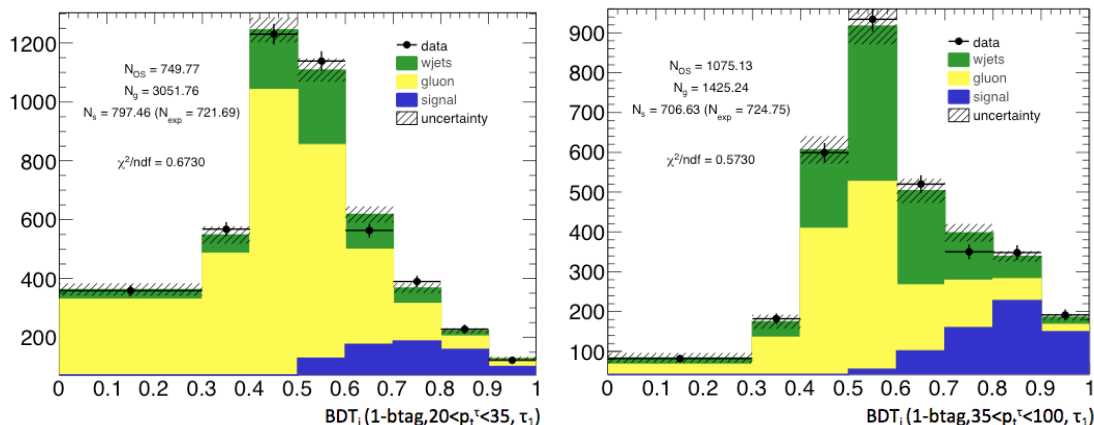
Figure 5.24: Fitting results to BDT_j data distribution using the corrected background and signal templates. Values of χ^2/ndf are showed for each fit.

Table 5.13: Fitting results to BDT_j data distributions. Numbers in the parentheses are χ^2/ndf.

Data Fits	S_{MC}	$S_{Fitted}^{AfterCorrections}$ (χ^2)
20<E_T<35GeV	721.7±6.5	797.5 ±72.1 (0.6730)
35<E_T<100GeV	724.8±6.4	706.6±52.3 (0.5730)

5.8 Cross section systematic uncertainties

The analysis of efficiencies and systematic uncertainties depends on the *prongs* of the τ's (1 or 3), the high and low multiplicity of primary vertices in the event, the p_T of the τ and the various ID's in combination with an electron veto. It is advisable to evaluate the uncertainties due to the cross section measurement, to assess the reliability of the measure.

Mainly systematic uncertainties are due to Monte Carlo, affecting to the fitting method due to small changes in the shape of the BDT_j, as the background shape uncertainty coming from signal subtraction, such as $Z + jets$ scale factor uncertainty, studied in section 5.3, and τ ID systematic uncertainties. These sources of systematic errors are taken into account in the cross-section evaluation by varying the signal contributions within the range of the systematic error for each contribution. The uncertainties in the cross section were derived using the samples variated in $\pm 1\sigma$ and performing the fitting method comparing the extracted cross section to the nominal samples in both e and μ channels together for 1-prong. The results

of the systematic uncertainties for the total cross sections extracted using fitting method will be shown in the next sections.

5.8.1   Systematic uncertainties description

To evaluate the systematic uncertainties, ATLAS uses common top group prescriptions and standard procedures to apply to the different experimental (lepton, jet, b-tagging) and theoretical sources considered. All qualified systematic are varied to produce the corresponding samples as *up-* and *down-* variations of the different systematic uncertainties needed for this analysis. The main sources of systematic uncertainties are described in the following.

Lepton uncertainties

The uncertainties related to lepton trigger, reconstruction and the selection efficiencies are estimated comparing the Monte Carlo $Z \to \ell\ell$ events that are selected with the same criteria as for the $t\bar{t}$ analysis.

Scale Factor uncertainties

Scale factors are applied to MC samples when calculating acceptances to account for any differences between predicted and observed efficiencies. The scale factors are evaluated comparing the measured efficiencies between simulated Z events in MC and the ones in data. Systematic uncertainties are evaluated by varying the selection of events used in the measurements of the efficiency. $Z \to \ell\ell$ events are selected by requiring two opposite signed leptons, with invariant mass inside the Z mass window ($80 < M_{\ell\ell} < 100$ GeV).

The modeling of the lepton momentum scale and resolution is studied using reconstructed invariant mass distributions of $Z \to \ell^+\ell^-$ candidates and used to adjust the simulation. More details about this study are described in the section 5.3.

Jet uncertainties

The jet energy scale (JES), jet energy resolution (JetRes), jet reconstruction efficiency (JetEff) and their uncertainties, are derived by combining information from LHC collision data and simulation, and from test-beam data [8]. The uncertainties of the JES dominate the ones related to jet, and it changes from 4-8%, depending on jet p_T and η. The jet reconstruction and identification, as the jet energy resolution measured in data and simulation are in good agreement. Systematic uncertainties are taken from the statistical uncertainties.

B-tagging uncertainties

The uncertainty in the efficiency of the b-tag algorithm has been estimated as an order of 6% for b-jet, based on *b-tagged* calibration studies using inclusive lepton final states [7].

The effect of all the previous variations on the final result is evaluated by varying each source of systematic uncertainty by $\pm 1\sigma$ in the $t\bar{t}$ MC sample, as it was indicated before. Consequently, the BDT signal template is variated and the cross section is recalculated by re-fitting the BDT_j signal distribution systematically variated.

Due that the $t\bar{t}$ production cross-section is obtained by taking the ratio of observed $t\bar{t}$ events to the expected number of $t\bar{t}$ events multiplied by the theoretical cross-section, the effect of the systematic variations has two origins: the variated expected number of $t\bar{t}$ events and the variated observed $t\bar{t}$ events. The first one is obtained from the integral of the BDT signal template with the lepton background and the background from real taus originated from non-$t\bar{t}$ processes subtracted; it contains the main part of the systematic variation. The second one is obtained from the fit variating the BDT_j signal template which is negligible.

MC generator and PDF uncertainties

Systematics in signal acceptance, with contributions depending of the choice of the generator, the modeling of the Initial and Final State Radiation (ISR/FSR) and PDFs, affect the uncertainty in the kinematics distribution of $t\bar{t}$ MC.

The generator uncertainty is evaluated by comparing the MC@NLO and ALPGEN [93] predictions with those of POWHEG [95] interfaced to either HERWIG or PYTHIA, following the official recommendations.

The uncertainty due to ISR/FSR effects is evaluated using ALPGEN generator interfaced to the PYTHIA shower model, and by varying the parameters controlling ISR and FSR in a range consistent with experimental data [87].

The PDF uncertainty is evaluated using different sets of PDF [89–91].

The dominant uncertainties in this case, are the modeling of ISR/FSR. The effect of all the variations ISR/FSR and generator on the final result is evaluated by varying only the expected number of $t\bar{t}$ events. The measured number of $t\bar{t}$ events remains at the nominal value since the fits are not remade given that changing the generator and/or moving from *fullsim* samples to *Atlfast* 2 samples could modify the background model.

τ identification uncertainties

The uncertainties related to τ ID are derived from the template fit to the BDT_j distribution from $Z \to \tau\tau$ data sample selected with the same requirement as it was used in the determination of the Z scale factors, described in section 5.3. It is also required two opposite signed isolated leptons, trigger and the reconstructed Z mass in the window [80, 100] GeV. In addition less than 2 jets are required and $M_T(\mu, E_T^{\mathrm{miss}}) < 20$ GeV, to remove $W + jets$ events [10].

The background templates are the $W+1$ jet OS and the gluon template used in the fit to the $t\bar{t}$ data sample. The signal template is the BDT_j distribution from $Z \to \tau^+\tau^-$ MC events. The total uncertainty includes the statistical uncertainty of the data samples, the one in the Z/γ^* cross section measured by ATLAS [92] (excluding luminosity uncertainty) and in the jet energy scale. It also includes the uncertainty on the number of misidentified electrons ($< 0.5\%$), determined from $Z \to e^+e^-$ data).

5.8.2   Summary of the systematic uncertainty

The fits results for the relevant systematic uncertainties are summarized in table 5.14. Table 5.15, shows the systematic uncertainties for cross section measurement using the fitting method. The dominant contribution comes from b-*tag* scale factor uncertainty. For MC generator systematics, only the signal expected is changed in the cross-section formula. The variation is exclusively from the signal expected, that is derived from the acceptance. The recommendations for systematic calculation from the Top ATLAS group are also followed [97].

5.9   Estimation of $\sigma_{t\bar{t}}$ with $l+\tau$ in the final state

The cross-section is calculated using the number of observed signal events, measured by the fit to the BDT_j shape in the signal region using the definition:

$$\sigma_{t\bar{t}} = \frac{S_{measured}}{A \cdot \varepsilon} \cdot \frac{1}{L}, \tag{5.13}$$

being $S_{measured}$ the measured signal, ε the object and trigger reconstruction efficiency, A is the signal acceptance and L is the integrated luminosity. The simulated signal model is:

$$S_{MC} = A\varepsilon L\sigma_{t\bar{t}(SM)}, \tag{5.14}$$

Table 5.14: Fitting results of relative systematic uncertainties for cross-section estimations for τ_1 and 1 b-*tag*, where δ Cross-Section is $100\times\frac{\sigma_{syst}-\sigma_{nominal}}{\sigma_{nominal}}$.

	$N_{sig.}$Expected	$N_{sig.}$Measured	Cross-Section (pb)	δ Cross-Section
Nominal	1272.6±7.6	1323.0±71.1	184.0±9.95	0
BSF up	1332.8±7.9	1321.3±62.0	175.5±8.30	-4.65
BSF down	1206.9±7.4	1324.2±101.6	194.2±14.95	5.53
JES up	1310.8±7.7	1321.8±61.1	178.5±8.31	-3.01
JES down	1228.0±7.5	1325.6±94.3	191.1±13.64	3.83
JetEff	1272.4± 7.6	1322.9±71.1	184.0±9.95	-0.00
JetRes	1256.6± 7.5	1323.1±86.7	186.4±12.26	0.64
MCNLO	1271.5±7.97	1329.3±57.99	185.0±8.16	
alppythia hi	1396.0±7.57	1329.3±57.99	168.5±8.16	
alppythia lo	1216.4±6.74	1329.3±57.99	193.4±8.16	
alpjimmy	1347.0±16.17	1329.3±57.99	174.7±8.18	
fPowHegJimmy	1358.1±7.84	1329.3±57.99	173.2±8.16	
fPowHegPythia	1248.2±7.53	1329.3±57.99	188.5±8.16	

Table 5.15: Absolute systematic uncertainties in pb, for the cross-section estimation for τ_1 and 1 b-*tag*. The first column shows the source of systematic uncertainty. The τ ID uncertainty includes electrons misidentified as τ leptons.

Source	Uncertainties (pb)
τ_1 Statistical	10.0
μ (ID/Trigger)	0.2
e (ID/Trigger)	0.2
Jet E scale	-5.2 / $+5.9$
Jet E res.	1.3
ISR/FSR	12.5
Generator	10.3
$b-$tag	-7.3 / $+9.4$
τ_1 ID	8.4
total syst. τ_1	$-19/+20$
total	10 (stat) $^{+20}_{-19}$ (syst)

where S_{MC} is the number of signal events expected from simulation, and $\sigma_{t\bar{t}(SM)}$ is the standard model $t\bar{t}$ cross section by which the simulation was normalized (177.3 pb). Then, the resulted cross section can be calculated by

$$\sigma_{t\bar{t}} = \sigma_{t\bar{t}(SM)} \cdot \frac{S_{measured}}{S_{MC}} \qquad (5.15)$$

The values of the measured and expected signals, after subtracting the contributions of real taus from other processes and of the electrons, are shown in table 5.16, for τ_1 and 1 b-tag case.

Table 5.16: Number of events resulted from the fit.

	τ_1, 1b-tag
$S_{measured}$	$1.32 \times 10^3 \pm 71.1$
S_{MC}	$1.27 \times 10^3 \pm 7.6$

Considering the uncertainty on the measured integrated luminosity to be 1.8% [55], the estimated cross-section, obtained for τ_1 and 1 b-*tag*, for both e and μ channels together is:

$$\sigma_{t\bar{t}} = 184 \pm 10(\text{stat.}) \pm {}^{+20}_{-19}(\text{syst.}) \pm 3.3(\text{lumi.})\text{pb}$$

This result agrees with the one expected from the standard model (177.3 pb) and with the previous measurements performed with 2 fb^{-1} [68], which is $\sigma_{t\bar{t}} = 186 \pm 13(\text{stat.}) \pm {}^{+20}_{-19}$ (syst.) ± 7 (lumi.) pb. More results including τ_1, τ_3 and 2 b-*tag* studies with new improvements developed, can be found in [64] with 2 fb^{-1} samples, and in [69] for 4.73 fb^{-1} samples.

Chapter 6

Summary and Conclusions

This thesis includes studies performed with the ATLAS experiment. It is divided in two parts: one is related to the Tile Calorimeter commissioning and the other shows $t\bar{t}$ studies with a τ in the final state, including a measure of the top-quark pair cross-section.

The first part includes:

- The description and results of data quality tests carried out before the start-up of the LHC collisions. The TileCal front-end electronic has been tested with physic and calibration data, both online and offline. The large number of detailed histograms produced by the monitoring system of the detector, allowed to check the correct behavior of TileCal, ensuring the Data Quality needed for operations. The monitoring system allows to check the correct performance of the detector in a very short time (online monitoring) and in a longer scale-time using different analysis tools (offline monitoring). The data quality tools tested worked well. They were essential to ensure efficient data taking and processing, which is imperative during commissioning and operational periods.

- The description of TileMuID, an algorithm based on TileCal implemented in the Muon Second Level trigger that allows to tag low p_T muons, and results from studies performed using this algorithm. The obtained results were published in an ATLAS note [27], verifying that the system was fully operative. A higher statistics of LHC collision data would be necessary to fully commission the muon trigger system, but the limited statistics available at that moment did not allow for any quantitative estimation of trigger efficiencies and resolutions at the different trigger levels. Latter periods of data taking contributed to a better understanding of the detector behavior.

The second part includes:

- The measurement of the probability for hadronic jets to be mis-identified as hadronically decaying τ lepton. This study uses two tau identification methods (BDT and LLH) with 2011 data, validating the use of the BDT algorithm for the rest of the analysis. The samples used are light quark jets which have a higher probability of faking a τ than all the other types of jets. The mis-identification probabilities for 1-*prong* case (3-*prong* case), ranged from 0.01% and 0.15% (0.005%-0.05%) for BDT identification algorithm, from 0.02% to 0.25% (0.005%-0.16%) for LLH, and from 0.02% to 0.13% (0.005%-0.04%) depending of the number of vertices. The probabilities depend on the chosen τ identification algorithm, the number of prongs of the τ candidate, its p_T, the origin of the reconstructed hadronic jets as a τ candidate, and the number of primary vertices found in the events. The *tight* selection was the most accurate, against the *loose* and the *medium* selections. BDT based τ-algorithm was the chosen one for the rest of the analysis presented in this work.

- The $Z + jets$ scale factors calculation required for $t\bar{t}$ cross-section estimation. These numbers add a parametrization by Zp_T, which is necessary for the application to the $Z \rightarrow \tau\tau$ samples. Studies checking the η dependence and measuring the uncertainty of the signal using the BDT τ identification variable, have been performed. Results show that distributions on Zp_T depend on the jet multiplicity, and they are independent on the kind of lepton or η value. This study takes part of the ATLAS note [63].

- The measurement of the $t\bar{t}$ production cross section with a lepton (electron or muon) and a hadronically decaying τ-lepton in the final state, using 4.73 fb^{-1} *proton-proton* collision data at a center of mass energy $\sqrt{7}$ TeV. A multivariate technique based on Boosted Decision Trees (BDT) that separate the signal from quark and gluon-jet backgrounds, and from which the ATLAS τ identification depends on, have been studied. The method obtains the BDT_j distribution from an identification score, for misidentified gluon jets and from another, mainly composed by OS light-quark jets plus a small gluon jets mixture from the W+jets, which is fitted to the signal region using a signal and a background template for τ lepton identification. The resulting cross section for τ_1 and 1 b-*tag* selection is,

$$\sigma_{t\bar{t}} = 184 \pm 10(\text{stat.}) \pm {}^{+20}_{-19}(\text{syst.}) \pm 3.3(\text{lumi.})\text{pb}$$

which is in good agreement with the one expected from the standard model and with the previous measurement performed to 2 fb^{-1}. The method im-

proves the previous one reducing the statistical uncertainty and building a better background model. BDT fits can be used in top quark physics to perform precise cross-section measurements in higher ranges of energies, which can help to determine properties of the top quark in more detail. This study takes part of the ATLAS note [69].

Chapter 7

Resumen

7.1 Introducción

La presente tesis se ha desarrollado en el marco del experimento ATLAS, un detector de propósito general y que al igual que los detectores CMS, ALICE y LHCb, se halla ubicado en el Gran Colisionador de Hadrones (LHC), en el Centro Europeo para la Investigación Nuclear (CERN). El trabajo que aquí se presenta, se compone de varias partes diferenciadas, y comienza con una descripción básica de la física que se estudia en el LHC centrada en el quark top, cuya producción de pares es uno de los procesos dominates en las interacciones protón-protón, después de los jets de QCD y la producción de los bosones W y Z. A continuación se describen las partes fundamentales del acelerador LHC y el detector ATLAS. Lo siguiente se dedica al detector TileCal y el algoritmo TileMuID, un algoritmo de nivel-2 del Trigger de Muones basado en TileCal, con estudios realizados durante la fase de puesta en marcha de ATLAS, mediante el análisis de datos de muones cósmicos. Por último, se presentan estudios relacionados con la física del quark top: cálculo de los factores de escala del Z, cálculo de probabilidad de identificación errónea de leptones τ provenientes de jets hadrónicos en el canal $\gamma+jets$ y una medida de la sección eficaz del par $t\bar{t}$, con un leptón y un τ desintegrado hadrónicamente en el estado final. Este análisis se ha realizado con datos a 4.73 fb^{-1} tomados por ATLAS en 2011.

7.2 Motivaciones físicas

El Modelo Estándar de las partículas (SM) es una teoría cuántica de campos unificada, consistente con la mecánica cuántica y la relatividad especial, lo cual permite la comprensión de la estructura de las partículas elementales y describe las interacciones fundamentales entre ellas. Por el momento, es la teoría que mejor describe

121

las observaciones experimentales y cuya validez ha sido probada a muy altas ener-
gías en multitud de experimentos con aceleradores de partículas. En el marco del
SM, se puede describir la interacción de los fermiones fundamentales de spin $1/2$,
leptones y quarks. Dichas interacciones están mediadas por bosones gauge de spin
1. Los bosones son una manifestación del grupo de simetría de la teoría, el cual para
el SM es $SU(3)_C \otimes SU(2)_L \otimes U(1)_Y$ donde C representa "Color", L denota "Isos-
pin", e Y hace referencia a la "Hipercarga". El grupo de simetría $SU(2)_L \otimes U(1)_Y$
describe la denominada Interacción Electrodébil (*Quantum Electrodynamics* ó
QED), cuya rotura espontánea se produce a través de la existencia de un campo
de Higgs de valor esperado distinto de cero. Este mecanismo conduce a la apari-
ción de los bosones vectoriales masivos, el $W^{\pm}$ ($M_W \sim 80$ GeV) y el Z ($M_Z \sim 91$
GeV), mediadores de la interacción débil, mientras que el fotón (γ) responsable de
la interacción electromagnética permanece sin masa.

Los quarks son tripletes del grupo gauge SU(3), y por tanto son capaces de
transportar una carga adicional denominada "Color", la cual es la responsable de
su participación en las interacciones fuertes (*Quantum Chromodynamics* ó QCD).
Un conjunto de ocho gluones vectoriales son los mediadores de esta interacción,
transportando dicha carga de color e interactuando unos con otros, pudiendo lle-
gar a producir pares virtuales quark-antiquark. Esto implica que la constante de
acoplamiento de QCD es pequeña en el caso de grandes transferencias de momento
y muy grande cuando se trata de procesos suaves, lo que explicaría el confinamien-
to de los quarks dentro de los hadrones, cuya carga de color es cero como en el
caso del protón y el neutrón. El intento de liberar un quark produciría un cho-
rro de hadrones a través de la producción de pares quark-antiquark y gluones de
bremsstrahlung. Sin embargo, el SM no explica de forma completa y satisfactoria
la totalidad de las interacciones fundamentales, ya que no incluye la gravedad, la
cuarta interacción fundamental conocida. El 4 de julio de 2012, el CERN anunció
la observación de una nueva partícula "consistente con el bosón de Higgs". El 14
de marzo de 2013, con el doble de estadística, se confirmó que la nueva partícula
es vista cada vez más como el bosón de Higgs. Sin embargo, subyace la cuestión
de si esta partícula es el bosón de Higgs del SM o tal vez el más ligero de varios
bosones predichos en algunas teorías que van más allá del Modelo Estándar. Ade-
más, dados los resultados experimentales actuales, el SM no se considera como la
teoría final.

El quark top es la partícula elemental más pesada con 172,5 GeV y junto con el
quark b constituye la tercera generación de los dobletes de quark. Debido a su gran
masa y a su desintegración, constituye una prueba importante para la búsqueda
de nueva física en el marco del SM. En el experimento ATLAS, uno de los estudios
concernientes a la producción de pares del quark top, es la medida de su sección
eficaz. Esta medida será importante para el estudio de las propiedades intrínsecas

del quark y sus interacciones, y es interesante para la búsqueda de nuevos mecanismos de producción no relacionados con el SM. La medida de la sección eficaz, puede realizarse mediante su desintegración en un único electrón o muón con jets asociados, o en dos muones o electrones con jets. El proceso de desintegración se describe por la teoría electrodébil una vez que se genera el quark top. Se descompone principalmente en un W y un quark-b, con una relación de desintegración próxima al 100 %. El bosón W se desintegra en un par quark-antiquark con una probabilidad de cerca de 2/3, o en un par leptón-neutrino cargado con una probabilidad de 1/3. Los pares $t\bar{t}$ suelen clasificarse de acuerdo con los productos de desintegración de los dos bosones W. Los estados finales que incluyen un par $t\bar{t}$ se clasifican de acuerdo con la desintegración del bosón W, donde el canal en el que todo son jets representa alrededor del 44 % de las desintegraciones, el canal leptón más jets cerca del 45 % y el canal dileptónico alrededor del 10 % de las desintegraciones. Sucesos en los que el estado final contiene electrones o muones, son de particular interés, ya que proporcionan claras señales de *triggers* y señas de diferentes eventos.

La partícula τ es un leptón que juega un papel importante en el programa de física del LHC, pertenece a la tercera gneración de leptones y su papel es equivalente al del electrón y el muón, pertenecientes a la primera y segunda generación respectivamente. Lo que definitivamente distingue al τ de electrones y muones es su elevada masa ($m_\tau = 1.777$ MeV), que le permite desintegrarse a través de canales hadrónicos y no solo a leptones. El leptón τ es útil para la búsqueda de nueva física, como el bosón de Higgs, búsquedas de SUSY, y en las mediciones electrodébiles.

7.3   LHC y ATLAS

7.3.1   LHC

El Gran Colisionador de Hadrones (LHC), es actualmente el mayor acelerador de partículas del mundo, con la energía más alta jamás producida. Comenzó su funcionamiento con colisiones protón-protón en noviembre de 2009. Durante el año 2011 se hizo funcionar con $\sqrt{s} = 7$ TeV. Debido a su gran energía en el centro de masas, el LHC se considera una fábrica de quarks-t, lo que permite evaluar la sección eficaz $t\bar{t}$ con gran precisión. Está instalado en los 27 km de longitud del túnel del antiguo Gran Colisionador Electrón-Positrón (LEP), situado en la frontera entre Suiza y Francia, junto a la ciudad de Ginebra, y a una profundidad de entre 50 y 175 m. El diseño del acelerador permitirá colisionar protones contra protones a una energía alrededor de 14 TeV en su centro de masas, con una luminosidad de diseño de 10^{34} cm^{-2} s^{-1}. Los paquetes de protones circulan

por el anillo del acelerador en direcciones opuestas con velocidades cercanas a la de la luz. En los puntos de colisión se ubican los cuatro grandes detectores del LHC: ATLAS y CMS, que son dos experimentos de propósitio general; ALICE, que estudia el plasma de quarks y gluones a partir de colisiones de iones pesados; y LHCb, dedicado a la física del quark-b y que tiene entre sus objetivos explicar la asimetría entre materia y antimateria.

7.3.2   ATLAS

ATLAS, A Toroidal LHC ApparatuS, es un experimento de propósito general para el Gran Colisionador de Hadrones (LHC). El principal objetivo del experimento ATLAS es el estudio de la física a la escala del TeV, con especial interés en la física del bosón de Higgs y la rotura espontánea de la simetría electrodébil. Es el mayor experimento del LHC. Las colisiones de protones en el centro del detector, donde la densidad de energía es similar a la energía de colisión de partículas en el Universo temprano, a menos de una mil millonésima de segundo después del Big Bang, revelarán procesos fundamentales de las partículas.

La identificación de partículas en el detector, se basa en la carga de la partícula y el poder de frenado en el material. Básicamente, los electrones y fotones son detectados en el calorímetro electromagnético, mientras que protones y neutrones, depositan su energía en el calorímetro de hadrones. Los muones atraviesan el detector, siendo registrados en el espectrómetro de muones. La presencia de neutrinos no se puede detectar directamente, pero es posible comprobar su contribución a través del desequilibrio de la cantidad de movimiento en el plano transversal. Los subdetectores principales que se pueden observar en la figura 3.5, se dividen en:

- **Detector Interno**: Además de reconstruir los vértices secundarios, reconstruye trazas de partículas cargadas y mide su momento transversal (p_T).

- **Sistema de Calorimetría**: Es el responsable de la reconstrucción de jets. El calorímetro electromagnético detecta electrones y fotones, mientras que el calorímetro de hadrones detecta jets de hadrones.

- **Espectrómetro de muones**: Reconstruye los muones y permite llevar a cabo una medida de su p_T.

- **Sistema de imanes**: Compuesto por un núcleo central y un sistema exterior de imanes toroidales con núcleo de aire, este último genera el campo magnético para el Espectrómetro de Muones.

El calorímetro hadrónico de tejas, TileCal, al que corresponden parte de los estudios presentados en este trabajo, es uno de los componentes del sistema de calorimetría de ATLAS.

7.4 Estudios con Muones en TileCal y en el Nivel 2 de Trigger

En esta sección se presentan estudios que contribuyeron a la puesta en marcha del sub-detector Tile Calorimeter (TileCal) y al sistema de Trigger de Muones de Nivel 2, en el detector ATLAS. Para la reconstrucción de la información en ATLAS se integró el uso de software offline para recibir información inmediata sobre los datos.

En el periodo de puesta a punto, se incluyeron una serie de tareas dentro del marco del proyecto *Data Quality Assessment* que utilizó software offline para reconstruir y analizar todos los datos tomados. Se demonstró un correcto funcionamiento que garantizó la calidad de los datos como una parte fundamental para la eficacia de toma y procesamiento de los mismos. El objetivo era identificar posibles fallos en los componentes electrónicos o problemas durante la operación del detector, para asegurar el correcto funcionamiento de los sistemas.

Los estudios referentes al Trigger de Muones, se realizaron con TileMuId, un algoritmo basado en TileCal implementado en el Nivel 2 de trigger.

7.4.1 TileCal

TileCal es uno de los sub-detectores de ATLAS, capaz de medir la energía de los hadrones. Es un calorímetro de muestreo que utiliza una estructura de placas de acero como material pasivo, y tejas centelleadoras de diversas dimensiones como material activo. Consiste en un barril central de 5,6 m de largo (LB) y dos barriles extendidos (EB) de 2,9 m de largo cada uno. TileCal se encuentra en la región η = 1.7 y se caracteriza por tener una buena resolución energética en todo el rango cubierto de ϕ, así como una excelente uniformidad en las direcciones ϕ y η. La luz de centelleo, generada en las tejas como consecuencia del paso de las partículas ionizantes, es leída por fibras ópticas (WLS) acopladas a las tejas en la dirección radial y transmitida, mediante mazos de fibras, a los fotomultiplicadores situados en el interior de la viga que sustenta los módulos del calorímetro. Dentro de la electrónica asociada, el elemento principal es el sistema de lectura. Está compuesto por 32 tarjetas Read-Out Drivers (ROD), basadas en tableros 9U VME64x equipados con un máximo de cuatro unidades de procesamiento. Los RODs se colocan en 4 *crates* correspondientes a las 4 particiones TileCal para la adquisición de datos. Cada partición es gestionada por una *crate* de TTC, equipada con módulos TTC estándares para los experimentos del LHC.

7.4.2 Evaluación de la Calidad de Datos TileCal

Durante la instalación y primeras fases del calorímetro TileCal, debido al gran número de canales electrónicos y la alta cantidad de datos tomados para verificar el correcto comportamiento de los sistemas de hardware y software, hizo falta una profunda puesta en marcha, desarrollando diferentes procesos de evaluación. Los primeros test con datos, se realizaron con muones cósmicos a través de todas las fases de la adquisición y el análisis (monitoraje, reconstrucción, validación de señales de datos y procesamiento de calibración). Las tareas para comprobar los datos adquiridos se basaban en el rendimiento del hardware y permitieron identificar problemas en el funcionamiento del detector como la conveniencia del uso de las herramientas de supervisión cuando los datos se toman de manera eficiente, o el uso de una especial calibración para investigar el estado de TileCal. El procedimiento se llevaba a cabo en tres pasos diferentes: la decodificación de los datos en bruto y preparación de cantidades reconstruidas, llenado de histogramas con las cantidades reconstruidas, y por último los procesos que utilizan histogramas para producir señales de calidad. Las herramientas desarrolladas iban desde las pruebas de verificación del hardware y el monitoreo en línea, hasta la reconstrucción fuera de línea, lo que permitió un análisis rápido y parcialmente automatizado de los resultados, mediante evaluación de histogramas a partir de tomas de datos al azar y de muónes cósmicos, así como los niveles de ruido, el número de eventos que superaban un umbral determinado, la reconstrucción del clúster y la reconstrucción de muones. Las pruebas realizadas en este trabajo comienzan comprobando los bloques de datos tomados por ATLAS y seleccionando los que tienen suficiente estadística. La figura 4.11, muestra un alto nivel de ruido en $\eta \sim 0{,}75$ y $\phi \sim 0.1$ (izquierda). Observando la representación correspondiente a la numeración del hardware (derecha), se aprecia cierta actividad en el módulo LBC35. Este histograma se realizó a partir de una toma de datos al azar, llamada *Random Muon Stream* (RNMD) que usa un trigger aleatorio, donde se espera que no tenga canales problemáticos si todo funciona bien. La figura 4.14 corresponde a datos tomados con muónes cósmicos. Se pueden observar los muones que entran en el TileCal, mostrando niveles de ocupación en coordenadas η-ϕ. La figura 4.16, representa la distribución de la pérdida de energía de los muones reconstruidos. Se observa un pico dE/dx cerca de 2 MeV/mm. Los muones tienen un comportamiento de Partículas de Mínima Ionización (MIP) que muestran una energía promedio y una longitud de onda característica.

7.4.3 Estudios con el Trigger de Muones a nivel 2

La siguiente sección muestra resultados del análisis realizado con el algoritmo TileMuID, utilizando datos cósmicos recogidos en otoño de 2009. Como antes se

ha mencionado, TileMuID sigue una estrategia para etiquetar muones de bajo momento transverso a Nivel 2 del Trigger en TileCal. Los resultados presentados en este trabajo formaron parte de una nota ATLAS [27], junto con todos los algoritmos del trigger de muones. El análisis fue realizado con datos tomados en otoño de 2009 a $\sqrt{s} = 900$ GeV.

Trigger de muones y TileMuID

Al igual que la estructura general del trigger de ATLAS, el sistema de trigger de muones tiene varios niveles diferentes: el nivel 1 basado en hardware (L1) y otro nivel basado en software (HLT) que comprende el Nivel 2 (L2) y el filtro de eventos (EF). L1, usa electrónica para rechazar la mayoría de fondos de colisiones a partir de la información proveniente principalmente de los calorímetros y de los detectores de muones. El HLT se inicia a partir de una región de interés (ROI), definida por el primer nivel del trigger. Para la reconstrucción se utilizan algoritmos de extracción que solicitan datos del detector asociados con las RoIs para identificar muones. TileCal tiene la posibilidad de etiquetar muones de bajo p_T en el segundo nivel del trigger de ATLAS. La identificación se realizaba mediante su momento transverso en el rango de la coordenada η. El algoritmo implementado para realizar esta tarea denominado $TrigMuTile$ ó $TileMuId$ [32], además de aportar redundancia y robustez al HLT de muones, contribuyó a optimizar los criterios de identificación para la toma de datos con colisiones. El algoritmo se basa en la deposición típica de energía (MIP) en el calorímetro y en su segmentación geométrica. Para definir un depósito MIP, se aplica el requisito de que la energía de la celda esté comprendida entre dos umbrales, tal como se indica en la ecuación 4.1. El umbral de energía inferior descarta las fluctuaciones de ruido o pile-up y el superior se utiliza para descartar las colas hadrónicas. Existen varias versiones del algoritmo TileMuId, siendo la versión denominada $TrigTileLookForMuAlg$ implementada en el marco de Athena, la que se utilizó en el presente trabajo. Este algoritmo accede a los objetos TileCell alrededor de las RoIs del nivel 1, donde TileMuId se aplica. La salida proporciona la información de los muones etiquetados. La figura 4.23 muestra la distribución del ángulo azimutal en TileCal, ϕ, obtenida con el algoritmo. Se observa la forma típica de arriba hacia abajo, como es de esperar en muones cósmicos que atraviesan el calorímetro. La distribución muestra una asimetría debido a que se identifican más muones en la parte superior del cilindro que en la parte inferior. Esto podría ser debido no sólo a la falta de estadística, sino a que el espectrómetro de muones da valores RoIs del nivel 1 más grandes en la parte superior. La figura 7.1 muestra la energía depositada en TileCal por muones cósmicos. La distribución muestra una cola, debido a que los rayos cósmicos de muones depositan una gran cantidad de su energía en una sola celda. Se aplicó un corte en la energía de la celda >300 MeV que permitió reducir los
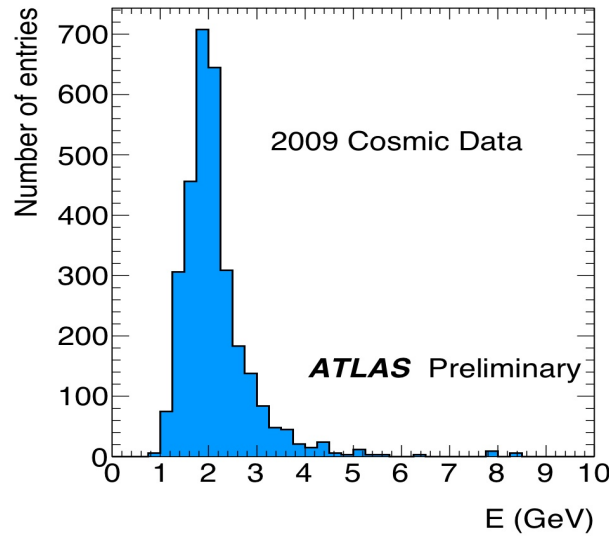
Figura 7.1: Distribución de energía en TileCal de rayos cósmicos de muones en el nivel L2. Los datos fueron recogidos en otoño de 2009.

efectos del ruido electrónico. Se observa un pico en la energía depositada alrededor de 2 GeV, compatible con el comportamiento de las partículas con ionización al mínimo en TileCal y que concuerda con lo obtenido mediante simulaciones MC.

7.5 Estudios $t\bar{t}$ con τ en el estado final

La segunda parte de este trabajo, está dedicada a la medida de la sección eficaz ($\sigma_{t\bar{t}}$) de producción de pares del quark top ($t\bar{t}$) con un leptón, electrón ó muón, en el estado final y un leptón τ desintegrándose hadrónicamente, usando datos de colisiones protón-protón a 4.73 fb^{-1} y una energía en centro de masas de $\sqrt{7}$ TeV, llevados a cabo con el experimento ATLAS. El análisis incluye el cálculo de los factores de escala de las muestras de bosones Z y el estudio de identificación errónea de leptones τ's en el canal $\gamma +$ jets ($\tau \; fake \; rates$) de aquellos eventos que por su topología son considerados candidatos. En este estudio se usan dos métodos de identificación del tau (BDT y LLH), que permite validar el uso del algoritmo BDT con datos de 2011 y es elegido para el resto del análisis. Los criterios de selección y la definición de objetos usados en este análisis se describen con detalle en la sección 5.1.

7.5.1 Estudios τ_{ID}: estimación de τ-*fake rates* con muestras $\gamma + jets$

En este trabajo se incluye un estudio de la falsa identificación de jets como taus (*fake rate*). La correcta identificación de taus reales es importante para reducir el fondo donde eventos $t\bar{t}$ se han identificado pasando determinados cortes de selección, pero la identificación del τ es falsa. Los *light-quarks* tienen una mayor probabilidad de falsear un τ que otro tipo de jets, debido a que tienen una baja multiplicidad de trazas. Este estudio evaluado en el canal $\gamma + jets$ es útil para la definición del modelo de fondo y poder estimar mejor la contaminación en la región de señal, y permite evaluar el algoritmo de identificación del tau más adecuando para datos correspondientes al periodo de 2011. Se han utilizado diferentes selecciones de τ (*loose*, *medium* y *tight*), que corresponden a diferentes eficiencias de señal con el fin de comparar los diferentes resultados. La *fake rate* se define mediante la ecuación:

$$f_{ID} = \frac{\text{Número de jets identificados como leptones } \tau}{\text{Núnero de jets reconstruídos como leptones } \tau} \tag{7.1}$$

Preselección y selección de eventos para la estimación de τ-*fake rates*

La selección de eventos comienza con la inclusión de la denominada *Good Run List* (GRL) para taus [56], seguida por la corrección del calorímetro Liquid Argon. Se requiere al menos un vértice con 4 trazas, y se usa al menos uno de los niveles de trigger del Event Filter con umbrales de energía (E_T) de γ en 20, 40 y 60 GeV, incluyendo la identificación del fotón *loose* para seleccionar la topología $\gamma + jet$. También se requiere una corrección que rechaza γ's que tienen más de 6 GeV de energía fuera del la región de aislamiento, así como que no haya jets con $p_T < 20$ GeV y energía < 0, que exista al menos un buen jet y al menos un buen γ. La siguiente condición demanda un ángulo $D\phi > 2.94$ entre el primer fotón y el primer jet que cumplan las condiciones requeridas. La distancia entre el candidato a τ y el jet principal debe de ser menor que 0.2. Finalmente se requiere que el p_T del segundo jet sea menor que el 10 % del p_T del primer fotón. La selección de eventos para γ, *jets* y τ se describe en la sección 5.1.6. El código de análisis desarrollado para este trabajo se puede encontrar en SVN [58].

Resultados según la selección de eventos y los criterios de identificación en el estudio de *fake rates*

La tabla 5.1 muestra el número de eventos obtenido después de cada corte, de acuerdo con las selecciones descritas en el apartado anterior, y el cálculo de la

eficiencia de los eventos obtenidos. Los resultados de la evaluación de la *fake rate* en función del p_T del leptón τ según las selecciones BDT, LLH y el número de vértices para el caso de 1-*prong*, se muestran en las siguientes figuras. En la figura 7.2(a), los resultados varían de 0.01 % a 0.15 %, siendo la selección *tight* la más precisa. En la figura 7.2(b) los valores obtenidos son mayores que para el caso BDT. No está incluido el veto al electrón como en el caso anterior, lo que puede influir en el resultado. Los valores obtenidos varían de 0.02 % a 0.25 %. Finalmente, en la figura 7.2(c) que muestra el número de vértices menor que 2, 4, 6, 8 y 12 en función del p_T del τ, se observan valores comprendidos entre 0.02 % y 0.13 % para el caso de 1-*prong*. Con este estudio se puede concluir que las probabilidades resultantes dependen del algoritmo escogido, del número de trazas del candidato a τ, su p_T, el origen de los jets hadrónicos reconstruídos como candidatos a τ, y el número de vértices encontrados en el evento. La selección *tight* es la más precisa, y el algoritmo basado en BDT el más eficiente, lo que es tenido en cuenta para el resto del análisis presentado en este trabajo.

7.5.2 Cálculo de los factores de escala Z+jets

La producción MC de Z+jets obtenida por un simulador, no reproduce bien la multiplicidad de jets observados en datos reales, por lo que se necesitan factores de escala para conseguir un mayor acuerdo entre datos y MC. En este trabajo se calculan los factores de escala del Z, comparando selecciones de muestras generadas por MC con datos reales, en función de la multiplicidad de los jets. La selección comienza obteniendo eventos Z limpios, para ello se utilizan los canales ee y $\mu\mu$. Se requieren dos leptones aislados (e ó μ) con signo opuesto, la activación de un trigger individual del leptón (e ó μ), que la masa del Z reconstruída se encuentre en el rango $80 < M_Z < 100$ GeV y que la banda lateral en la que los eventos tengan una masa en los intervalos $60 < M_Z < 70$ GeV ó $110 < M_Z < 120$ GeV, sea sustraída como fondo. Además, los elementos que pasan esta selección se clasifican según el número de jets con $p_T > 25$ GeV para derivar los factores de corrección dependientes de la multiplicidad de jets. Los electrones, muones y jets han de pasar la selección de objetos descrita en la sección 5.1.

Factores de escala Z en función de la multiplicidad de jets y de bines de $\mathbf{p}_T$

El momento del leptón y su resolución, así como las incertidumbres, son evaluadas utilizando datos simulados MC, permitiendo reproducir la masa invariante del sistema diléptonico. La figura 5.9, muestra las distribuciones M_Z en bines de multiplicidad del jet para $Z \to ll$, donde $ll = ee, \mu\mu$. El pico de masa reconstruído a partir de los dos leptones es previo al requerimiento $80 < M_Z < 100$ GeV y a la

(a)

(b)

(c)
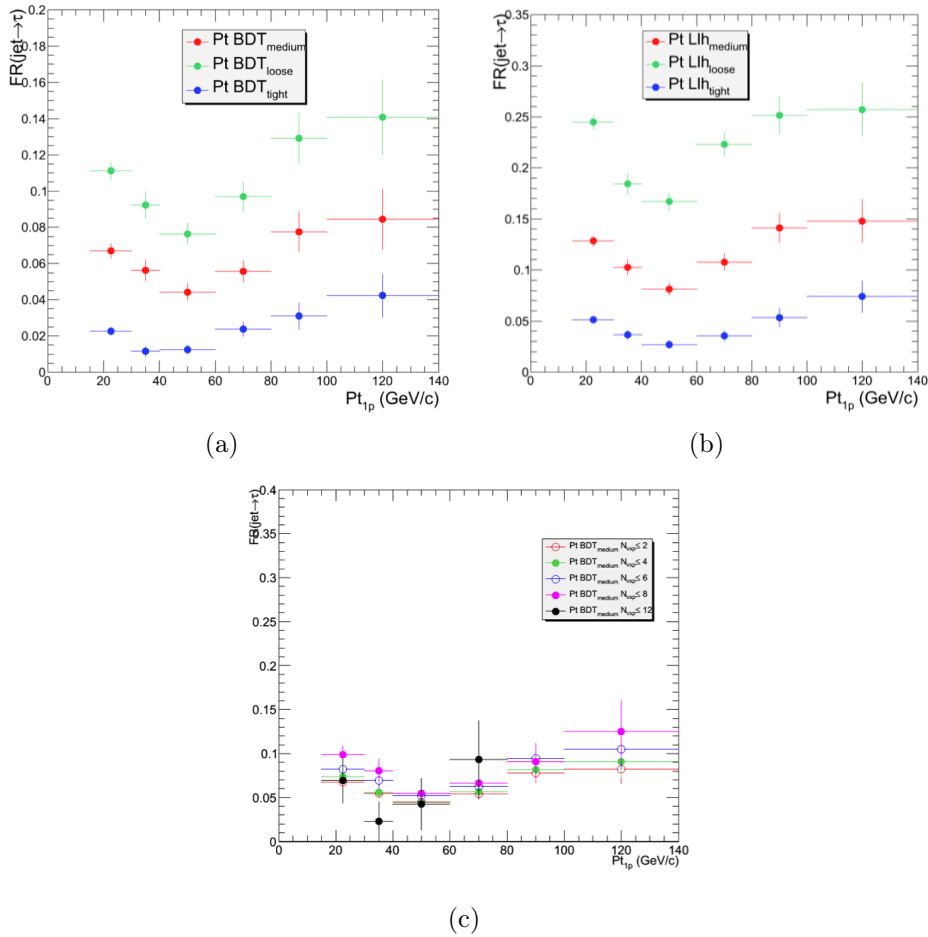
Figura 7.2: (a) Valores de la *fake rate* en función del p_T para las variables τ-BDT *medium*, *loose* y *tight*, y el caso 1-*prong*. (b) Equivalentemente valores de la *fake rate* en función del p_T para las variables τ-LLH. (c) Número de vértices primarios encontrados en los eventos en función del p_T para la topología $\gamma + jets$, clasificados en función del número de vértices (<2, 4, 6, 8, 10 y 12) para el caso de 1-*prong*.

Tabla 7.1: Factores de escala (SF) en función del número de jets en el evento. Los factores de escala vienen dados por la proporción de eventos en MC y datos reales según la multiplicidad de jets una vez sustraída la banda lateral de eventos con una masa entre $60 < M_Z < 70$ GeV o $110 < M_Z < 120$ GeV.

ee			
no.jets	data	MC	SF
0	$5.200{\cdot}10^5$	$5.590{\cdot}10^5$	0.931 ± 0.001
1	$0.816{\cdot}10^5$	$0.825{\cdot}10^5$	0.989 ± 0.003
≥ 2 jets	$0.234{\cdot}10^5$	$0.232{\cdot}10^5$	1.010 ± 0.007

$\mu\mu$			
no.jets	data	MC	SF
0	$9.200{\cdot}10^5$	$9.740{\cdot}10^5$	0.944 ± 0.001
1	$1.530{\cdot}10^5$	$1.490{\cdot}10^5$	1.030 ± 0.003
≥ 2 jets	$0.434{\cdot}10^5$	$0.410{\cdot}10^5$	1.060 ± 0.005

sustracción de bandas laterales, para 0 jet, 1 jet y 2 ó más jets. El fondo sustraído en las distribuciones de datos reales y de MC es pequeño y el efecto de la sustracción en el número real de Z's es despreciable. Los factores de escala derivados de la proporción del número total de eventos calculados para cada Z$\to ll$, se muestran en la tabla 7.1, donde se han usado muestras separadas Z$\to \mu\mu$ y Z$\to$ee. La figura 5.10 muestra las distribuciones Zp_T en función de los bines de multiplicidad del jet para $Z \to ll$ después de la sustracción lateral de bandas. Hay pequeñas diferencias entre las distribuciones en valores bajos de Zp_T, que justifican por qué son necesarios los factores de escala. Las diferencias entre Z$\to ee$ y Z$\to \mu\mu$ son debidas al orden de la incertidumbre estadística si se requiere el p_T de los muones mayor que 25 GeV, como para el caso de los electrones. Los factores de escala aplicados a Z$\to \tau\tau$ son derivados como función del p_T de los Z's, asegurando que la cinemática antes de la desintegración del Z es la misma entre Z$\to ll$ y Z$\to \tau\tau$. La tabla 7.2 muestra los factores de escala obtenidos para las selecciones Z$\to ee$ y Z$\to \mu\mu$ en función de los bines de p_T del Z y del número de jets en el evento ≥ 0, ≥ 1 y ≥ 2. En las secciones B.1 y B.2 se muestran los estudios realizados sobre la dependencia de los factores de escala del Z con la variable *pseudorapitidy* (η) y con la forma de la variable BDT_j, demostrándose dependencia de la multiplicidad de jets con Zp_T, mientras que no existe con el tipo de leptón o valor de η.

7.5.3 Selección de eventos y comparación entre datos y MC

La selección de eventos usados para medir la sección eficaz de la producción de pares de quark top se basa en las condiciones descritas en la sección 5.4. Se resumen en lo siguiente: la selección de eventos se produce mediante un trigger de leptón

Tabla 7.2: Factores de escala en función de los bines de p_T del Z y el número de jets en el evento obtenido a partir de Z→ee y Z→$\mu\mu$.

	$\mathbf{Z}p_T$ (ee) SF	$\mathbf{Z}p_T$ ($\mu\mu$) SF
0 jets		
0-10 GeV	0.942 ± 0.003	0.958 ± 0.003
10-20GeV	0.897 ± 0.005	0.905 ± 0.003
20-30GeV	0.922 ± 0.008	0.923 ± 0.006
30-40GeV	1.020 ± 0.015	1.030 ± 0.011
40-50GeV	1.090 ± 0.029	1.180 ± 0.022
50-60GeV	1.140 ± 0.049	1.200 ± 0.035
60-70GeV	1.190 ± 0.076	1.070 ± 0.048
70-80GeV	1.000 ± 0.092	1.040 ± 0.067
80-100GeV	0.921 ± 0.095	0.919 ± 0.067
100-200GeV	0.965 ± 0.122	0.738 ± 0.073
1 jets		
0-10 GeV	0.733 ± 0.022	0.759 ± 0.017
10-20GeV	0.986 ± 0.021	1.030 ± 0.016
20-30GeV	0.989 ± 0.016	1.040 ± 0.013
30-40GeV	0.982 ± 0.016	1.010 ± 0.012
40-50GeV	0.993 ± 0.018	1.070 ± 0.014
50-60GeV	1.040 ± 0.023	1.100 ± 0.017
60-70GeV	1.080 ± 0.029	1.090 ± 0.021
70-80GeV	1.050 ± 0.035	1.070 ± 0.026
80-100GeV	1.060 ± 0.033	1.050 ± 0.025
100-200GeV	0.992 ± 0.030	0.997 ± 0.025
$\geq$ 2 jets		
0-10 GeV	0.828 ± 0.051	0.914 ± 0.041
10-20GeV	1.020 ± 0.046	1.060 ± 0.035
20-30GeV	0.993 ± 0.041	1.020 ± 0.030
30-40GeV	1.020 ± 0.041	1.080 ± 0.031
40-50GeV	0.979 ± 0.041	1.100 ± 0.032
50-60GeV	1.000 ± 0.043	1.130 ± 0.034
60-70GeV	1.090 ± 0.050	1.090 ± 0.035
70-80GeV	1.060 ± 0.052	1.100 ± 0.039
80-100GeV	1.070 ± 0.042	1.030 ± 0.031
100-200GeV	1.010 ± 0.031	1.020 ± 0.026

individual, un evento debe contener un vértice primario con al menos cinco trazas, un jet con $p_T > 20$ GeV, al menos un candidato a τ y $E_T^{miss} > 30$ GeV, al menos dos jets con $p_T > 25$ GeV no solapando con el candidato a τ, el candidato a τ y el leptón deben de ser de signo opuesto y al menos un jet debe de ser identificado como b-jet (≥ 1 b-tag).

El número de eventos observados y esperados después de cada corte para una luminosidad integrada de 4,73 fb^{-1}, se muestra en la tabla 7.3 para el caso de 1-*prong* en ambos canales $(e + \tau)$ y $(\mu + \tau)$. Se puede observar como después del requerimiento de E_T^{miss}, el fondo de Z se ha reducido. Los fondos remanentes corresponden a W+jets y $t\bar{t} \to l+jets$, donde un jet es erróneamente identificado con un candidato a τ. El fondo W+jets se reduce después del requerimiento de b-tag. Los eventos $t\bar{t}(\ell\ell')$, son eventos dileptones $t\bar{t}$ con sólamente un leptón reconstruído como tal y un leptón o jet reconstruído como un τ. Los errores corresponden a las incertidumbres estadísticas.

La figura 5.14 muestra las distribuciones de la masa invariante (M_t) para τ_1, comparando datos y MC en diferentes etapas de la selección de eventos, antes y después del corte de b-tag para ambos canales e y μ. Los puntos negros representan las distribuciones de datos y los histogramas coloreados representan los datos generados por MC. Las gráficas en la parte baja de cada representación muestran la relación (Datos$-$MC)/MC. El acuerdo entre ambos es aceptable dentro de la incertidumbre estadística. Equivalentemente, la figura 5.15 muestra las distribuciones BDT para 1-*prong*. Después del requerimiento de E_T^{miss} y antes del corte en 1 b-tag, el fondo dominante es el proceso W+jets, como previamente se ha indicado en la descripción de la tabla de cortes, siendo el fondo dominante $t\bar{t} \to l + jets$ después del corte en 1 b-tag. La mayor contribución procede de jets falseando τ's. Como el modelo de fondo para este análisis es derivado de datos, los fondos multi-jet, las distribuciones MC y las incertidumbres, no afectan a la medida de la sección eficaz.

Tabla 7.3: Tabla de cortes $(e + \tau)$ y $(\mu + \tau)$ para candidatos a τ_1, con incertidumbres estadísticas.

e 1p-Cut	$t\bar{t}(\ell\tau_{had})$	$t\bar{t}(\ell jet)$	$t\bar{t}(\ell\ell)$	Z + jets	W + jets	Single Top	Diboson	MC Total	Data
$\geq 1\ \tau$ cand	1071 ± 7	4683 ± 15	257 ± 4	41920 ± 130	173182 ± 524	1166 ± 16	1726 ± 8	224005 ± 540	276430
$N_{jet} > 2$	827 ± 6	4328 ± 14	203 ± 3	6697 ± 35	12565 ± 88	571 ± 10	390 ± 4	25580 ± 96	30825
$E_T^{miss} > 30$	711 ± 6	3397 ± 13	182 ± 3	1889 ± 18	8773 ± 73	431 ± 9	238 ± 3	15621 ± 77	16463
OS	697 ± 6	2312 ± 11	100 ± 2	1167 ± 15	5525 ± 57	313 ± 7	158 ± 2	10271 ± 61	10404
≥ 1 b$-$jet	588 ± 5	1841 ± 9	76 ± 2	97 ± 4	328 ± 14	219 ± 6	18 ± 1	3167 ± 19	3382
≥ 2 b$-$jet	240 ± 3	660 ± 5	24 ± 1	5 ± 1	17 ± 3	40 ± 3	1 ± 0	988 ± 8	1079
μ 1p-Cut	$t\bar{t}(\ell\tau_{had})$	$t\bar{t}(\ell jet)$	$t\bar{t}(\ell\ell)$	Z + jets	W + jets	Single Top	Diboson	Total	Data
$\geq 1\ \tau$ cand	1362 ± 8	6097 ± 17	326 ± 4	49097 ± 137	275302 ± 680	1488 ± 18	2283 ± 9	335955 ± 695	450885
$N_{jet} > 2$	1062 ± 7	5635 ± 16	261 ± 4	3546 ± 25	19943 ± 120	706 ± 11	448 ± 4	31601 ± 124	40255
$E_T^{miss} > 30$	921 ± 7	4528 ± 15	234 ± 3	1587 ± 17	14584 ± 103	559 ± 10	318 ± 3	22730 ± 106	23536
OS	908 ± 7	3089 ± 12	130 ± 3	1134 ± 14	9150 ± 80	399 ± 8	216 ± 3	15025 ± 82	14773
≥ 1 b$-$jet	756 ± 6	2467 ± 11	98 ± 2	107 ± 5	537 ± 20	274 ± 7	24 ± 1	4262 ± 25	4567
≥ 2 b$-$jet	314 ± 4	894 ± 6	32 ± 1	9 ± 2	33 ± 5	53 ± 3	2 ± 0	1337 ± 9	1393

7.5.4   Método de ajuste para la estimación de la sección eficaz a 4.73 fb^{-1}

En este trabajo se presenta una medida de la sección eficaz que utiliza una técnica desarrollada para 2 fb^{-1} [64], adaptada y mejorada para el cálculo a 4.73 fb^{-1}. La técnica usa distribuciones Boosted Decision Tree τ-jet (BDT$_j$) de eventos seleccionados, ajunstándolas a plantillas que identifican por su forma leptones τ y falsos τ, consiguiendo separar de este modo procesos de señal, de procesos con jets erróneamente identificiados como τ. La variable discriminante BDT$_j$ tiene distribuciones diferentes para cada proceso de fondo dependiendo de qué tipo de jet esté falseando un τ, por tanto, las plantillas que se puedan obtener de las distribuciones serán también diferentes. Los falsos τ originados de gluones ó b-jets, presentan normalmente un valor BDT$_j$ menor. En cambio los que provienen de jets de *light-quark*, tienen un valor intermedio entre τ y gluón o b-jet. En estudios anteriores con 2 fb^{-1} [68], se sustraían eventos donde el leptón y el candidato a τ tenían el mismo signo de carga (SS), de eventos con signo de carga opuesto (OS). De este modo se eliminaba la contribución de gluones, ya que el τ en la señal era siempre OS con los leptones. Pero esto producía un incremento del error estadístico, por lo que en este análisis se ha usado toda la selección de datos OS para reducirlo y poder construir un modelo de fondo mejorado, en el que se incluyen W+jets, para jets de *light-quarks* y gluones. A partir de las ecuaciones 5.6 a 5.11, que expresan distribuciones BDT$_j$ obtenidas como una suma de jets de *light-quarks* y jets de gluones, se puede obtener la ecuación $k_1 \cdot OS1 + k_2 \cdot Gluons$, donde k_1 y k_2 representan constantes, $OS1$ representa las distribuciones de signo opuesto para W + 1 jet, y *Gluons* las de gluones. Esta expresión reproduce cualquier distribución BDT$_j$ construída con una mezcla de jets de *light-quarks* y gluones.

Extracción de señal mediante ajuste de la forma de BDT$_j$

El método usado para extraer la señal después del requerimiento de b-tagging (etiquetado), ajustando el fondo MC a los gluones y la plantilla de W, permite reducir dicho fondo. Después de la preselección y la selección de b-tagging, el fondo dominante en el canal *lepton+jets*, es la producción de pares del quark top. Para suprimirlo, se aplica la técnica $TauID$. Para realizar los ajustes se usa la variable BDT$_j$, ya que es la que mejor describe las diferencias de forma entre señal y fondo. La plantilla de la señal BDT$_j$ deriva de candidatos a τ de MC, emparejados a un τ real. Consiste en señales $t\bar{t} \rightarrow \tau + \ell$, $Z \rightarrow \tau^+\tau^-$, y una pequeña contribución de eventos 'single top' y dibosones. Como se ha explicado en el apartado anterior, la plantilla de fondo proviene de datos y consiste en jets de *light-quarks* y gluones falseando τ's provenientes de muestras de datos enriquecidos con W+jets. Usando ambas plantillas, se realiza un ajuste χ^2 con parámetros que fijan la normalización

de cada plantilla según la ecuación 5.12, sobre la que se lleva a cabo un ajuste a dos parámetros, después de imponer la condición de que la suma de señal y fondo debe añadirse al número de eventos observados. Los resultados combinados de los canales e y μ se obtienen ajustando la suma de las distribuciones. Las formas de los canales e y μ concuerdan. Los ajustes son realizados sobre muestras con al menos 1 b-tag.

Aplicación del método de ajuste a muestras $4{,}73$ fb^{-1}

El método es testeado usando dos muestras de MC estadísticamente independientes. Una de las muestras es usada previamente para construir el fondo esperado para dos regiones de E_T ($20 < E_T < 35$ GeV y $35 < E_T < 100$ GeV), que serán ajustadas con las plantillas de fondo. El nivel de confianza correspondiente al valor χ^2/ndf indica que las plantillas de fondo no lo reproducen correctamente, como se puede observar en la figura 5.20. Las plantillas de señal y fondo se crean más tarde con una segunda muestra, utilizando para ello las correcciones de fondo que se muestran en la figura 5.21. La figura 5.22 muestra los resultados del ajuste para ≥ 1 b-tag. La figura 5.23 corresponde al ajuste sin correciones. En la tabla 7.4 se pueden observar los resultados del ajuste antes y después de aplicar las correcciones. A pesar de las pequeñas diferencias en la señal medida y en la esperada en el primer bin de p_T después de las correciones, los valores del ajuste obtenido después de realizarlas demuestran que el método funciona bien.

Tabla 7.4: Valores esperados de MC y resultado del ajuste usando muestras MC estadísticamente independientes como datos y plantillas, antes y después de las correcciones. Los números entre paréntesis son valores de χ^2/ndf.

	S_{MC}	$S_{Fitted}^{BeforeCorrections}$ (χ^2)	$S_{Fitted}^{AfterCorrections}$ (χ^2)
$20 < E_T < 35$GeV	721.7 ± 6.5	638.7 ± 41.3 (0.5542)	703.6 ± 51.2 (0.0936)
$35 < E_T < 100$GeV	724.8 ± 6.4	612.4 ± 39.8 (1.9325)	721.1 ± 39.6 (0.0062)

Aplicación del método de ajuste a datos reales

En el siguiente paso, el método de ajuste se aplica a datos de ATLAS para extraer la señal $t\bar{t} \rightarrow \tau + \ell$. Los canales e y μ son combinados de modo que las distribuciones BDT de datos para los dos canales se suman. La figura 5.24 y la tabla 5.13, muestran el resultado final del ajuste, con un χ^2/ndf sobre la unidad, demostrando que el método es aceptable.

7.5.5　Incertidumbre sistemática

El análisis de eficiencias e incertidumbres sistemáticas depende principalmente del número de *prongs* del τ, de la alta o baja multiplicidad de vértices primarios en el evento, del p_T del τ y de su identificación. Las principales incertidumbres sistemáticas se deben al Monte Carlo, afectando al método de ajuste en pequeños cambios en la forma del BDT_j, por ejemplo la incertidumbre de la forma del fondo que proviene de la sustracción de la señal, como la incertidumbre de los factores de escala $Z + jets$ estudiados anteriormente y las incertidumbres de la identificación del τ. Estas fuentes de error son tomadas en cuenta en la evaluación de la sección eficaz, variando la contribución de la señal dentro del rango de error sistemático para cada contribución. Las incertidumbres en la sección eficaz han sido derivadas utilizando muestras variadas en $\pm 1\sigma$ y aplicando el método de ajuste. La sección eficaz extraída y la de la muestra nominal, se comparan en ambos canales juntos (e y μ) para 1-*prong*. Los valores obtenidos se muestran en la tabla 7.5.

Tabla 7.5: Incertidumbres sistemáticas absolutas en *pb*, para la estimación de la sección eficaz en el caso de τ_1 y 1 b-*tag*. La primera columna muestra la fuente de incertidumbre sistemática. La incertidumbre asociada a la identificición del τ incluye electrones erróneamente identificados como leptones τ.

Source	Uncertainties (pb)
τ_1 Statistical	10.0
μ (ID/Trigger)	0.2
e (ID/Trigger)	0.2
Jet E scale	$-5,2$ / $+5,9$
Jet E res.	1.3
ISR/FSR	12.5
Generator	10.3
$b-$tag	$-7,3$ / $+9,4$
τ_1 ID	8.4
total syst. τ_1	$-19/+20$
total	10 (stat) $^{+20}_{-19}$ (syst)

7.5.6 Medida de la sección eficaz del par $t\bar{t}$ en el canal $\ell + \tau$ a 4.73 fb^{-1}

La sección eficaz se calcula a partir del número de eventos observados en la señal medidos por el ajuste a la forma del BDT_j en la región de señal, mediante la siguiente expresión:

$$\sigma_{t\bar{t}} = \sigma_{t\bar{t}(SM)} \cdot \frac{S_{measured}}{S_{MC}} \tag{7.2}$$

donde $\sigma_{t\bar{t}(SM)}$, es la sección eficaz teórica, S_{MC} es el número de eventos esperados de la simulación, y $S_{measured}$ la señal medida. El resultado estimado para los canales e y μ considerados simultáneamente, en el caso de τ_1 y 1 b-*tag* es:

$$\sigma_{t\bar{t}} = 184 \pm 10(\text{stat.}) \pm {}^{+20}_{-19}(\text{syst.}) \pm 3{,}3(\text{lumi.})\text{pb}$$

Este valor está de acuerdo con lo esperado según el Modelo Estándar para 4,73 fb^{-1} (177,3 pb) y con las medidas previas obtenidas para 2 fb^{-1} [68]. Los resultados presentados en este trabajo, además de otros estudios que ayudan a la compresión y mejora del método de ajuste, se encuentran publicados en una nota ATLAS [69].

7.6 Sumario y conclusiones

En este trabajo se presentan estudios concernientes al calorímetro hadrónico Tile-Cal del experimento ATLAS, en el gran acelerador de partículas LHC y un análisis de la física en el marco de la producción de pares de quarks $t\bar{t}$, con leptones τ en el estado final. La primera parte representa una contribución a la puesta en marcha del calorímetro hadrónico TileCal y del segundo nivel del trigger de muones. Este estudio incluye:

- Testeo y descripción del sistema de monitoreo de TileCal utilizado durante el período de puesta en marcha, el cual contribuyó a alcanzar posteriormente el correcto funcionamiento del detector. El proceso de verificación de la calidad de los datos de TileCal, realizado a través de diferentes etapas, tanto en línea como fuera de línea, funcionó correctamente y permitió una toma de datos y procesamiento eficiente.

- Resultados de estudios con TileMuID, un algoritmo basado en TileCal, implementado en el trigger de muones de segundo nivel de ATLAS, que permitió etiquetar muones de bajo momento transvero. Los resultados obtenidos fueron publicados en una nota de ATLAS [27], verificando que el sistema quedó

completamente operativo y preparado para la adquisición de datos durante las colisiones. Muestras con mayor estadística se utilizaron posteriormente para la plena puesta en marcha del sistema de trigger, pero los escasos datos disponibles en el momento de este análisis no permitieron establecer una estimación cuantitativa de la eficiencia y resolución de los diferentes niveles del trigger.

La segunda parte de esta tesis constituye una contribución a la física del quark top, obteniendo una primera estimación de la sección eficaz del par $t\bar{t}$ en colisiones *proton-proton* a 4,73 fb^{-1}. Los datos se han obtenido en ATLAS para un valor de la energía de $\sqrt{7}$ TeV en el centro de masas, usando el canal con un leptón (electrón o muón) y un τ desintegrándose hadrónicamente. Este trabajo incluye:

- El cálculo de la probabilidad de error en la identificación de leptones τ desintegrados hadrónicamente, con muestras de $\gamma + jets$. Este estudio usa dos métodos de identificación del tau (BDT y LLH) con datos de 2011, validando el uso del algoritmo BDT para el resto del análisis. Para el caso de 1-*prong*, la probabilidad varía entre 0.01 % y 0.15 % usando el algoritmo de identificación BDT y entre 0.02 % y 0.25 % con LLH. El estudio en función del número de vértices proporciona valores entre 0.02 % y 0.13 %. Las probabilidades dependen del algoritmo de identificación del τ, del número de prongs del candidato a τ, de su p_T, del origen de los jets reconstruídos como candidatos a τ y del número de vértices primarios encontrados en el evento. El algoritmo τ-BDT es más eficiente que el algoritmo τ-LLH, lo que es considerado para el resto del análisis.

- El cálculo de los factores de escala requeridos para la estimación de la sección eficaz para $t\bar{t}$. Se han realizado estudios comprobando la dependencia con η a través de las medidas de la variable BDT, representativa en la identificación de leptones τ. Se ha observado que las distribuciones Z-p_T, dependen de la multiplicidad del jet y son independientes del tipo de lepton o valor de η. Este estudio contribuye a la nota de ATLAS [63].

- La aplicación de una técnica basada en la variable BDT (de la que depende la identificación del leptón τ en ATLAS), capaz de separar la señal de los fondos de quarks y gluones de jets. El método permite obtener distribuciones BDT_j correspondientes a jets de gluones erróneamente identificados y otras distribuciones principalmente compuestas por jets de *light-quarks* más una pequeña mezcla de W+jets. Estas distribuciones son ajustadas a la región de señal y a la plantilla de fondo para la identificación del leptón τ. La sección eficaz resultante para el caso τ_1 y la selección de 1 b-*tag* es:

$$\sigma_{t\bar{t}} = 184 \pm 10(\text{stat.}) \pm {}^{+20}_{-19}(\text{syst.}) \pm 3{,}3(\text{lumi.})\text{pb}$$

medida que está en buen acuerdo con los valores teóricos que se obtienen a partir del Modelo Estándar y con medidas previas a 2 fb^{-1}. Este estudio contribuye a la nota de ATLAS [69].

Appendices

Appendix A

Calibration Tests

Various systems have been designed to calibrate the different elements in the electronic chain, which allow monitoring the calorimeter. They are summarized in section 4.1.3. In this appendix, some histograms taken during TileCal commissioning for CIS and Laser calibration runs are displayed to complement Chapter 4 descriptions on DQA process.

CIS run

The next histograms show some digital readout data integrity checks. For each Data Management Unit (DMU), Bunch Crossing Identification (BCID) errors are checked for low gain (LG) and high gain (HG), as it is showed in figure A.1. The X-axis represents the DMUs' number and the value of the gain is represented on the Y-axis. Usually these errors indicate that data are corrupted, and a module with this problem should be marked as bad. Figure A.2 shows histograms of Cyclic Redundancy Codes (CRC) errors, in the module 56. On the Y-axis, it is indicated which part has a possible error. No errors were found, but one thing to keep in mind in these checks, is that if the module also has CRC errors, the BCID error can be a consequence of corrupted data. The checks for CRC, are calculated for each event on the data from each single DMU within a drawer. It is usually accompanied by global CRC error checks and can indicate deteriorating digitizer.

Figure A.3, shows the reconstructed amplitude, error and time for each channel using a fitting method to the signal [26]. It is tested the charge linearity in the CIS scan run. In both LG and HG, the reconstructed signal amplitude divided by the injected charge (Amp/Q ratio), is calculated for each of the capacitors used (100pF or 5pF). For good channels, this quantity should be close to one. If the Amp/Q ratio is not close to one or the error bars are large, it means that there

145
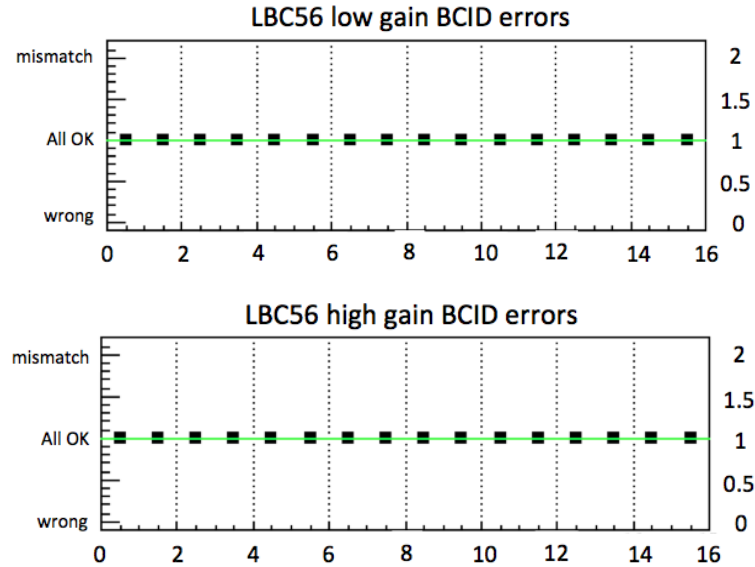
Figure A.1: Histograms produced to check the possibility of finding BCID errors, for one of the long barrel modules . On the X-axis it is represented the DMUs' number.

are many events in the tails of the Amp/Q distribution. In that case, the channels should be marked as bad. Looking at figure A.3 one can see that PMT's 30, 31 and 43 are not working. To verify the correct behavior of the calibration system, this test is the most important, together with data integrity tests in the CIS runs.

Figure A.4 shows the time slope of the PMT's as a function of time of the injected charge, compared for both LG and HG in both capacitors (100 pF and 5 pF). A slope of zero means that there is no variation of the pulse timing.

Among all histograms that can be checked for a CIS scan, there are some that check noise and pedestal histograms, intended to monitor the baseline noise levels and observation of any changes of the noise levels with time. The level of the pedestal for each channel should be between 40 and 70. This test gives a general overview of the noise level of each channel, but the pedestal root mean square (RMS) tests are more important for determining noisy channels. The expected value of the signal amplitude depends on the run type, and for Pedestal runs the response should be around zero in both gains. In Pedestal runs, a failure of the amplitude test is often in conjunction with other errors in the noise checks. The timing for a module should be uniform across all channels and there should be no problem within a channel.
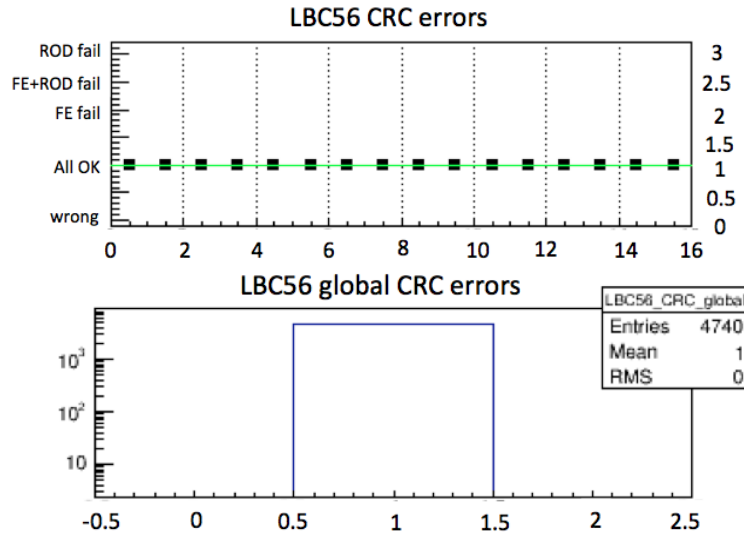
Figure A.2: Histograms showing Cyclic Redundancy Codes (CRC) checks for errors in the long barrel module number 56, where everything looks to work correctly. X-axis represents the DMUs' number.

Laser run

A few histograms from a laser run are showed in the following. For these kind of runs, only LG values are checked. To check the energy reconstruction representation, the fit and optimal filtering methods are used [26] (see section 4.1.1). Figure A.5, shows in blue shading, the sum of all histograms (DSP-OF) for all channels. It is represented the amplitude and time with its RMS. PMT number 31 shows a problem. Figure A.6 shows the low gain amplitude and RMS of Amplitude for LB56 module.
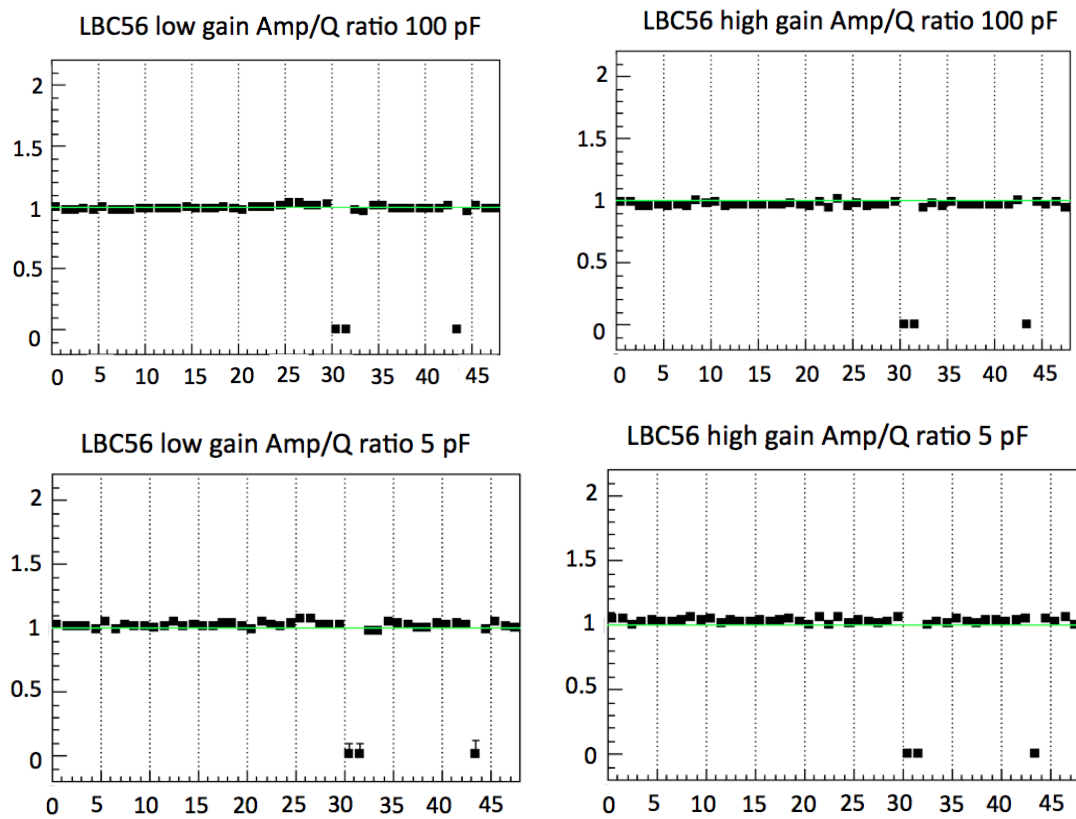
Figure A.3: On the top, CIS scan amplitude histograms at 100 pF of capacitance, for low gain on the left and high gain on the right. The X-axis represents the PMT's number. On the bottom, same histograms at 5 pF of capacitance. One can see some dead channels.
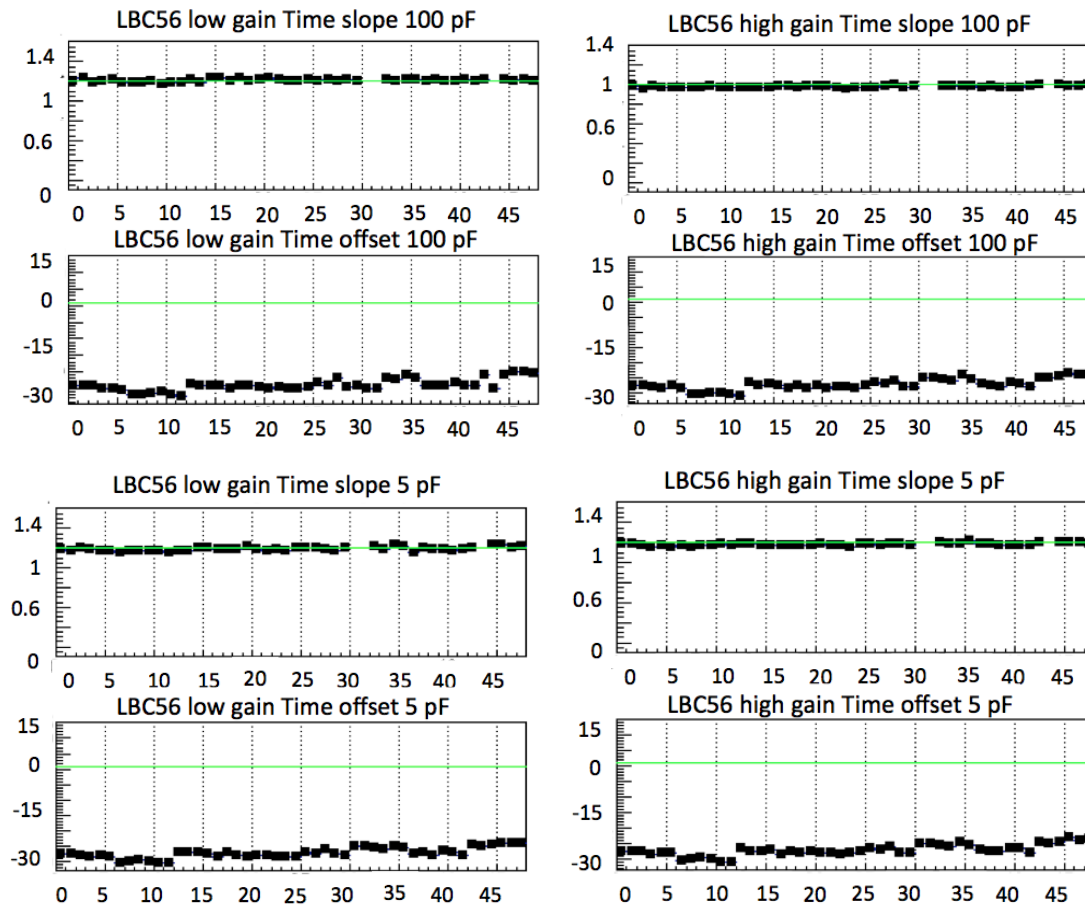
Figure A.4: Time slope and offset in a CIS scan, at 100 pF of capacitance, on the first and second rows. A low value of the gain time slope, would indicate that there is no variation of the pulse timing. On the third and fourth rows, time slope and offset in a CIS scan, at 5 pF of capacitance.
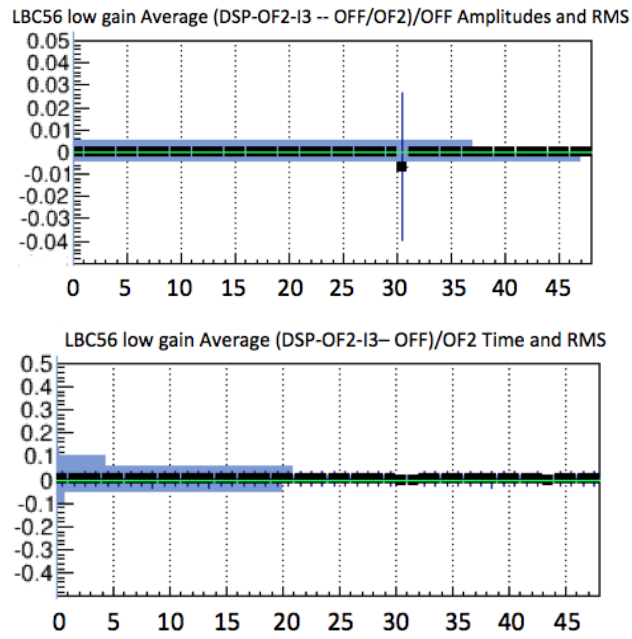
Figure A.5: Optimal Filtering histograms.
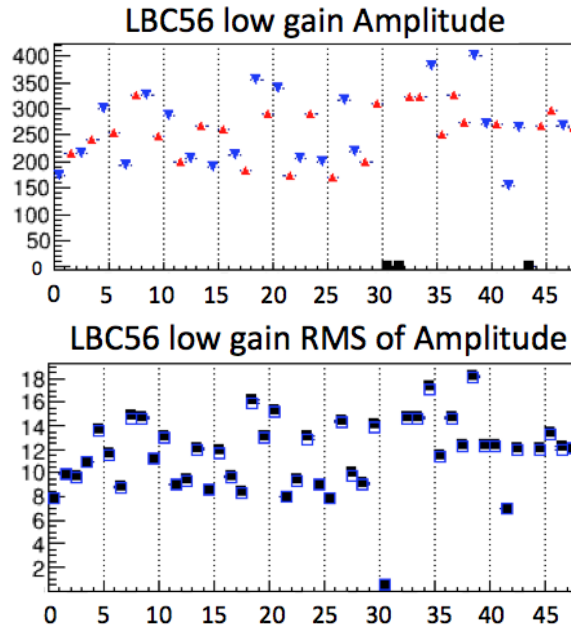
Figure A.6: Low gain amplitude and RMS of Amplitude for LB56 module.

Appendix B

Scale Factors Studies

This appendix shows different studies carried out for the scale factors calculation, displayed in section 5.3. To perform this specific systematic study of the Zp_T, some MC distributions obtained from $Z \to ee + jets$ and $Z \to \mu\mu + jets$ channels have been compared with real data, checking the dependency of the scale factors with η and BDT_j shape.

B.1 Studies of the Z dependence with η distributions

Using a fixed jet multiplicity, there are two configurations of interest according to the pseudorapidity interval of the leptons:

1. having both leptons in the central part of the detector, with $\mid \eta \mid < 1.37$

2. having one lepton in the central region and the other one in the forward region, that means one with $\mid \eta \mid < 1.37$ and the other lepton with $\mid \eta \mid > 1.52$

The first case of study is displayed in figure B.1, showing an agreement in the distributions for e's and μ's respectively, and for data and MC. Figure B.2 shows agreement between the distributions for the second η selection case. In both cases, the Zp_T distributions are dependent on jet multiplicities and there is no η dependence with jet multiplicity. Zp_T and pseudorapydity distributions for muons and electrons are very close. When increasing the jet multuplicity, the Z boson is more boosted and the two Z-decaying leptons have closer pseudorapidities. The corresponding distributions for e's and μ's channels are quite compatible; assuming they are coincident, it is possible to calculate global scale factors as the average of the ones obtained for the individual distributions.
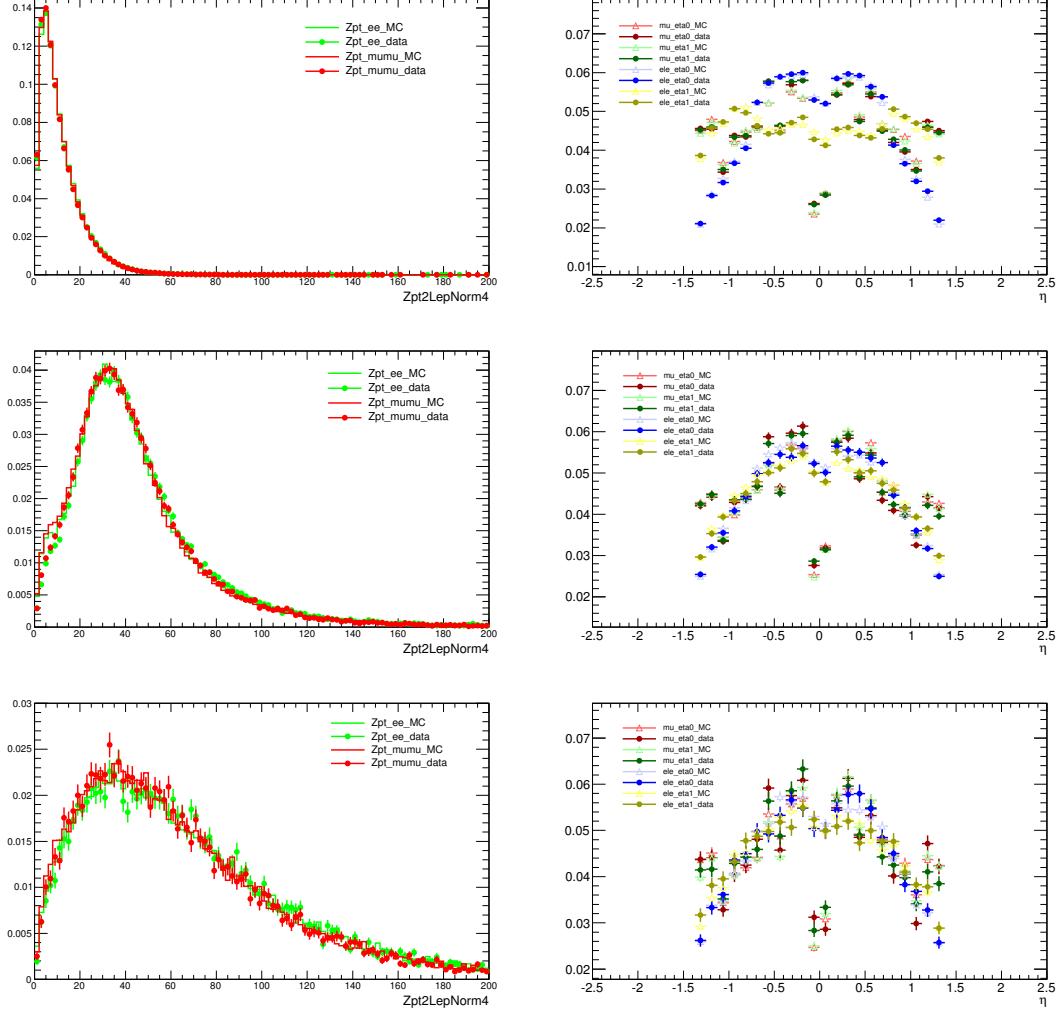
Figure B.1: On the left, the Zp_T normalized distributions for Z$\to ee + jets$ and Z$\to \mu\mu + jets$ channels, for data and MC (named Zpt_ee and Zpt_mumu) and a fixed jet multiplicity. Both leptons have the same η value, $| \eta |< 1.37$. The column on the right shows the pseudorapidity distributions of the first lepton, the one with the highest p_T (named mu_eta0 and ele_eta0 for MC and data selections) and the second lepton (named mu_eta1 and ele_eta1 for MC and data selections). First row shows the zero jet multiplicity case, second row shows the one jet multiplicity case and the third one the case of two o more jets.
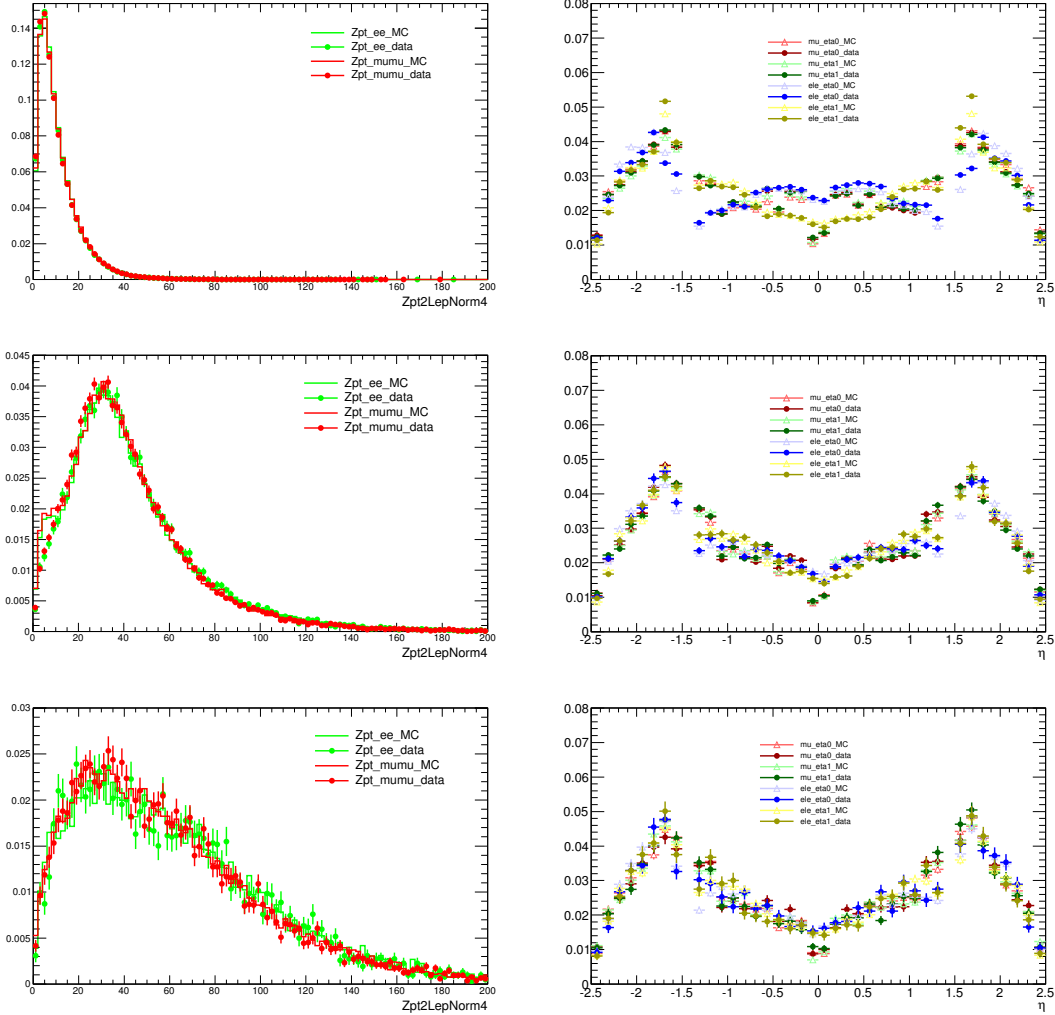
Figure B.2: On the left, the Zp_T normalized distributions for Z$\rightarrow ee + jets$ and Z$\rightarrow \mu\mu + jets$ channels, for data and MC (named Zpt_ee and Zpt_mumu) and a fixed jet multiplicity. The two leptons have different η value, one lepton with $\mid \eta \mid < 1.37$ and the other lepton with $\mid \eta \mid > 1.52$. The right column shows the pseudorapidity distributions of the first lepton, the one with the highest p_T (named mu_eta0 and ele_eta0 for MC and data selections) and the second lepton (named mu_eta1 and ele_eta1 for MC and data selections). First row shows the zero jet multiplicity case, second row shows the one jet multiplicity case and the third one the case of two o more jets.

B.2   Studies of the Z dependence with BDT_j shape

A measure of the uncertainty on the signal is the number of events after $BDT_j >$ 0.7 cut. The difference between using e's or μ's scale factors gives us an idea of the sensitivity. In order to quantify the sensitivity of the predicted number of signal events after certain cut on BDT_j, to the correction with scale factors obtained with differentiated Z$\to ee$ and Z$\to \mu\mu$ data set, Z$\to \tau\tau$ events have been selected applying the event selection for the $e/\mu + \tau$ channels. A derived histogram has been built from BDT_j distributions corrected with the scale factors, which allows to illustrate the sensitivity of the obtained numbers:

$$\Delta(BDT_1, BDT_2) = 2 \cdot \frac{(BDT_1 - BDT_2)}{(BDT_1 + BDT_2)} \tag{B.1}$$

where BDT_1 is the resulting distribution using the Zee scale factors and BDT_2 is the equivalent using Z$\mu\mu$.

There are two BDT distributions of interest:

1. **Distributions for τ_{ID}**: to check the uncertainty, events with zero jets and one jet not overlapping with the τ candidate are added. It is required at least one jet not overlapping with the τ candidate, $\tau_{p_T} > 20$ GeV, $\mu_{p_T} > 20$ GeV, $n_{jets} < 2$ and the transverse mass of the leptons $M_t(l, E_T^{miss}) < 20$ GeV to reduce W+jets background in the $Z \to \tau\tau$ samples. Samples of interest in this study are only $\mu + \tau$ events.

2. **Distributions for Z$\tau\tau$ contribution to $t\bar{t}$ events selection**: to check the uncertainty, the data sample events are selected with $n_{jets} > 1$ not overlapping with the τ candidates, with the requirement of $E_T > 30$ GeV, $\tau_{p_T} > 20$ GeV, $\mu_{p_T} > 20$ GeV and $e_{p_T} > 25$ GeV, which are all the cuts used to select $t\bar{t}$ candidates. For this case, $e + \tau$ and $\mu + \tau$ channels are combined and Z$\mu\mu$ or Zee scale factors applied.

Figure B.3 shows BDT distributions using the cuts described in the first case, applying Z$\mu\mu$ and Zee scale factors to Z$\tau\tau$ channel with only $\mu + \tau$ samples. Figure B.4, shows BDT distributions using the cuts described in the second case, applying Z$\mu\mu$ and Zee scale factors to Z$\tau\tau$ channel with both $e + \tau$ and $\mu + \tau$ samples. From these histograms, the observed difference is quite small.

Figure B.5, shows the derived histograms obtained from BDT distributions using the different scale factors. For τ_1-*prong*, the statistics at low BDT values is poor. It can be expected a large uncertainty, but this is not important since the
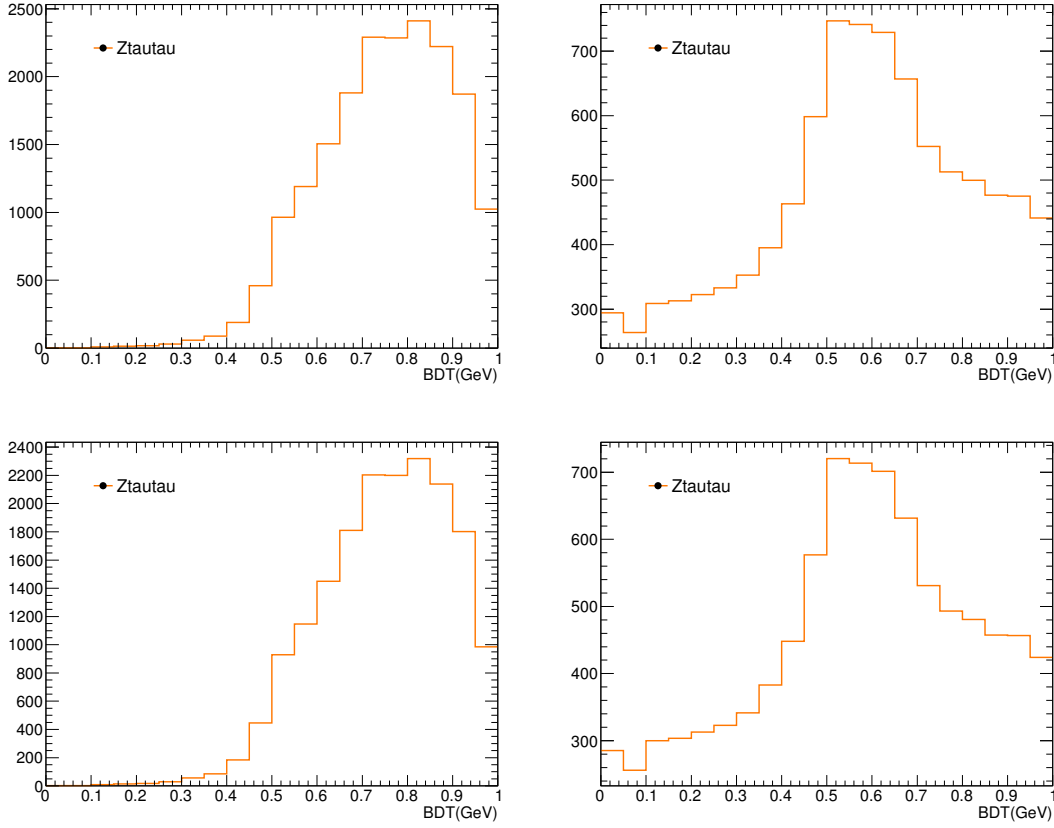
Figure B.3: BDT distributions for case 1, using only $\mu+\tau$ samples, applying $Z\mu\mu$ scale factors (on the first row) and Zee scale factors (on the second row) to $Z\tau\tau$ channel. On the left for τ_1-*prong* case and on the right for τ_3-*prong*.

interest is about the signal and its contribution from low BDT is small. In the case of τ_3-*prong*, the values have larger errors because of lower statistics and the fewer events are more uniformly distributed. The systematic shift is only a small percentage, which is acceptable and of the same size as the statistical uncertainty.

As a conclusion of these studies, which have checked the dependence of the scale factors with η and BDT_j shape by measuring the uncertainty of the signal using the BDT identification variable, it can be said that distributions on Zp_T depend on the jet multiplicity and they are independent on the kind of lepton or η value.
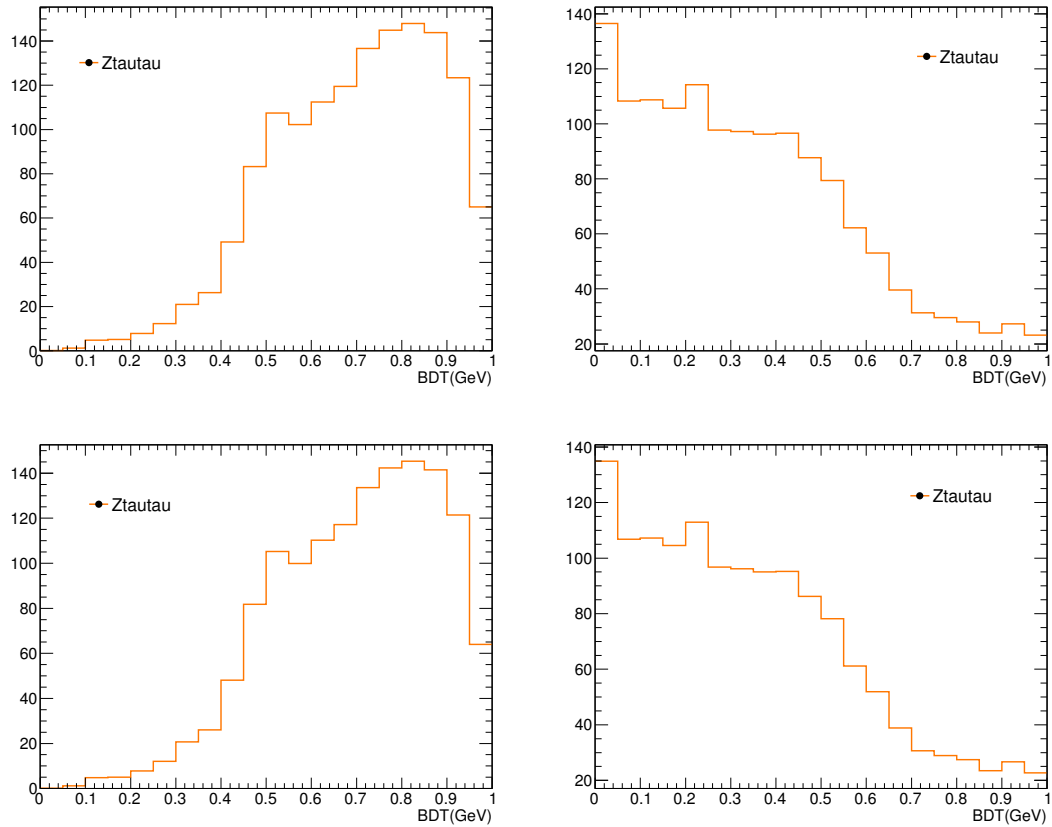
Figure B.4: BDT distributions for case 2, using both $e + \tau$ and $\mu + \tau$ samples, applying Z$\mu\mu$ scale factors (on the first row) and Zee scale factors (on the second row) to Z$\tau\tau$ channel. On the left for τ_1-*prong* case and on the right for τ_3-*prong*.
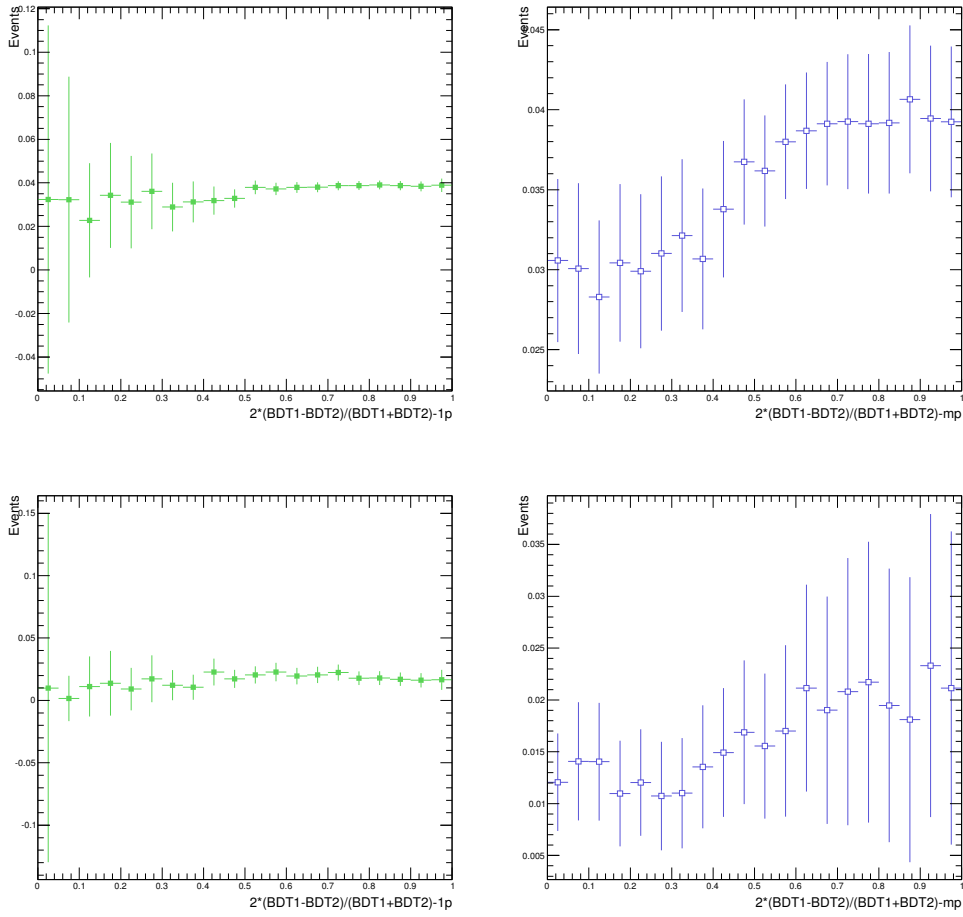
Figure B.5: First row, shows the derived distributions of BDT from the case 1 of study, for τ 1-prong (left) and for τ 3-prong (right). It is represented the difference expressed in equation B.1, being BDT_1 the histogram for Z_{ee} scale factors and BDT_2 the histogram for $Z_{\mu\mu}$ scale factors. Equivalently, the second row shows the derived distributions of BDT from the case 2 of study.

Bibliography

[1] LHC web page. http : //lhc.web.cern.ch/lhc/.

[2] The ATLAS Collaboration. The ATLAS experiment at the CERN Large Hadron Collider. JINST, 3(S08003), 2008.

[3] The ATLAS Collaboration. The ATLAS experiment at the CERN Large Hadron Collider. Chapter 4: Inner Detector. JINST, 3(S08003), 2008.

[4] The ATLAS Collaboration. The ATLAS experiment at the CERN Large Hadron Collider. Chapter 5: Calorimetry. JINST, 3(S08003), 2008.

[5] The ATLAS Collaboration. The ATLAS experiment at the CERN Large Hadron Collider. Chapter 6: Muons Spectrometer. JINST, 3(S08003), 2008.

[6] ATLAS computing: Technical design report G. Duckeck et al. (ATLAS Collaboration). 2005. CERN-LHCC-2005-022.

[7] ATLAS Collaboration, Commissioning of the ATLAS high-performance btagging algorithms in the 7 TeV collision data, ATL-CONF-2011-102

[8] ATLAS Collaboration, Jet energy measurement with the ATLAS detector in proton-proton collisions at $\sqrt{s} = 7$ TeV, arXiv:1112.6426

[9] ATLAS Collaboration, Measurement of the inclusive $W^{\pm}$ and Z/γ cross sections in the e and μ decay channels in pp collisions at $\sqrt{s} = 7$ TeV with the ATLAS detector, arXiv:1109.514v3

[10] Study of hadronic tau identification using W and Z events(ATL-COM- PHYS-2012-1744)

[11] M. Cacciari, G. P. Salam, and G. Soyez, The Anti-k(t) jet clustering algorithm, JHEP 0804 (2008) 063, arXiv:0802.1189 [hep-ph].

[12] https://twiki.cern.ch/twiki/bin/viewauth/Atlas/WorkBookComputingModel

[13] https://twiki.cern.ch/twiki/bin/viewauth/Atlas/WorkBookAthenaFramework

[14] http://proj-gaudi.web.cern.ch/proj-gaudi/

[15] http://www.cmtsite.org

[16] S. Agostinelli et al. (GEANT4 Collaboration). ÒGeant4: A simulation toolkitÓ. Nucl.Instrum.Meth., A506:250Ð303, 2003

[17] http://www.sysf.physto.se/ klere/tile-dmu/chip.html

[18] V. Gonzalez et al. Development of the Optical Multiplexer Board Prototype for Data Acquisition in the TileCal System. Nuclear Science, IEEE Transactions on, 53(4):2131Ð2138, August 2006.

[19] J. Carvalho. The TileCal/ATLAS calorimeter calibration systems. ATL-TILECAL-PROC-2011-011.

[20] http://root.cern.ch/drupal/

[21] http://www2.pv.infn.it/ gaudio/Monitoring/MuonWeek-200507.pdf

[22] A.Dotti, L.Fiorini. TileCalorimeter DQA Project. ATLAS Note. September 2008

[23] Anderson K et al. 2007 A mobile data acquisition system JINST 2 P07002

[24] Adragna P et al. 2006 GNAM: a low-level monitoring program for the ATLAS experiment IEEE Transaction on Nuclear Science Vol. 53 Num. 3 1317-22

[25] Bosman M et al. 2005 Development and test of the event-filter for the ATLAS experiment 14th IEEE-NPSS RTC 2005

[26] Energy Reconstruction in the Hadronic Tile Calorimeter and Early SUSY Fully Hadronic Searches in ATLAS. Joaquin Poveda Torres - CERN-THESIS-2008-094

[27] ATLAS Muon Trigger Performance in cosmic rays and pp collisions at $\sqrt{s} = 900$ GeV. ATL-ATLAS-CONF-2010-013

[28] ATLAS Collaboration, Muon Spectrometer Technical Design Report, CERN/LHCC/97-022 (1997)

[29] ATLAS Collaboration, Expected performance of the ATLAS experiment : detector, trigger and physics, CERN-OPEN-2008-020 - Geneva : CERN, 2009

[30] A. Ruiz-Martinez et al. Monte Carlo Performance of the TileCal Low p_T Muon Identification Algorithm. ATL-TILECAL-PUB-2008-008

[31] https://twiki.cern.ch/twiki/bin/view/Atlas/TriggerPhysicsMenu.

[32] Studies with Muons in ATLAS: TileCal Level-2 Trigger and MSSM Higgs Discovery Reach. Aranzazu Ruiz Martinez - CERN-Thesis-2009-131

[33] https://twiki.cern.ch/twiki/bin/view/Atlas/MuonSliceDataQualityMonitoring

[34] M. Boonekamp et al., Cosmic Ray, Beam-Halo and Beam-Gas Rate Studies for ATLAS Commissioning, ATLAS Note ATL-GEN-2004-001

[35] The ATLAS luminosity working group, *Improved Luminosity Determination in pp Collisions at $\sqrt{s} = 7$ TeV using the ATLAS detector"*, EPJC 73 (2013) 2518.

[36] P. Nason, *A new method for combining NLO QCD with shower Monte Carlo algorithms*, JHEP 11546 (2004) 040, S. Frixione, P. Nason, and C. Oleari, *Matching NLO QCD computations with Parton Shower simulations: the POWHEG method* , JHEP 11 (2007) 070.
S. Frixione, P. Nason, and G. Ridolfi,*A Positive-Weight Next-to-Leading-Order Monte Carlo for Heavy Flavour Hadroproduction*, JHEP 09 (2007) 126.

[37] P.M. Nadolsky et al., *Implications of CTEQ global analysis for collider observables*, Phys. Rev. D78 (2008) 013004, arXiv:0802.0007 [hep-ph].

[38] M.L. Mangano, M. Moretti, H. Lai, P. Nadolsky, and A.D. Polosa, *ALPGEN,, a generator for hard multiparton processes in hadronic collisions*, JHEP 07 (2003) 001.

[39] S. Frixione and B.R. Webber, *Matching NLO QCD computations and parton shower simulations*, JHEP 06 (2002) 029, S. Frixione, P. Nason and B.R. Webber, *Matching NLO QCD and parton showers in heavy flavour production*, JHEP 08 (2003) 007, S. Frixione, E. Laenen and P. Motylinski, *Single-top production in MC@NLO*, JHEP 03 (2006) 092,

[40] M. Czakon, P. Fiedler and A. Mitov, arXiv:1303.6254v1.

[41] G. Corcella et al., *HERWIG 6.5: an event generator for Hadron Emission Reactions With Interfering Gluons (including supersymmetric processes)*, JHEP 01 (2001) 010, G. Corcella et al., *HERWIG 6.5 release notes*, arXiv:hep-ph/0210213.

[42] The ATLAS collaboration,*Study of hadronic tau identification using W and Z events*, ATL-COM-PHYS-2012-1744, https://cds.cern.ch/record/1496528

[43] J. Butterworth et al., Zeit. fur Phys. C72 (1996) 637.

[44] Davidson et al., arXiv:1002.0543,http://www.ph.unimelb.edu.au/ ndavidson/tauola/doxygen/index.html

[45] https://eeh06.physik.hu-berlin.deatlasaplusplus/htmldoc/ROOTFitFitResult.html

[46] https://twiki.cern.ch/twiki/bin/viewauth/AtlasProtected/TopRootCore

[47] https://twiki.cern.ch/twiki/bin/view/AtlasProtected/TopCommonObjects2011

[48] https://twiki.cern.ch/twiki/AtlasProtected/CpReferences/ Final_2011_data_recommendations

[49] The anti-kt jet clustering algorithm. arxiv.org/pdf/0802.1189.

[50] The ATLAS Collaboration, *Measurement of the b-tag efficiency in a sample of jets containing muons with 5 fb^{-1} of data from ATLAS detector*, ATLAS-CONF-2012-043, https://cdsweb.cern.ch/record/1435197.

[51] The ATLAS collaboration. Commissioning of the ATLAS high-performance b-tagging algorithms in the 7 TeV collision data. ATLAS-CONF-2011-102.

[52] The ATLAS Collaboration, *Performance of the Reconstruction and Identification of Hadronic Tau Decays with the ATLAS Detector*, ATLAS-CONF-2011-152

[53] Using Boosted Decision Trees for Tau Identification in the ATLAS Experiment. J.Godfrey. BSc., University of the Fraser Valley, 2006.

[54] The ATLAS Collaboration, Data-Quality Requirements and Event Cleaning for Jets and Missing Transverse Energy Reconstruction with the ATLAS Detector in Proton-Proton Collisions at a Center-of-Mass Energy of Ãs = 7 TeV, ATLAS-CONF-2010-038.

[55] The ATLAS Collaboration, Luminosity Determination in pp collisions at $\sqrt{s}$ = 7 TeV using the ATLAS detector in 2011, ATLAS-CONF-2011-016 (2011).

[56] https://twiki.cern.ch/twiki/bin/viewauth/Atlas/GoodRunsListsTutorial

[57] https:twiki.cern.chtwikibinviewauthAtlasProtectedTopCommonObjects#Electrons

[58] https://svnweb.cern.ch/trac/atlasusr/browser/evallado/TauD3PDAna_rel17

[59] https:twiki.cern.chtwikibinviewauthAtlasProtectedSMDirectPhoton2011Common

[60] https:twiki.cern.chtwiki/binviewauthAtlasProtectedTopCommonObjects#Jets

[61] Tau identification using multivariate techniques in ATLAS. D C OÕNeil

[62] Measurement of the Mis-identification Probability of τ Leptons from Hadronic Jets and from Electrons. ATLAS-CONF-2011-113

[63] Study of hadronic tau identification using W and Z events. S. Cabrera Urbán, S. Protopopescu, T. Pérez Garcia-Estañ, and E. Valladolid-Gallego. ATL-COM- PHYS-2012-1744.

[64] Measurement of the top quark pair production cross section in proton-proton collisions at center-of-mass energies of 7 TeV in final states with a tau lepton with the ATLAS detector. T. Pérez Garcia-Estañ. Thesis.

[65] http://inspirehep.net/record/1114034

[66] https://twiki.cern.ch/twikiAtlasProtected/TopMC11/MC11_Common_Conventions

[67] https://twiki.cern.ch/twiki/AtlasProtected/Top2011MCCrossSectionReference

[68] Measurement of the top quark pair production cross section with ATLAS in pp collisions at $\sqrt{s} = 7$ TeV using final states with an electron or a muon and a hadronically decaying lepton. ATL-COM-PHYS-2011-1664

[69] Measurement of the top quark pair production cross section in pp collisions at $\sqrt{s} = 7$ TeV in the $\ell+\tau$ channel with ATLAS. S. Cabrera Urbán, S. Protopopescu, T. Pérez Garcia-Estañ, and E. Valladolid-Gallego. ATL-COM-PHYS-2014-005.

[70] M. Cacciari et al., Top-pair production at hadron colliders with next-to-next-to-leading logarithmic soft-gluon resummation, Phys. Lett. B710 (2012) 612-622, arXiv:1111.5869 [hep-ph]

[71] M. Beneke et al., Hadronic top-quark pair production with NNLL threshold resummation , Nucl.Phys. B855 (2012) 695-741],http://arxiv.org/abs/arXiv:1109.1536

[72] P. Bärnreuther et al., Percent Level Precision Physics at the Tevatron: First Genuine NNLO QCD Corrections to $q\bar{q} \to t\bar{t}$, Phys. Rev. Lett. 109 (2012) 132001, arXiv:1204.5201 [hep-ph]

[73] M. Czakon and A. Mitov., NNLO corrections to top-pair production at hadron colliders: the all-fermionic scattering channels, JHEP 1212 (2012) 054, arXiv:1207.0236 [hep-ph]

[74] M. Czakon, A. Mitov., NNLO corrections to top pair production at hadron colliders: the quark-gluon reaction, JHEP 1301 (2013) 080,arXiv:1210.6832 [hep-ph]

[75] M. Czakon, P. Fiedler, A. Mitov., The total top quark pair production cross-section at hadron colliders through $\mathcal{O}(\alpha_S^4)$, Phys. Rev. Lett. 110 (2013) 252004, arXiv:1303.6254 [hep-ph]

[76] M. Czakon and A. Mitov, Top++: a program for the calculation of the top-pair cross-section at hadron colliders, arXiv:1112.5675 [hep-ph]

[77] M. Botje et al. , The PDF4LHC Working Group Interim Recommendations, arXiv:1101.0538 [hep-ph].

[78] A. D. Martin et al., Parton distributions for the LHC, Eur. Phys. J.C63 (2009) 189-285, arXiv: 0901.0002 [hep-ph]

[79] A. D. Martin et al., Uncertainties on $alpha_S$ in global PDF analyses and implications for predicted hadronic cross sections, Eur. Phys. J.C64 (2009) 653-680, arXiv:0905.3531 [hep-ph]

[80] H.-L. Lai et al., New parton distributions for collider physics, Phys. Rev. D82 (2010) 074024, arXiv:1007.2241 [hep-ph]

[81] J. Gao et al., The CT10 NNLO Global Analysis of QCD, arXiv:1302.6246 [hep-ph]

[82] R. D. Ball et al., Parton distributions with LHC data,Nucl. Phys. B867 (2013) 244-289, arXiv:1207.1303 [hep-ph]

[83] P. Nason, A new method for combining NLO QCD with shower Monte Carlo algorithms, JHEP 11 (2007) 070

[84] S. Frixione, P. Nason, and C. Oleari, Matching NLO QCD computations with parton shower simulations: the Powheg method, JHEP 11 (2007) 040

[85] S. Alioli, P. Nason, C.Oleari, and E. Re, A general framework for implementing NLO calculations in shower Monte Carlo programs: the POWHEG BOX, JHEP 06 (2010) 043

[86] B.P. Kersevan and E.Richter-Was, The Monte Carlo event generator AcerMC version 2.0 with interfaces to PYTHIA 6.2 and HERWIG 6.5, arXiv:hep-ph/0405247

[87] ATLAS Collaboration, The ATLAS Simulation Infrastructure, Eur. Phys. J. C70 (2010) 823-874

[88] G. Romeo et al., *Jet Energy Resolution from In-situ techniques with the AT-LAS Detector Using pp Collisions at $\sqrt{s} = 7$ TeV*, ATL-COM-PHYS-2011-240.

[89] J. Pumpli et al. *New generation of parton distributions with uncertainties from global QCD analysis*, JHEP 07 (2002) 012.

[90] A.D.martin, R.g. Roberts and R.S. Thorne,*Parton distributions and the LHC: W and Z production*, Eur. Phys J. C14 (2000) 133

[91] CTEQ collaboration, H. Lai et al.,*Global QCD analysis of parton structures of the nucleon: CTEQ5 parton distributions*, Eur. Phys J. C12 (2000) 375.

[92] The ATLAS Collaboration, *Measruement of the inclusive W+- and Z/γ cross sections in the electron and muon decay channels in pp collisions at $\sqrt{s} = 7$ TeV with the ATLAS detector*, PRD85 (2012) 072004.

[93] M.L. Mangano, M. Moretti, H. Lai, P. Nadolsky, and A.D. Polosa, *ALPGEN,, a generator for hard multiparton processes in hadronic collisions*, JHEP 07 (2003) 001.

[94] S. Frixione and B.R. Webber, *Matching NLO QCD computations and parton shower simulations*, JHEP 06 (2002) 029, S. Frixione, P. Nason and B.R. Webber, *Matching NLO QCD and parton showers in heavy flavour production*, JHEP 08 (2003) 007, S. Frixione, E. Laenen and P. Motylinski, *Single-top production in MC@NLO*, JHEP 03 (2006) 092,

[95] P. Nason, *A new method for combining NLO QCD with shower Monte Carlo algorithms*, JHEP 11546 (2004) 040,

[96] ATLAS Collaboration, *Calibrating the b-tag and Misstag efficiencies of the SV0 b-tagging Algorithm with 3 pb^{-1} of Data with the ATLAS Detector*, ATKAS-CONF-2010-041

[97] https://twiki.cern.ch/twiki/bin/viewauth/AtlasProtected/TopMC11

List of Acronyms

ADCs: Analogic to Digital Converters

ASIC: Application Specific Integrated Circuit

ATLAS: A Toroidal LHC Apparatus

BC: Bunch Crossing

BCID: Bunch Crossing Identification

BDT: Booster Decision Tree

BR: Branching Ratio

BS: Beam Spot

BSM: Beyond the Standard Model

CAF: CERN Analysis Facility

CB: Central Barrel

CERN: Conseil Européen pour la Reserche Nucléaire

CIS: Charge Injection System

Cs: Cesium

CSC: Cathode Strip Chamber

CRC: Cyclic Redundancy Check

CTP: Central Trigger Processor

DAQ: Data AcQuisition

DDM: Distributed Data Management

DQ: Data Quality

DQA: Data Quality Assessment project

DQMF: Data Quality Monitoring Framework

DMU: Data Management Unit

DSP: Digital Signal Processor

DVS: Detector Verification System

EB: Extended Barrel

ECAL: Electromagnetic Calorimeter

EF: Event Filter

EW: ElectroWeak theory

FSR: Final State Radiation

GNAM: Event Analysis Framework Monitoring Tool For ATLAS

GRL: Good Run List

GWS: Glashow-Weinberg-Salam Model

HCAL: Hadronic Calorimeter

HG: High Gain

HLT: High Level Trigger

HV: High Voltage

ID: Inner Detector

IP: Interaction Point

ISR: Initial State Radiation

JES: Jet Energy Scale

JetEff: Jet Reconstruction Efficiency

JetRes: Jet Energy Resolution

JVF: Jet Vertex Fraction

LAr: Liquid Argon Calorimeter

LB: Long Barrel

LCG: LHC Computing Grid

LEIR: Low Energy Ion Ring

LEP: Large Electron Positron collider

LG: Low Gain

LHC: Large Hadron Collider

LHCb: Large Hadron Collider Beauty Experiment

LHCf: Large Hadron Collider forward

LINAC: LINear ACcelerators

LLH: Likelihood

LUTs: Look-Up-Tables

L1: Level-1 trigger

L1A: Level-1 Accept

L1ID: L1 identification

L2: level-2 trigger

MBTS: Minimum Bias Trigger Scintillator

MC: Monte Carlo

MDT: Monitored Drift Tubes

MIP: Minimum Ionizing Particle

MS: Muon Spectrometer

MSSM: Minimal Supersymmetric Standard Model

MuCTPI: Muon to Central Trigger Processor Interface

NLL: Next to Leading Logarithm

NLO: Next to Leading Order

NNLO: Next-to-Next-to-Leading-Order

OMB: Optical Multiplexer Board

OS: Opposite Sign Charge

PDF: Parton Density Function

PMT: PhotoMultiplier

PS: Proton Synchrotron

PSB: Proton Synchrotron Booster

PUs: Processing Units

QCD: Quantum ChromoDynamics Theory

QED: Quantum ElectroDynamics Theory

QF: Quality Factor

RDOs: Raw Data Objects

RMS: Root Mean Square

RNMD: Random

ROBs: Read-Out Buffers

ROD: Read-Out Drivers

RoI: Region of Interest

ROLs: Read-Out Links

RPC: Resistive Plate Chamber

SCT: Silicon Micro-Strip sensors

SF: Scale Factors

SM: Standard Model

SS: Same Sign Charge

SUSY: SUperSYmmetry

SVN: SubVersioN

TBM: Trigger and Busy Module

TiCal: Tile Calorimeter

TileDMU: Tile Data Management Unit

TDR: Technical Design Report

TDAQ: Trigger and Data Acquisition system

TGC: Thin Gap Chamber

TRT: Transition Radiation Tracker

TTC: Trigger and Timing Control

TTCrx: TTC receiver chip

WIS: Web Interfaces for Shifters

WLS: Wave-Length Shifting

Agradecimientos

Lo primero de todo, quiero expresar mi agradecimiento a las personas más importantes para mi, a los que tanto me han ayudando para que yo pudiera terminar esta tesis (o lo que hiciera falta): a mi familia, especialmente mi madre y mi tita Uja, y a mis grandes amigos, los de verdad (ellos saben quiénes son, aunque no pueda nombrarlos a todos).

Muchas gracias a M. Victoria Castillo por ayudarme y estar conmigo hasta poder concluir este trabajo, y al grupo TileCal al completo. Gracias a A. Dotti por enseñarme a utilizar las herramientas que me permitieron poner mi pequeña contribución en ATLAS. Gracias a S. Cabrera por abrir paso para el análisis de física de esta tesis y por las correcciones aportadas, y a S. Protopopescu por tantas aclaraciones y guiarme en varios estudios. Gracias a T.Perez por ser mi 'post-doc' sin serlo aún, así como al IFIC por permitirme trabajar dentro del gran proyecto ATLAS.

Gracias a mis amigos de Valencia por los ratos de café, comidas y cháchara, en especial a Paola y Beth; a mis fantásticos compañeros de despacho Vicky y Sebastian, y a mi maravillosa gente del CERN, los que son hormiguitas y los que no, a los que no olvido a pesar del tiempo y la distancia. Gracias a mis capri, Arancha y Nieves, por estar ahí aunque tantos kilómetros nos separan, y al resto de mi gente de Granada, Carmen, Paloma, Jacqueline, Alexandra, ... y a la casa que me ha acogió entre fotografías, vino, pasteles y teatros (¡viva Granada!).

Por último, quiero terminar dando las gracias a los verdaderos responsables de que esta tesis se haya realizado, aquellos que como mi familia han estado conmigo en todo momento y nunca me han abandonado, empujándome hacia adelánte en los peores momentos y motivándome al máximo en los mejores: el Doctor, E.Torrini, Alicia y Jack. Nunca podría haberlo hecho sin vosotros, sin vuestro apoyo y sin vuestro ánimo continuo. Mil gracias a vosotros por no dejarme sola en esto. Por fin, ha llegado la hora de sacar el buen soufflé.